Experimental Study of Gas Bubble Nuclei and Acoustic Cavitation in Gas-Supersaturated Water

February 2019

Tatsuya Yamashita

論文要旨

超音波洗浄では複数の音響流体現象が生じ，被洗浄物の表面汚れを機械的に除去する．近年の報告によると，音響キャビテーション気泡の運動が促進する洗浄面近傍の局所的な液流動が洗浄に有用であることが指摘されている．ところが，高音圧超音波の照射下の激しい気泡崩壊に伴う衝撃波の放射，ジェット流の水撃および液相の温度上昇による洗浄面の壊食（エロージョン）が技術的課題の一つである．本研究では，高効率かつダメージレスの超音波洗浄技術として，曝気水（ガス過飽和水）を洗浄液とする低音圧超音波の使用を提案する．ガス過飽和水では，低音圧超音波の照射下においても，比較的穏やかな音響キャビテーション気泡の駆動が期待される．

はじめに，マイクロバブル曝気によりガス過飽和水を生成し，水中溶存ガス量を評価した．溶存酸素濃度は商用の溶存酸素計により取得できるが，溶存窒素濃度は同様の計測ができない．そこで，固体壁面で初生したガス気泡の準静的な拡散成長過程を観察し，複数気体種に拡張したEpstein-Plessetモデルによりフィッティング処理することで溶存窒素濃度を推算した．この結果，大気圧下で水中に飽和溶存していた窒素（または酸素）の大部分は酸素マイクロバブル（または窒素マイクロバブル）曝気によりパージ（脱気）される事を確認した．

次に，溶存酸素過飽和度に対するキャビテーション気泡の初生確率の応答特性を評価した．ブラウン運動を計測原理とするナノ径粒子解析により，溶存酸素濃度の変化による粒子数密度の大きな差異は見られず，水中の固体ナノ粒子が計測されている事が示唆された．また，ナノ秒パルスレーザーの照射により局所的に水および固体ナノ粒子を加熱することで，ガス気泡の初生を誘起した．初生した気泡は拡散成長し，観察可能なサイズの気泡による散乱光を撮影した．この結果，溶存酸素濃度の増加に伴い，初生気泡数は非線形に増加し，キャビテーション気泡核数が増大（気泡初生閾値が減少）することを確認した．

最後に，ガス過飽和水を洗浄液とし，低音圧超音波の照射下での音響キャビテーション気泡に関する音響流体現象を評価した．洗浄槽内の高速度観察およびPIV解析により，溶存酸素濃度の増加に伴うキャビテーション気泡発生量の増大および液相流（音響流）・気泡流の促進を確認した．次に，シリカ粒子を塗布したガラス板を被洗浄サンプルとし，粒子除去効率を評価した．洗浄試験では，音響キャビテーション気泡による液流動が洗浄を発現させる一方で，粒子除去効率が最大となる溶存酸素濃度の最適値の存在を確認した．これは超音波振動子から伝ぱする音響エネルギーが気泡群の力学的散逸効果により減衰し，音響キャビテーション気泡の洗浄効果が消失したためである．またアルミ箔のエロージョン痕観察および気泡振動誘起の音響周波数解析では，溶存酸素濃度の増加に伴いエロージョンが低減され，気泡の激しい崩壊が回避された．この結果，最適なガス過飽和度の選択により，低音圧超音波の照射下で洗浄効率を維持しつつ，エロージョンを極力回避できる当洗浄技術の優位性が示唆された．

Abstract

A number of acoustic and fluid-dynamic phenomena appear in ultrasonic cleaning baths and contribute to mechanical removal of contaminant particles at immersed surfaces. Recent studies suggest that the acoustic cavitation bubble enhances localized liquid flow on the targeted surfaces, resulting the effective particles removal in ultrasonic cleaning. However, bubbles under high-intensity ultrasound often accompanies shock emission from violent collapse, water hammer from re-entrant jet collision against solid surfaces, and temperature increase by repeated collapse of many bubbles, giving rise to the critical problem of surface erosion. In this thesis, we aim to develop an erosion-free ultrasonic cleaning with the aid of aerated water (gas-supersaturated water), which allows for driving relatively mild oscillation of acoustic cavitation bubbles even under lower-intensity ultrasound.

First, we generate gas-supersaturated water by aeration with microbubbles and evaluate the amount of dissolved gas. While the concentration of dissolved oxygen (DO) can be detected by a (commercial) DO meter, that of dissolved nitrogen (DN) is unavailable. To detect the DN level, we observe the quasi-static diffusion-driven growth of gas bubbles nucleated at glass surfaces and compare it with the extended multi-species theory of Epstein and Plesset where the DN is treated as a fitting parameter. Comparisons between the experiment and the theory suggest that the saturated DN and DO in the water is effectively purged by the aeration of oxygen and nitrogen microbubbles, respectively.

Second, we relate DO supersaturation to the probability of cavitation bubble nucleation. The concentration of contaminant particles in the water is examined by nanoparticle tracking analysis based on Brownian motion and turns out to be rather insensitive to the DO supersaturation, suggesting the detection of nano-sized solid particles in the water. Nanosecond pulse laser is shot into the water in order to locally heat the water or the nano-sized solid particles, triggering bubble nucleation. Since the nucleated bubbles subsequently grow by mass diffusion, the number of visible-sized bubbles is counted from capturing their scattered light. It is confirmed that the number of the nucleated bubbles nonlinearly increases as the DO supersaturation increases, meaning that the number of stable nuclei that contribute to cavitation inception is augmented under the supersaturation.

Finally, we examine the role of cavitation bubbles from cleaning tests under low-intensity ultrasound in DO supersaturated water. Glass slides spin-coated with silica particles are used to define particle removal efficiency. High-speed camera recordings and Particle Image Velocimetry analysis show that the population of cavitation bubbles increases and bubbly streaming flow is promoted under DO supersaturation. The cleaning is found to be achieved mainly by the action of cavitation bubbles, but there exists optimal gas supersaturation to maximize the cleaning efficiency. Beyond the optimal DO supersaturation, the bubbles' population becomes large enough to mechanically absorb a large part of the ultrasound energy propagating from the transducer, giving rise to damped oscillation of bubbles with less cleaning effects. Furthermore, it follows from the simple erosion tests with aluminum foils that DO supersaturation could play a role in minimizing cavitation erosion, which is supported by the frequency spectrum analysis of the acoustic emissions from the oscillating bubbles. Our finding suggests that low-intensity ultrasound irradi-

ation under the optimal gas supersaturation in cleaning solutions allows for having mild bubble dynamics without violent collapse and thus cleaning surfaces without cavitation erosion.

Acknowledgments

First and foremost, I would like to show my deepest gratitude for my supervisor, Assistant Professor Keita Ando, for his outstanding supervision and unwavering academic supports over seven years. His deep understanding and intuition of the topics of bubble dynamics always pushed us to think critically and creatively with the freedom to pursue a range of different research directions. He has always been my best mentor and invaluable sources of guidance throughout my doctoral study. I am also very grateful for his introduction of outstanding researcher, Dr. Claus-Dieter Ohl, and let me explore several projects under his supervision at Nanyang Technological University in Singapore for nine months. I also would like to deeply appreciate him for his warm welcome to the Cavitation Laboratory. He gave me many hard questions and comments and never let me hide in a corner. Your playful style with exciting new ideas encouraged me to tackle challenging experiments.

This thesis would never have been possible without my collaborating and advisory committee. I am grateful to Professor Shinnosuke Obi and Professor Koji Fukagata for their outstanding insights and many questions at every critical stages of my doctoral study. They gave us many international opportunities and great enthusiasm and passion on science. I would also like to deeply thank Professor Koichi Terasaka for his collaboration on ultrasonic cleaning studies, invaluable supports to our experiment, and useful suggestions. I would like to deeply thank Professor Kenjiro Takemura and Assistant Professor Yuta Kurashina for their collaboration on hydroponics studies. The exciting collaborations opened my eye to the areas of chemical engineering and biology.

I would like to thank all the past and present colleagues in Ando Lab for their helpful advices and greatest friendship. Fumiya Hamaguchi deeply committed to variety of experiments with his insight and passion for research. I was very fortunate to work with Tomoki Kondo, Tatsuya Kobayashi, Masashi Sasaki, Eriko Shirota, Risa Yamauchi, Kentaro Asano, Ikumi Takemura, and Yu Katano, who deeply contributed to studies of diffusion dynamics of bubbles and ultrasonic cleaning. I also thank the colleagues in Terasaka Lab, Takemura Lab, Sugiura Lab, Obi Lab, and Fukagata Lab for their great supports to our experiments. I would like to especially thank Kenichiro Shimizu, Dr. Naohiro Sugita, and Tomoyuki Takano for their experimental supports and helpful feedback.

We also acknowledge support by Mizuho Foundation for the Promotion of Science. This work was supported in part by MEXT Grant-in-Aid for the Program for Leading Graduate Schools and in part by Mentor-Mitakai. I am very grateful for the financial supports for my doctoral study by the program.

Finally, it is beyond words to express my deepest gratitude for my family for everthing they have done for me with love and patience. My parents gave me everything which is really important in my life: a home filled with love and care, and a freedom to make choices. They have alway been my strongest support and I cannot thank you enough.

Contents

List of Figures

List of Tables

Chapter 1

Introduction

1.1 Acoustics and hydrodynamics of ultrasonic cleaning

Ultrasound, above the frequency range of human audibility (>20 kHz), has been implemented in a wide variety of practical applications after the discovery of piezoelectricity of transducer, which can convert mechanical stress with a certain frequency into electrical energy (ultrasound detection) and vice versa (ultrasound generation) [1]. In particular, high-power ultrasound (>1 W/cm^2), with its mechanical and thermal effects, has been of great interest in many applications: manufacture processing [2–5], food processing [6–11], chemical processing [12–16], or medical therapies or diagnostics [17–22]. The ultrasound-based technology is considered to be unique with non-invasive and high-efficient ability of process intensification. While primary effect of the high-power ultrasound is periodic pressure oscillations, secondary effects are generally predominant including physical, chemical and biological effects by acoustic cavitation or absorption of sound waves (acoustic streaming and heating).

A large part of this thesis deals with ultrasonic cleaning [23] (see Fig. 1.1) to gain significant insight into the more efficient cleaning with less material erosion. The definition of cleaning is the removal of foreign contaminants from the surface of a targeted substrate without causing a physical, and chemical change. The contaminants consist of inorganic or organic materials, which are removed, dissolved, or decomposed selectively by physical, chemical, or biological means, depending on each target. The ultrasonic cleaning has emerged as a primary choice and a well-established method when reaching normally

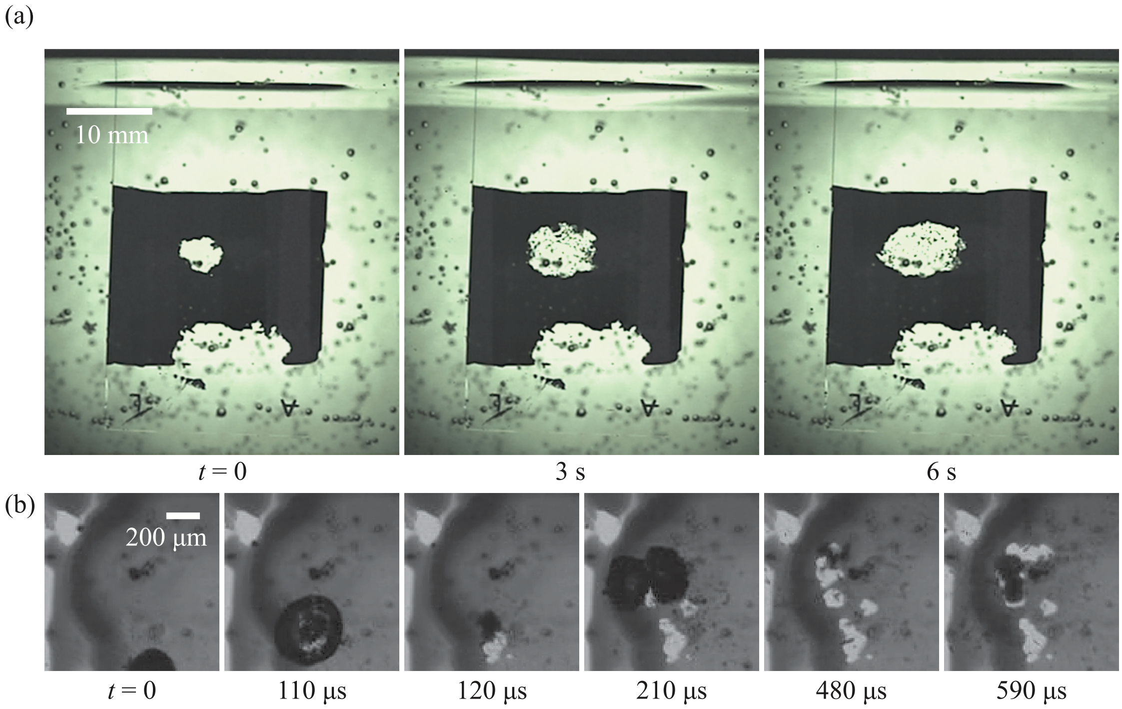

Fig 1.1: Typical images of ultrasonic cleaning of micron/submicron-sized particles attached on glass surfaces immersed in water: (a) Macroscopic observation of ink removal (black area) by cavitation bubbles. (b) Microscopic observation of ink removal (gray area) by a single cavitation bubble.

inaccesible spots with holes or cavities on the targeted surfaces without disassembling them. Such cleaning technology, with its high precision, safety, and consistency, is used in a number of manufacturing processes of products such as semiconductor wafers, optical devices, and precision apparatus [24]. Conventionally, lower frequency (20–100 kHz) is used for degreasing metal objects, while higher frequency (in the range of MHz) is used for removing small particles (of micron/submicron sizes) from delicate surfaces such as semiconductor wafers and liquid crystal displays (i.e., the so-called megasonic cleaning) [25,26]. Ultrasonic cleaning is often combined with toxic chemicals (detergents) in cleaning solutions to enhance its efficiency reducing the adhesive forces between the contaminants and the targeted surfaces [27]; however, physical cleaning that does not rely on any chemicals and has sufficient mechanical forces is favored from an environmental point of view (less toxic chemicals and less rinsing process)[28].

Recent studies on ultrasonic cleaning [29–34] suggest that acoustic cavitation (Fig. 1.2),

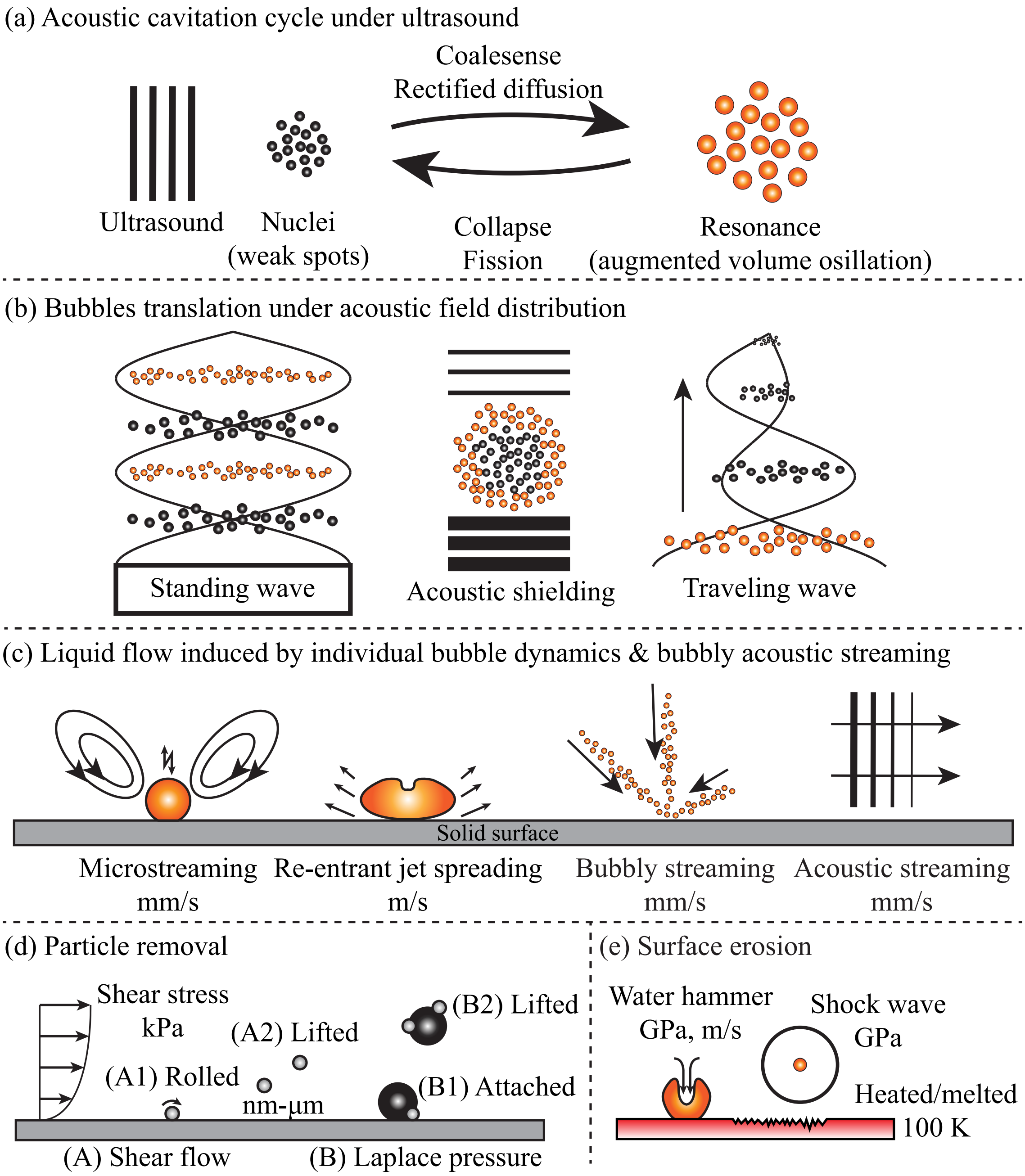

Fig 1.2: Schematic overview of acoustics and hydrodynamics in ultrasonic cleaning: (a) acoustic cavitation cycle under ultrasound with repeated growth and fission, (b) bubbles translation under acoustic field distribution (standing wave/traveling wave), (c) liquid flow induced by individual bubble dynamics and bubbly acoustic streaming, (d) mechanism of particle removal by wall shear stress or Laplace pressure jump, and (e) mechanism of surface erosion by shock emission from violent collapse, water hammer from re-entrant jet collision against solid surfaces, and temperature increase by repeated collapse of many bubbles.

which is nucleated by stretching liquid under the rarefaction phase of ultrasound beyond its tensile strength [35,36], serves as the main cleaning agent. The nucleated bubbles oscillate in volume under ultrasound forcing and then grow due to the net influx of gases dissolved in the liquid by area and shell effects (i.e., the so-called rectified mass diffusion [37–41]). As the bubbles approach the resonant size corresponding to the (forced) ultrasound frequency, the amplitude of their volume oscillation is augmented [42,43]. Bubble collapse under resonance can be violent enough to split single bubbles into smaller fragments; these bubble fragments then oscillate as a cloud [44–49]. Oscillating bubbles can be trapped by the primary Bjerknes force [50] in standing-wave-like acoustic fields that appear in ultrasonic cleaning baths; bubbles smaller and larger than the resonant size are trapped, respectively, at the antinodes and nodes of the pressure field [51,52] (Fig. 1.2(b)). If the bubble population is dense, the nearby bubbles that oscillate in phase are more likely to coalesce by the secondary Bjerknes force [53–56]. Since surface tension becomes less effective after the bubble coalescence, the merged bubbles result in fission more easily [57]. During the repeated coalescence and fission, the oscillating bubbles keep moving between the node and antinode, depending on the ratio of the equilibrium bubble radius to the resonant radius (in the linear scenario), which is believed to sustain the cavitation process [58] (Fig. 1.2(a)).

Another complication, in addition to the dynamics of individual cavitation bubbles, may arise under the existence of densely populated cavitation bubbles in ultrasonic cleaning baths (Fig. 1.2(b)). Since the energy of ultrasound propagating through bubbly liquids is converted into oscillations of the dispersed bubbles, the ultrasound intensity can exhibit a significant reduction in the propagation direction, impairing a standing-wave-like acoustic field in the baths [59–65]. Under the acoustic intensity gradient, bubbles can translate by the acoustic radiation force [66,67], entraining the surrounding liquid [68–76]. Such streaming of bubbly liquids is expected to arise even in the case of low-frequency ultrasound, provided that there appear a sufficiently large number of cavitation bubbles in the baths.

Both individual bubble dynamics and bubbly acoustic streaming are believed to contribute to physical cleaning mechanisms (Fig. 1.2(c)), including wall shear stress that is generated by instantaneous motion of bubbles (such as re-entrant jet spreading over solid surfaces) [77–82] or by time-averaged microstreaming [83–85], and Laplace pressure jump across moving bubble interfaces [86–89]. The previous studies [90–92] suggest that contaminant particles adhering to solid surfaces via the van der Waals force [92] are removed mainly by the rolling mechanism that arises from liquid shear flow (Fig. 1.2(d)). Here, we summarize the cleaning aspects and superiorities of acoustic cavitation bubbles and bubbly acoustic streaming as:

- Instantaneous/time-averaged local flow by the acoustic cavitation dynamics removes the contaminant particles, and continuous bulk flow by bubbly acoustic streaming prevents their reattachment from the surfaces.
- Acoustic cavitation bubble translates by the primary Bjerknes force from acoustic intensity gradient or by the secondary Bjerknes force from the nearby bubbles, enlarging effective cleaning area.
- Acoustic cavitation bubble is attracted to the nearby surfaces by the secondary Bjerknes force (mirror effect) or directly nucleated from the surfaces, enhancing the ability of continuous cleaning.
- Rectified diffusion, coalescence, and fission of bubbles are likely to be repeated, sustaining the process of acoustic cavitation and thus the cleaning over long time periods.

Since acoustic cavitation serves as the main cleaning agent, it is reasonable to refer to the physical characteristics affecting such cavitation dynamics and the resulting efficiency of ultrasonic cleaning [93–101]. Acoustic cavitation is sensitive to a number of external parameters: sonication conditions (intensity [51, 102, 103], frequency [104–112], waveform [113–116], sound direction [117–122], or liquid height [123–125]) and liquid properties (liquid types [126–128], temperature [97, 102, 103, 129], surface tension [130–132], or viscosity [130, 133, 134]). Although such complicated external parameters makes it difficult to predict and control acoustic cavitation in time, space and size, we can organize the cleaning by considering two possible arrangements from engineering viewpoints:

- **Cleaning process window** [135]: Targeted intensity of the cleaning forces by bubble dynamics and bubbly acoustic streaming are carefully chosen by considering the adhesion force of contaminant particles and mechanical strength of targeted surfaces. The characteristics of the cleaning forces (cavitation intensity, bubbles size and population, boundary layer thickness, or frequency) must effectively correspond to those of the cleaning targets.

- **Energy efficiency**: Effective sonication conditions for realizing the targeted cleaning forces are carefully chosen by considering acoustic field distribution. Standing wave effect has preferential sites for the cleaning but less uniformity on the targeted surfaces. Acoustic intensity must exceed the threshold for cavitation nucleation. Void fraction of the nucleated bubbles can enhance the cleaning efficiency and attenuate the acoustic energy (promotion of acoustic streaming and acoustic shielding).

Indeed ultrasound cavitation contributes to the cleaning, but it also has a side effect; bubbles under high-intensity ultrasound often accompanies shock emission from violent collapse, water hammer from re-entrant jet collision against solid surfaces [136, 137], and temperature increase in solid surfaces by repeated collapse of many bubbles [138, 139], giving rise to surface damage [140–147] (Fig. 1.2(d)). To avoid such cavitation erosion, degassed water is conventionally used as cleaning solutions in order to reduce the probability of having cavitation bubble nucleation in the liquid [99, 148–151]. Unfortunately, in this approach, the cleaning efficiency will be reduced in the absence of bubbles as cleaning agents. We can thus say that toward the development of **erosion-free, ultrasonic cavitation cleaning**, there is a need to realize mild bubble oscillation [152, 153].

1.2 Cavitation in gas-supersaturated water

To drive mild cavitation dynamics for erosion-free ultrasonic cleaning, low-intensity ultrasound irradiation is required. Even with low-intensity ultrasound, there are perhaps the following two approaches to effectively trigger bubble nucleation from weak spots

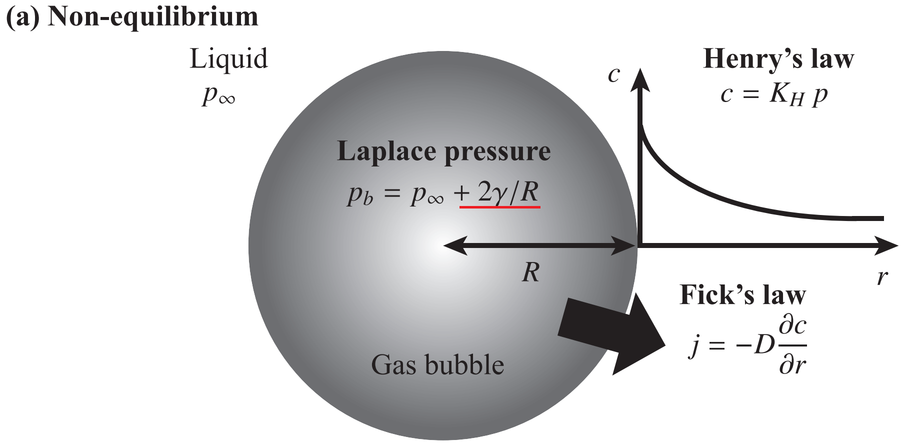

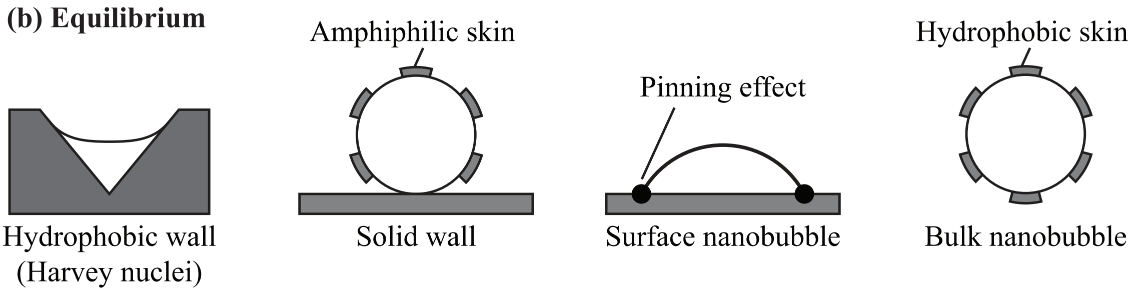

Fig 1.3: (a) Schematic of the diffusion-driven dynamics of gas bubble. Generally, a gas bubble is unstable against dissolution unless the system is in equilibrium. Henry's law states the linear relationship between partial pressure of gas and their solubility. Laplace pressure drives the gas dissolution from the bubble into the liquid. Fick's law states the linear relationship between volume flux of gas and the gradient of gas concentration. (b) Gas bubble can become diffusion-equilibrium by hydrophobic wall [154], amphiphilic skin [155], pinning effect [156], or hydrophobic skin [157].

(heterogeneous nucleation) [158]:

- **Gas bubble nucleation sites** are intentionally provided in cleaning solutions.
- **Dissolved gas supersaturation** is realized in cleaning solutions.

In the former approach, injected bubbles [159–165] or gas pockets at micropits that are etched on solid surfaces [166–169] work as cavitation nuclei and ultrasound-induced dynamics of cavitation bubbles are reported to improve cleaning efficiency. With the latter approach we explore in this paper, a larger number of stabilized gas bubble nuclei are expected to exist in the cleaning solution whose surface tension is lowered under dissolved gas supersaturation [170–172], leading to a reduction in the cavitation inception threshold [173–180].

When we consider the diffusion dynamics, gaseous bubbles are inherently unstable unless the system is out of equilibrium (Figure 1.3(a)). Henry's law states that the amount of dissolved gas in liquids, c, is directly proportional to the partial pressure of gas, p: $c = K_H p$ where K_H is Henry's constant which decreases with temperature. The internal pressure of a spherical gas bubble at the equilibrium state can be described by the Young-Laplace equation, $p_b = p_\infty + 2\gamma/R$, where p_∞ is the ambient pressure of liquid, γ is the surface tension, and R is the bubble radius. For example, a gas bubble of 1 μm in radius has an internal pressure of 2.5 atm. From Henry's law and Young-Laplace equation, surface tension strongly drives the bubble dissolution according to Fick's law (if continuum assumption holds) [181]. By extending the seminal theory of Epstein and Plesset [182], describing the quasi-static dissolution of a gas bubble in infinite volume of liquid, we can calculate the bubble's lifetime [183]. For example, an oxygen bubble of 1 μm in radius should dissolve into oxygen saturated water in 10 ms. Additionally, characteristic time scale of diffusion is much longer than those of cavitation, dissolved gas is typically assumed to play minor influence on inertially controlled process of cavitation inception [184]. However, there are several mechanisms which stabilize bubble nuclei by solid surfaces or by diffusion (Figure 1.3(b)). The hydrophobic crack on a particle or surface can create concave-shaped bubble nuclei with the negative Laplace pressure $p_b = p_\infty - 2\gamma/R$ [175]. Furthermore, gas supersaturation determines the thermodynamic stability of nano-sized gas bubbles [185] combining with effects of amphiphilic skin [155], pinning effect [156], or hydrophobic skin [157]. Hence, a larger number of stabilized gas bubble nuclei are expected to exist in the cleaning solution whose surface tension is regarded to be lowered under dissolved gas supersaturation, leading to a reduction in the cavitation inception threshold.

That is, the use of gas-supersaturated cleaning solutions facilitates nucleating cavitation bubbles even with lower-intensity ultrasound. Moreover, as the dissolved gas concentration increases, the partial pressure of gas (not vapor) inside cavitation bubbles is expected to increase [150, 186, 187]. In this case, the (noncondensable) gas content plays a more important role and its cushion effect can in principle mitigate violent collapse often accompanied by nonlinear bubble oscillations [188–191], thus contributing to erosion-free, ultrasound cavitation cleaning. Since degassed or saturated water is used as cleaning solutions in conventional ultrasonic cleaning [97, 132, 192–195], the case with gas-supersaturated water has not been investigated extensively in previous studies [196–198].

1.3 Thesis objective

The overall objective of this thesis is to experimentally develop an erosion-free ultrasound cleaning technique with the aid of cleaning solutions that are supersaturated with dissolved gases. We investigate the diffusion-driven dynamics under gas supersaturation, and acoustics and fluid dynamics with underwater ultrasound and gas supersaturation. The objective of this thesis are:

1. Generate gas-supersaturated water by aeration with microbubbles and evaluate the amount of dissolved gas.
2. Determine nucleation threshold of gas bubbles in gas-supersaturated water.
3. Examine acoustic and fluid-dynamic events in ultrasonic cleaning with gas-supersaturated water.
4. Examine cleaning efficiency in ultrasonic cleaning with gas-supersaturated water.

1.4 Thesis outline

This thesis presents phenomena of acoustics and fluid-dynamics in gas-supersaturated water, toward the development of ultrasonic cleaning with the aid of the gas-supersaturated water. The influence of the gas-supersaturation on mechanical action by cavitation bubbles is studied. We experimentally explore how the gas-supersaturation essentially influence the bubble dynamics and the resulting ultrasonic cleaning. The thesis is organized in five chapters:

Chapter 1 gave a general literature review on the subject of ultrasonic cleaning with aspects of acoustics and fluid-dynamics, including applicability of gas-supersaturated water for ultrasonic cleaning.

Chapter 2 reports the generation of gas-supersaturated water by microbubble's aeration and evaluation of the amount of dissolved gas.. More specifically, water is aerated with oxygen microbubbles in order to produce DO supersaturated water. We aim to quantitatively evaluate whether nitrogen gas originally dissolved in water under one atmosphere is purged by the aeration with oxygen microbubbles. We observe diffusion-driven growth of gas bubbles nucleated and compare it with the multi-species theory of Epstein and Plesset where the (unknown) DN concentration is treated as a fitting parameter.

Chapter 3 reports the effect of gas-supersaturation on bubbles nucleation. We trigger bubble nucleation by an intense nanosecond laser irradiation in DO-supersaturated water and relate the supersaturation to the probability of having the bubble nucleation. We also discuss the effect on the nucleation of contaminant particles floating in the water whose concentration is measured by nanoparticle tracking analysis.

Chapter 4 reports the role of cavitation bubbles from ultrasonic cleaning tests with varying dissolved gas concentration in water. In our cleaning tests, 28-kHz ultrasound with a fixed power inputted to the ultrasound transducer is used to clean glass substrates at which silica particles of micron/submicron sizes are spin-coated. The acoustic and fluid-dynamic events in our cleaning bath are examined by high-speed camera recordings and Particle Image Velocimetry (PIV) analysis. To examine the cleaning efficiency as a function of DO supersaturation, the particle removal efficiency (PRE) is defined by an optical technique based on light scattering.

Chapter 2

Microbubble's aeration to generate gas-supersaturated water

In this chapter, we apply aeration with oxygen microbubbles to tap water; the intent is to quantitatively evaluate whether nitrogen gas originally dissolved in the water under the atmosphere is purged by the aeration with oxygen microbubbles. Oxygen microbubbles are continuously injected to the circulation system of tap water open to the atmosphere. While the concentration of dissolved oxygen (DO) can be detected by a commercial DO meter, that of dissolved nitrogen (DN) is unavailable. To detect the DN level, we observe the growth of millimeter-sized gas bubbles nucleated at glass surfaces in contact with the aerated water and compare it with the multi-species theory of Epstein and Plesset where the (unknown) DN concentration is treated as a fitting parameter. In the theory, we solve binary diffusion of each gas species (oxygen or nitrogen) in the water independently, under the assumption that the dissolved gases are sufficiently dilute. Comparisons between the experiment and the theory suggest that the DN in the water is effectively purged by the oxygen aeration. The supplemental experiment of aeration with nitrogen microbubbles is also documented to show that the DO can be effectively purged as well.

2.1 Introduction

Aeration is employed to efficiently control the amount of gases dissolved in water with various purposes. To enhance the rate of gas dissolution, we often use bubbling where smaller-sized gas bubbles (with larger Laplace pressure and longer residence time) [199] are favored. There are various techniques to generate micron-sized bubbles (the so-called microbubbles) based on decompression, hydrodynamic cavitation or membrane filteration, for example [200]. Aerated water in which gases dissolve beyond their saturation levels has potential uses for industrial and medical purposes including wastewater treatment [201], ozonation for disinfection [202], hydroponics [203], cultured fishery [204], and a rapid oxygen delivery system in therapeutics [205]. To suppress oxidation in food processing, it is favorable to replace oxygen gas with inert gas such as nitrogen or argon [206,207]. On the contrary, nitrogen gas should be purged to avoid decompression sickness of marine divers [208] or gas-bubble disease in fish [209] as a result of the formation of nitrogen bubbles in blood or tissues. In these applications, it is essential to quantitatively monitor gas dissolution in liquids.

While the concentration of dissolved oxygen (DO) in the aerated water can be detected by a commercial DO meter, there do not exist commercially available sensors to detect that of dissolved nitrogen (DN). To detect the DN level, which is the target of the present study, we observe the growth of millimeter-sized gas bubbles nucleated at glass surfaces in contact with aerated water and compare it with the extended theory of [182] that predicts quasi-static growth or dissolution of a single gas bubble whose translation under buoyancy is ignored. The original theory considers the case of single gas species dissolved in liquids. When it comes to discussing the case of air in water, the binary diffusion rates of dissolved oxygen (DO) and nitrogen (DN) are of the same order so that air is usually treated as single-species molecules [210,211]. For observing quasi-static bubble growth, Enríquez *et al.* [212,213] used water–CO_2 solutions with other gas species (air) expelled in order to ignore any interaction between the different gases. In recent studies [214–218], the classical Epstein–Plesset theory is extended to account for binary diffusions of different gas species dissolved in a liquid for the case of subsaturation or saturation under which bubbles dissolve into the liquid. In these studies, dissolved gas species can be assumed to be dilute enough to ignore their interaction, which allows one to rely on Henry's law that indicates a linear proportionality between dissolved gas concentration and gas partial

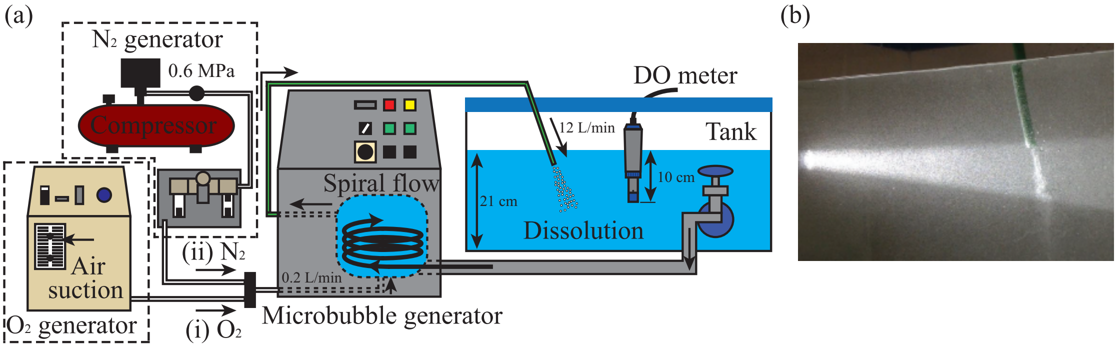

Fig 2.1: (a) A schematic diagram of aerating water by a commercial microbubble generator of spiral flow type. The O_2 generator is replaced with an N_2 generator in supplemental experiments (b) Image of the aeration with oxygen microbubbles produced by the commercial microbubble generator. Oxygen bubbles are ejected from a polyurethane tube whose inner and outer diameter are 7 mm and 9.5 mm, respectively.

pressure at bubble interfaces. As a result, it is possible to solve the diffusion equation for the different gas species independently.

In this study, we aim to quantitatively evaluate whether nitrogen gas originally dissolved in water under one atmosphere is purged by the aeration with oxygen microbubbles. Oxygen microbubbles are continuously injected to the circulation system of tap water open to the atmosphere. The DO concentration is monitored using a DO meter of fluorometric type. To detect the DN level, we observe diffusion-driven growth of a gas bubble nucleated at glass surfaces in contact with the aerated water and compare it with the multi-species theory of Epstein and Plesset that accounts for the binary diffusion of DN in addition to DO [215,218] and treats the (unknown) DN concentration as a fitting parameter. The supplemental experiments of the aeration with nitrogen microbubbles are also documented in the appendices.

2.2 Experimental methods

2.2.1 Aeration and DO measurement

Tap water that is originally saturated with air at room temperature (approximately 19 °C) and ambient pressure (1 atm) is aerated using a commercially available, microbubble generator of spiral flow type (Japan Patent No. 2011-088079), which is depicted in Fig.

2.1(a). This bubble generator creates swirling liquid flow at the volume flow rate of 12 L per minute driven by a centrifugal pump whose rotation core shows a pressure reduction due to centrifugal effects. Pure oxygen gas is sucked into the low-pressure region at the volume flow rate of 0.2 L per minute; the gas phase is split into micron-sized oxygen bubbles due to shearing or compression under pressure recovery [219]. Analyses of bubble images captured by a high-speed camera with a microscope show that the most probable radius of the bubbles is found approximately at 50 μm; see the Appendix A for image processing to determine the bubble size distribution. As seen in Fig. 2.1(b), LED light (SLG-150V, REVOX) is scattered due to a large number of microbubbles that float in the water. Tap water in a 39.6 L acrylic tank open to the atmosphere is circulated by the pump through the bubble generator. Temperature and DO concentration (10 cm from the free interface) are monitored by a DO meter with a fluorometric sensor (SG9, METTLER TOLEDO). Here, we define the (dimensionless) supersaturation of DO according to

$$\zeta_1 = \frac{c_1 - c_{s,1}\,(T)}{c_{s,1}\,(T)}\,, \tag{2.1}$$

where c_1 is the DO concentration detected by the DO meter (in mass per unit volume) and $c_{s,1}$ is the saturated DO concentration at water temperature T. Note that the subscript 1 indicates oxygen while the subscript 2 will be used for nitrogen in the following analysis; the supersaturation of DN, ζ_2, is defined in the same manner. For reference, the saturated concentrations of DO and DN under the atmospheric pressure (0.2 atm oxygen and 0.8 atm nitrogen) are $c_{s,1} = 9.09\ \mathrm{mg\,L^{-1}}$ and $c_{s,2} = 16.4\ \mathrm{mg\,L^{-1}}$, respectively, from Henry's law that suggests a linear proportionality between dissolved gas concentration and gas partial pressure at free surfaces. Since the amount of other dissolved gases such as argon is very small, we account for contributions from oxygen and nitrogen only. During the aeration, a temperature rise due to pumping effects was up to 4 °C. In this study, additional experiments of aeration with nitrogen microbubbles are also conducted by supplying a pure nitrogen gas to the bubble generator.

A maximum (or steady-state) value of DO supersaturation ζ_1 is achieved about 30 minutes after the aeration starts; it records $\max(\zeta_1) = 6.0$ in the experiment. See also Ap-

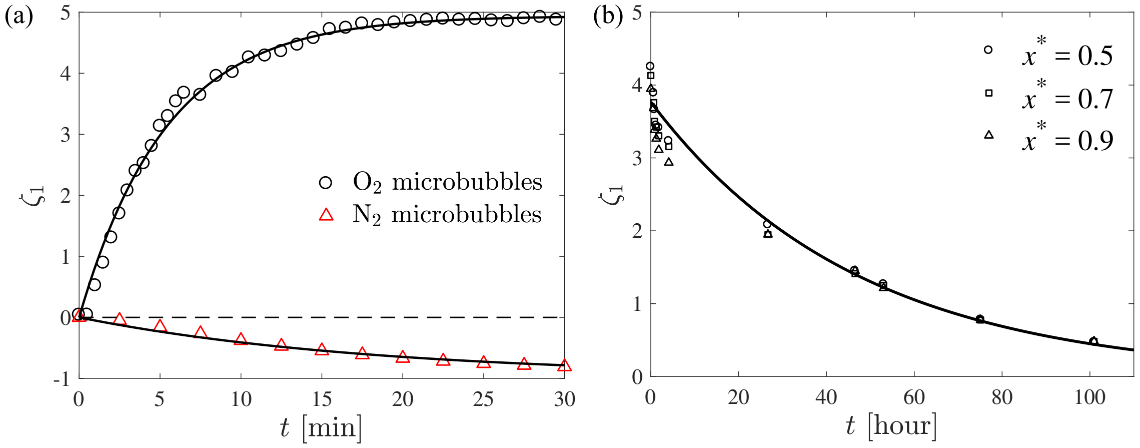

Fig 2.2: (a) Evolution of DO supersaturation ζ_1 during the aeration with O_2 microbubbles and N_2 microbubbles. (b) Degassing rates in the DO supersaturated water at different positions $x^* = x/L$ where x is the spatial coordinate and L is the liquid column height.

pendix B for the effect of bubble size on $\max(\zeta_1)$ as supplemental materials. Fig. 2.2(a) shows the evolution of DO supersaturation ζ_1 during aeration with oxygen microbubbles and nitrogen microbubbles. For the case of oxygen microbubbles, ζ_1 increases to $\max(\zeta_1) = 5.0$. On the contrary, for the case of nitrogen microbubbles, ζ_1 decreases to $\min(\zeta_1) = -0.8$, which means that the DO is effectively purged by the nitrogen aeration. A maximum or minimum value of DO supersaturation is achieved about 30 minutes after the aeration starts for both the cases. After the aeration is finished, large bubbles escape from the tank by buoyancy and the water again looks transparent as usual tap water. For the case of carbonated beverages, gas supersaturation is created by a sudden pressure reduction after pressurized bottles are opened to the atmosphere. Pressure waves accompanied by the bottle opening propagate inside the liquid and are expected to work as a mechanical disturbance to activate nucleation sites at bottle surfaces. Bubbles form from a number of activated nucleation sites, continue to grow under supersaturation, and are eventually detached from bottle surfaces by buoyancy. On the other hand, the water aerated with microbubbles is put under the atmosphere and is not subjected to such pressure transient. Indeed, the bubble formation at the container surface is found to be rather sporadic in comparison to carbonated beverages. This might be attributed to smaller population of activated nucleation sites in the aerated water. The supersaturation in the aerated water

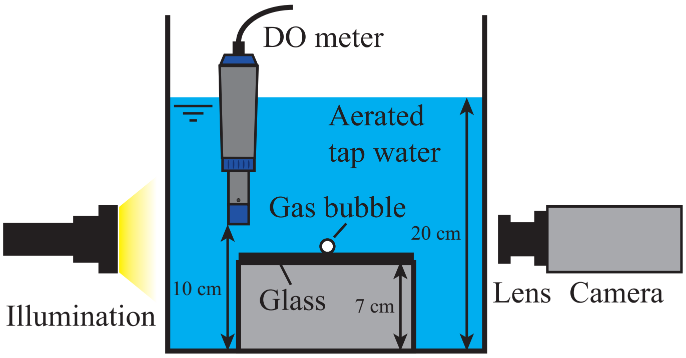

Fig 2.3: A schematic diagram of visualizing the growth of a bubble nucleated at a glass surface in the aerated water.

decays over several days as the DO gradually escapes, with a limited number of nucleation sites, through the free surface. The lower DO supersaturation level is prepared simply by leaving the water open to the atmosphere. Fig. 2.2(b) shows diffusion-driven degassing rates in the DO supersaturated water at different positions. It is noted that, in order to further suppress the probability of having bubble formation at solid boundaries, the aerated water is transferred to a (hydrophilic) glass cylinder whose inner diameter is 85 mm. The height of the water column is set at L =20 cm. The saturation level is lowered due to degassing that is promoted by forced convection in transferring the water to the different container. The DO concentration and temperature in the water are simultaneously measured with the DO meter at 2, 6 and 10 cm below the free surface, which correspond to $x^* = x/L = 0.9, 0.7$, and 0.5, respectively (x is the spatial coordinate). Care is taken to slowly move the DO meter between the different measurement positions, but this will induce some convection in the liquid column. We notice that the spatial and temporal evolution of the concentration field is quite repeatable between the measurements based on different samples of the aerated water. We note that the temperature variation during the measurement period (over days) is up to 2.7°C. Hence, it is more likely that the change in the room temperature can trigger natural convection in the column.

2.2.2 Observation of bubble growth under supersaturation

We observe the growth of a bubble nucleated in the aerated water, which is transferred from the water tank (Fig. 2.1) to a 12.5 L glass container, as illustrated in Fig. 2.3. To heterogeneously trigger bubble nucleation, a microscope glass slide on which a crack of about 100 μm radius is intentionally created by a glass cutter is inserted in the water. Now that the water is supersaturated with DO, a bubble nucleated from the crack is expected to grow as the DO is transferred into the bubble. The bubble growth driven by the mass diffusion is recorded with a video camera (ULTRA Cam, nac) with a microscope (×5.5–6.5, 7.6–9.1 μm per pixel) at 2 frames per minute until it detaches from the surface with buoyancy defeating the capillary force. The time for bubble detachment varies between different observations as will be seen in Fig. 2.7(a) and 2.9(a), for the nucleation site created by a glass cutter is believed to have rough surfaces. Since the inception of bubble nucleation is an instant event, it is an experimental challenge to capture it. We found in the video a nucleated bubble from the crack within a couple of minutes after inserting the glass slide into the water. Practically, we define time $t = 0$ at the initial video frame to capture the nucleated bubble, for the time to find the nucleation was much shorter than the bubble growth phase. The bubble image is extracted by thresholding based on Otsu's method [220].

The observation was performed at four different conditions (i) to (iv) of initial bubble radius R_0 and DO supersaturation ζ_1 (see Table 2.1). We confirmed that the DO reading ζ_1 remained unchanged during the observation of the bubble growth. The observed bubble growth is to be compared with the multi-species Epstein–Plesset calculation where the (unknown) DN supersaturation is treated as a fitting parameter.

2.3 Multi-species theory of Epstein and Plesset

Assuming that bubble growth driven by mass diffusion in a supersaturated solution is gradual enough to ignore advection effects (and that there are no boundaries in the vicinity of bubbles of concern), mass transfer at spherical bubbles can be modeled by the diffusion

Experimental condition	(i)	(ii)	(iii)	(iv)
Initial bubble radius, R_0 [µm]	235	317	379	375
DO supersaturation (measured), ζ_1	6.0	5.4	2.9	1.8
DN supersaturation (fitted), ζ_2	−0.91	−0.9	−0.37	−0.22

Table 2.1: Initial radius of the nucleated bubble (captured in the initial frame), supersaturation from the DO reading, and fitted values of DN supersaturation in experiments (i) to (iv).

equation with spherical symmetry. Epstein and Plesset [182] derived the formula of the quasi-static growth rate of a spherical bubble in infinite liquids for the case of single gas species:

$$R\frac{dR}{dt} = \frac{D}{\rho_G}\frac{\left[c_\infty - c_s\left(1 + \frac{2\gamma}{Rp_\infty}\right)\right]}{\left(1 + \frac{4\gamma}{3Rp_\infty}\right)}\left(1 + \frac{R}{\sqrt{\pi D t}}\right), \tag{2.2}$$

where R is the bubble radius, D is the binary diffusion coefficient, ρ_G is the gas density inside the bubble, γ is the surface tension, p_∞ is the ambient pressure (for this study one atmosphere), and c_∞ and c_s stand, respectively, for the undisturbed concentration away from the bubble and the saturated concentration corresponding to p_∞. Vapor pressure at room temperature is much smaller than gas pressure inside the bubble and its contribution is thus neglected in Eq. (2.2). Our target is the case of supersaturation (i.e., $c_\infty > c_s$) under which bubbles will grow due to gas influx. As the bubble grows, surface tension becomes less influential; this assumption is reasonable, for the bubble size of our concern is on the order of submillimeters to millimeters. Under the approximations, the Epstein–Plesset theory can be extended to include the two components of pseudo-binary gases [215]:

$$\frac{dR}{dt} = \frac{BT}{4\pi R^2 p_\infty}\sum_{i=1}^{2}\frac{dn_i}{dt}, \tag{2.3}$$

where B is the universal gas constant, n_i is the moles of gas species i inside the bubble, and T is the (undisturbed) room temperature. Note that $i = 1$ and 2 stand for oxygen and nitrogen, respectively, which we model as ideal gases; the atmospheric pressure p_∞ consists of $p_{\infty,1} = 0.2$ atm from oxygen gas and $p_{\infty,2} = 0.8$ atm from nitrogen gas. The molar transfer rate for species i is governed by Fick's law together with Henry's law:

$$\frac{dn_i}{dt} = 4\pi R^2 D_i K_{H,i}\left[p_{\infty,i}\left(\zeta_i + 1\right) - p_i\right]\left(\frac{1}{R} + \frac{1}{\sqrt{\pi D_i t}}\right), \tag{2.4}$$

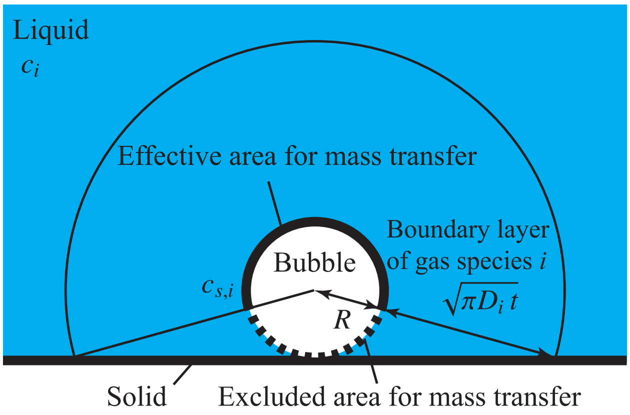

Fig 2.4: Schematic of the geometrical effect of the solid surface on the formation of concentration boundary. The effective area for mass transfer is denoted by the thick solid line, while mass transfer is shielded due to the solid surface (dashed line).

where $K_{H,i}$ is the Henry's constant of species i and $p_i = n_i BT/(4\pi R^3/3)$ is the partial pressure of species i inside the bubble. The right-hand side of Eq. (2.4) divided by $4\pi R^2 D_i$ represents the concentration gradient at the bubble wall $(\partial c_i/\partial r)|_{r=R} = (c_{\infty,i} - c_{s,i})\left(1/R + 1/\sqrt{\pi D_i t}\right)$ [217,221]. The binary diffusion coefficients (in water) and the Henry's constants of species $i = 1$ and 2 are obtained from Wilhelm *et al.* [222] and Sander [223]: $D_1 = 2.4 \times 10^{-9}\,\mathrm{m^2\,s^{-1}}$, $D_2 = 2.0 \times 10^{-9}\,\mathrm{m^2\,s^{-1}}$, $K_{H,1} = 4.0 \times 10^{-4}\,\mathrm{kg\,m^{-3}\,Pa^{-1}}$, and $K_{H,2} = 1.7 \times 10^{-4}\,\mathrm{kg\,m^{-3}\,Pa^{-1}}$.

It is possible to extend the Epstein–Plesset theory to the case of spherical bubbles attached at hydrophilic surfaces with very small contact angles such as glasses. As we will see (in Fig. 2.5), the bubble we obtained keeps fairly spherical during the observation. This situation can be modeled by considering an imaginary bubble (of the identical size) mirrored at the opposite side of the glass surface in order to satisfy no penetration condition across the solid boundary. This means that the bubble growth is hindered by having the imaginary bubble. According to Enríquez *et al.* [213], the effective area ($4\pi R^2 f_{A,i}$) through which mass transfer of species i occurs is estimated by introducing the (dimensionless) correction factor:

$$f_{A,i} = 1 - \frac{1}{2}\frac{\sqrt{\pi D_i t}}{R + \sqrt{\pi D_i t}}. \tag{2.5}$$

The asymptotic limit $f_{A,i} \to 0.5$ means that the concentration boundary layer develops fully and becomes much larger than the bubble, so that the mass transfer rates halve. For

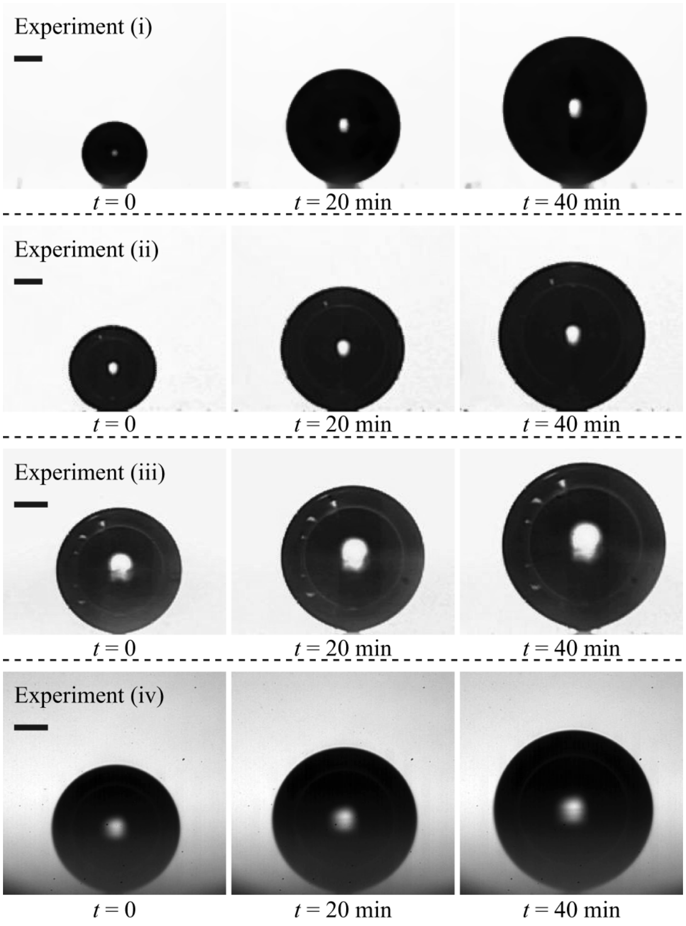

Fig 2.5: A growing bubble attached at the glass surface in experiments from (i) to (iv). The image at $t = 0$ corresponds to the initial video frame to capture the nucleated bubble. Each scale bar shows 200 µm.

comparisons with the experiments, Eq. (2.3) and (2.4) together with correction factor $f_{A,i}$ from Eq. (2.5) are integrated numerically by ordinary differential equation (ODE) solver *ode45* of MATLAB. In these equations, while DO supersaturation ζ_1 is taken from the DO reading in the experiments, DN supersaturation ζ_2 is unknown and thus treated as a fitting parameter.

When it comes to evaluating the concentration boundary layer development, which is represented by $\sqrt{\pi D_i t}$ in Eq. (2.4) and (2.5), the time t needs to be measured from the nucleation of bubbles, rigorously speaking. However, bubble nucleation is an instant event and the nucleation time is thus unavailable from the experiments. In this sense, one can replace t with $(t + t_0)$ in the evaluation where t_0 is a time shift or the time to experimentally find nucleated bubbles after inserting the glass slide into the aerated water. It is important

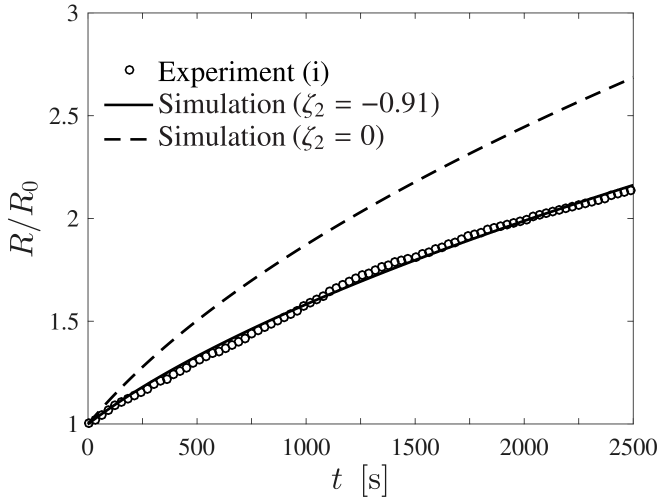

Fig 2.6: Evolution of the growth of the bubble in experiment (i) under the maximum supersaturation of DO at $\zeta_1 = 6.0$. The experiment (i) is compared with the multi-species Epstein–Plesset formula (Section 2.3) with different supersaturation of DN at $\zeta_2 = -0.91$ (fitted) and $\zeta_2 = 0$.

to note that the calculation of DN supersaturation ζ_2 is almost unaffected by the time shift on the order of a couple of minutes in the experiments. This means that the boundary layer development is properly evaluated even with the convenient definition of $t = 0$ from the bubble growth visualization as in Fig. 2.5.

2.4 Results and discussion

2.4.1 Experimental observation

First, we examine the growth of a surface-attached bubble in experiment (i) under the maximum supersaturation of DO at $\zeta_1 = 6.0$ in Fig. 2.5; the measured evolution of the (area-equivalent) bubble radius is plotted with symbols in Fig. 2.6; the bubble radius keeps increasing, while its growth is decelerating, as time progresses. Namely, the radius-time curve does not have any points of inflection.

It is of interest to compare this observation with the the growth of surface-attached bubbles under CO_2 supersaturation. Since CO_2 has much higher solubility than O_2, a difference in the solution density across the concentration boundary layer that forms from nucleated bubbles will come into play during the long observation of the bubble growth.

To be precise, the solution within the boundary layer is CO_2-depleted and its density is thus lower, thereby triggering ascending fluid motion (under buoyancy) around the bubbles. Such natural convection leads to enhancement of the bubble growth rate, for example, in the experiment of Enríquez *et al.* [213] where the gradual growth driven by diffusion is first observed and the accelerated growth is then obtained after the natural convection onset; there exists an inflection point in the radius-time curve in the CO_2-water solution.

Now that the extent of the density difference is much lower in our case of O_2 because of its low solubility, on the contrary, the natural convection on the bubble growth is expected to have a minor impact on the bubble growth. We say, in other words, that the growth is controlled dominantly by diffusion so that the radius-time curve does not show such an inflection point. Indeed, the time for the natural convection onset [224] is estimated at 1200 s to 2900 s for the O_2-water system in experiment (i) to (iv) and is comparable with the observation period, meaning that the natural convection does not alter the early stage of the diffusion-dominant bubble growth.

2.4.2 Comparison to the theory

Now that advection induced by bubble wall velocity $\dot{R} = dR/dt$ is also negligible because of small Peclet number ($\mathrm{Pe} = 2R\dot{R}/D_1 < 0.1$), the Epstein–Plesset calculation is expected to work. In Fig. 2.6, the evolution of the measured bubble growth in experiment (i) is compared with the multi-species Epstein–Plesset theory. In the Epstein–Plesset calculation, there are two unknown parameters:

- the initial mole fraction of oxygen gas inside the bubble, $X_1(0) = n_1(0)/(n_1(0) + n_2(0))$,
- the supersaturation of DN, ζ_2.

Now that the water is supersaturated with DO, it is reasonable to assume that the initial bubble content is mainly oxygen gas; in the calculation, we set $X_1(0) = 1$ as the initial condition. It is instructive to note, however, that the change in $X_1(0)$ is not influential in

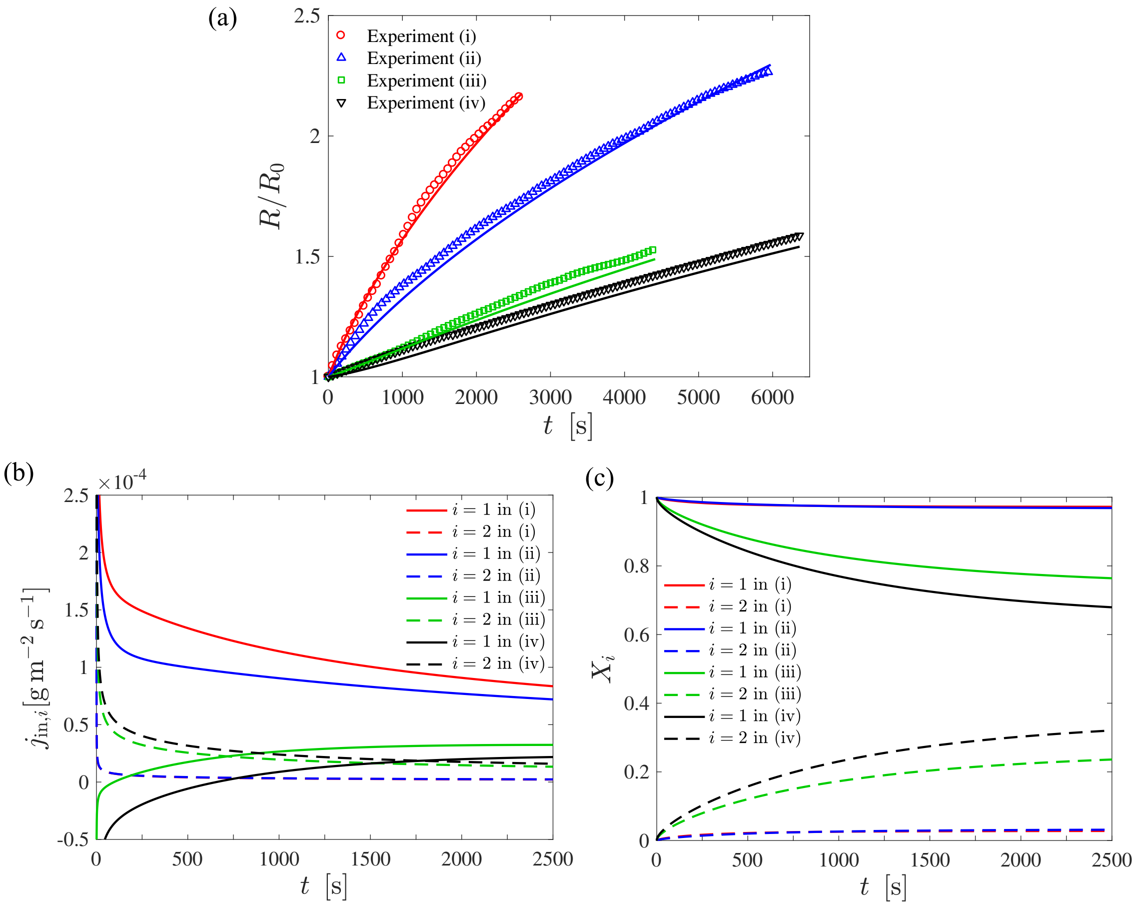

Fig 2.7: (a) Evolution of the growth of the bubble in experiments (i) to (iv). These measurements are compared with the multi-species Epstein–Plesset formula (represented by lines) with the DN concentration fitted (see table 2.1). (b) Simulated evolution of the mass influx of gas species i into the bubble, $j_{\text{in},i}$.(c) Simulated evolution of the mole fraction of gas species i inside the bubble, X_i.

the calculation, meaning that the overall bubble growth is rather insensitive to the initial gas composition of the nucleated bubble.

For the value of DN supersaturation, we consider two scenarios:

- DN is undisturbed by the oxygen aeration and keeps being saturated at 0.8 atm (i.e., $\zeta_2 = 0$) [225, 226],
- DN is purged by the oxygen aeration and thus is lowered (i.e., $\zeta_2 < 0$).

For the latter case, we infer the value of ζ_2 by fitting between the experiment and the theory. It follows from the comparison in Fig. 2.6 that the latter scenario is the case and the fitted DN supersaturation is $\zeta_2 = -0.91$. Note that $\zeta_2 = -1$ means that DN is purged

Experimental condition	(v)	(vi)	(vii)
Initial bubble radius, R_0 [μm]	145	245	214
DO supersaturation (measured), ζ_1	−0.79	−0.7	5.0
DN supersaturation (fitted), ζ_2	2.5	0.86	−0.88

Table 2.2: Initial radius of the nucleated bubble (captured in the initial frame), supersaturation from the DO reading, and fitted values of DN supersaturation in experiments (v) to (vii).

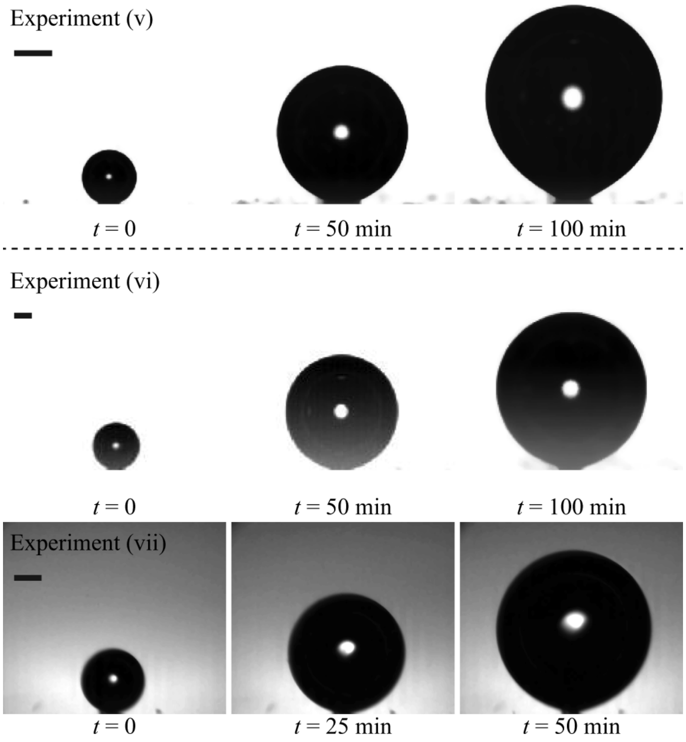

Fig 2.8: A growing bubble attached at the glass surface in experiments (v) to (vii). The image at $t = 0$ corresponds to the initial video frame to capture the nucleated bubble.

perfectly. This suggests that the DN, which is originally saturated under the atmosphere, is effectively purged by the oxygen aeration.

The fitting procedure is applied to the observation up to bubble detachment in experiments (i) to (iv); see Fig. 2.7(a). The fitted values of ζ_2 are documented in Table 2.1. The overall trend in the bubble growth is found to be well fitted by the multi-species theory of Epstein and Plesset. We recorded the bubble growth until the bubble was detached from the glass slide, but did not observe remarkable increases in the growth rate by natural convection as seen in the CO_2-water system of Enríquez *et al.* [213]. It is clear that the bubble growth is suppressed as the DO supersaturation ζ_1 is reduced. More importantly, the DN concentration increases as the DO concentration decreases. Since we obtained the lower DO level by leaving the aerated water open to the atmosphere, the nitrogen gas in the atmosphere again dissolves into the water through its free surface.

We calculate the the influx of gas species i into the bubble, $j_{\mathrm{in},i} = M_i(dn_i/dt)/(4\pi R^2)$ where M_i is the molecular weight of species i, and plot its evolution in Fig. 2.7(b). For experiments (i) and (ii) where the DO supersaturation is relatively high, the oxygen influx is dominating over the nitrogen influx (except in the initial stage at which the growth is sensitive to the initial condition $X_1(0)$); the bubble growth is driven mainly by the transfer of DO into the bubble. When we look at the evolution of mole fraction of gas species i inside the bubble X_i (Fig. 2.7(c)), mole fraction of oxygen X_1 is also dominating over the mole fraction of nitrogen gas X_2. It is interesting to note, on the contrary, that the negative influx (i.e., outflux) of the DO arises when the DO supersaturation is not sufficiently high as in experiments (iii) and (iv); to be specific, the right-hand side of Eq. (2.4) is negative because of $p_i > p_{\infty,i}(\zeta_i + 1)$. As the DN is transferred into the bubble, the mole fraction of oxygen X_1 is reduced so that the influx of the DO is eventually obtained, regardless of the initial condition $X_1(0)$.

2.4.3 Nitrogen aeration to air-saturated water

So far, we have studied the aeration of water with oxygen microbubbles and its role of purging nitrogen gas originally dissolved in the water. We performed another experiment same as in Section 2.2, but aerating with nitrogen microbubbles. As mentioned in Section 2.2.1, after the 30-minutes aeration, the value of ζ_1 decreases to $\min(\zeta_1) = -0.8$ (i.e., DO subsaturation), which means that the DO is effectively purged by the nitrogen aeration. The growth of a surface-attached bubble in the aerated water is then observed (Fig. 2.8); the experimental conditions (v) and (vi) are summarized in Table 2.2.

To detect the supersaturation of DN, we calculate the multi-species Epstein–Plesset equations in Section 2.3 and fit them to the experiments. Since the water is now supersaturated with DN, the bubble just after nucleation is expected to consist mainly of nitrogen gas so that $X_1(0) = 0$; the (unknown) DN supersaturation is treated as a fitting parameter

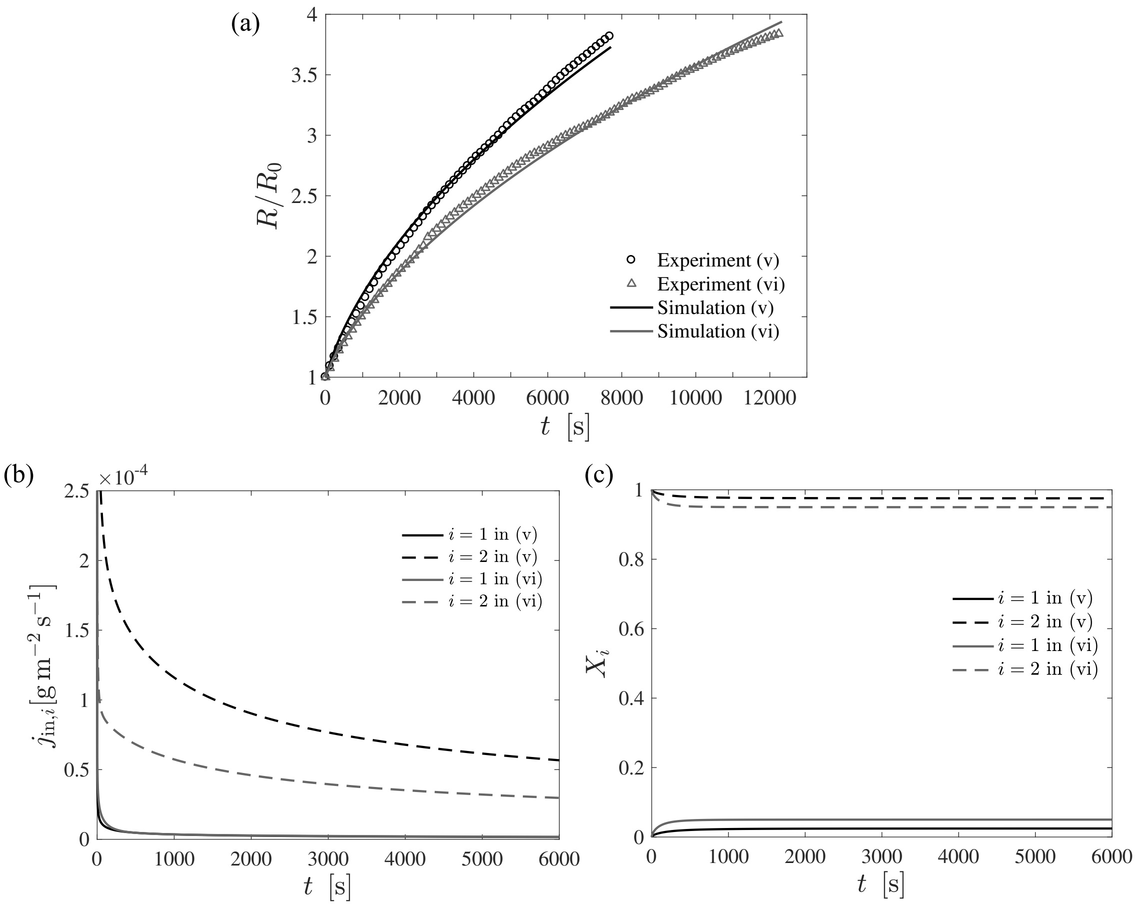

Fig 2.9: (a) Evolution of the growth of the bubble in experiments (v) to (vii). These measurements are compared with the multi-species Epstein–Plesset formula with the DN concentration fitted (see table 2.2). (b) Simulated evolution of the mass influx of gas species i into the bubble, $j_{\text{in},i}$. (c) Simulated evolution of the mole fraction of gas species i inside the bubble, X_i.

as in Section 2.4.

In Fig. 2.9(a), the simulated evolution of the bubble growth is compared with the experiments (v) and (vi). The experiments are found to be well fitted to the calculations, meaning that the bubble growth is caused mainly by diffusive effects. At the minimum DO concentration in experiment (v), we predict the maximum DN supersaturation at $\max(\zeta_2)$ from the fitting. It should be pointed out that the maximum DO supersaturation obtained from the oxygen aeration is 2.4 times higher than the maximum DN supersaturation from the nitrogen aeration; indeed the ratio $(\max(\zeta_1)/\max(\zeta_2) = 2.4)$ agrees with that of the Henry's constants between oxygen and nitrogen ($K_{H,1}/K_{H,2} = 2.4$ at the room temperature). The evolution of mass influx $j_{\text{in},i}$ in experiments (v) and (vi) is also computed in

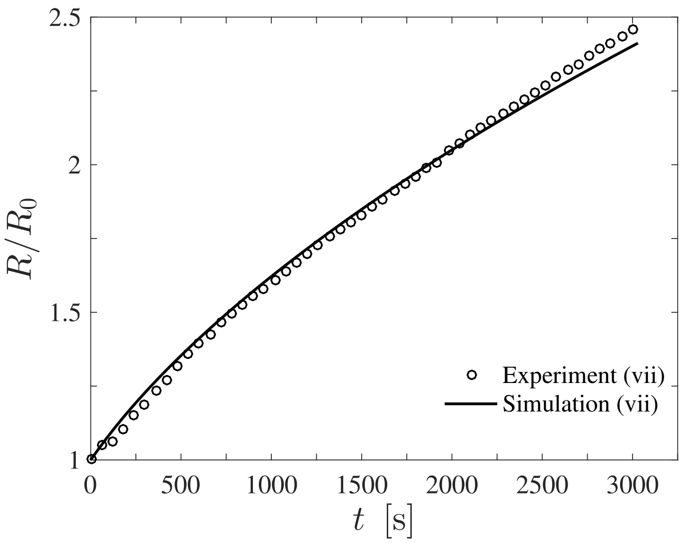

Fig 2.10: As Fig. 2.6, but with the oxygen aeration applied to DN-supersaturated water at $\zeta_2 = 1.3$ (fitted according to Section 2.4.3).

Fig. 2.9(b). We can confirm, in this case, that the bubble growth is driven mainly by the transfer of DN into the bubble, and mole fraction of nitrogen X_2 is also dominating over the mole fraction of oxygen X_1.

2.4.4 Oxygen aeration to DN-supersaturated water

In all the above experiments, the water we used is originally saturated under the atmosphere. To examine the influence of the initial state of dissolved gases on the purging performance, we performed another experiment of applying the oxygen aeration to DN-supersaturated water that is prepared by the nitrogen aeration beforehand. Aeration with nitrogen microbubbles was first applied to (gas-saturated) tap water for 20 minutes, producing DO subsaturation at $\zeta_1 = -0.64$ from the DO reading and DN supersaturation at $\zeta_2 = 1.3$ from the analysis as in Section 2.4.3. Then, the oxygen aeration was applied to the DN supersaturated water for 30 minutes. The bubble growth observation and its fitting to the theory followed in Fig. 2.8 and 2.10, which allowed us to calculate the DN concentration at $\zeta_2 = -0.88$ (see also Table 2.2) in the water after the oxygen aeration; namely, the dissolved nitrogen was purged effectively as well. We can thus say that the purging effect arises from the aeration, regardless of the initial state of dissolved gases in water.

2.5 Conclusions

To study whether nitrogen gas originally dissolved in water can be purged by aeration with oxygen microbubbles, we devised a technique to measure the concentration of DN. Oxygen microbubbles were continuously injected to the circulation system of tap water that was originally saturated with gases at one atmosphere or was first aerated with nitrogen microbubbles. The gradual growth of a surface-attached bubble in the aerated water was visualized and was then compared with the extended Epstein–Plesset theory that accounts for mass diffusions of multiple gas species. In the comparison, the (unknown) DN concentration is treated as a fitting parameter. It follows from the fitting that the DN can be effectively purged by the oxygen aeration, regardless of the initial state of dissolved gases in the water. From the supplemental experiment, such a purging effect was confirmed also in the cases of aeration with nitrogen microbubbles and of oxygen aeration to DN-supersaturated water. We say that these purging effects, which are well known particularly in food industry and fishery, can be evaluated quantitatively by our technique based on the bubble growth observation and its fitting to the extended Epstein–Plesset theory.

Chapter 3

Laser-induced nucleation of bubbles in oxygen-supersaturated water

Cavitation is a ubiquitous phenomenon in hydraulics (e.g., pumps) and underwater acoustics (e.g., ultrasonic cleaning). However, it is an experimental challenge to quantify effects of cavitation on liquid base flow, for the inception (and subsequent) dynamics of cavitation bubbles depend significantly on the (unknown) extent of contamination (such as gas bubble nuclei and solid particles) in liquids. The stability of gas bubble nuclei, which float in a bulk of liquids or are attached to contaminant particles, is determined by the concentration of dissolved gases and surfactants. Here, we select dissolved oxygen (DO) supersaturation in (unfiltered) tap water as a controlling parameter and relate it to the probability of having cavitation bubble nucleation. The DO supersaturation is controlled by oxygen microbubble aeration. The concentration of contaminant particles in the aerated water is examined by nanoparticle tracking analysis based on Brownian motion and turns out to be rather insensitive to the bubble aeration (and the DO supersaturation). Nanosecond pulse laser at 532 nm is shot into the water to trigger gas bubble nucleation; the number of nucleated bubbles of optically visible sizes is counted. It is experimentally confirmed that the number of the nucleated bubbles increases as the DO supersaturation increases, meaning that the number of stable nuclei that contribute to cavitation inception is augmented under the supersaturation.

3.1 Introduction

Cavitation occurs widely in applications of hydraulics and underwater acoustics. Ultrasonic cleaning is one of the remarkable application of acoustic cavitation, which leads to cleaning forces such as shear stress, acoustic streaming, re-entrant liquid jetting, and shock wave emission due to violent collapse and water hammer from the liquid jet collision [24]. Such high local pressures induced by cavitation is also responsible for the occurrence of mechanical erosion on the surfaces of the cleaning materials [141,227]. One of the critical parameters affecting cavitation is the amount of dissolved gas as it affects threshold for cavitation inception, composition of nucleated bubbles, and their subsequent growth rate [187] Our experiments (see Chapter 4) employ DO supersaturated water with fine-tuning its supersaturation toward realization of erosion-free ultrasonic cleaning. The key idea is that (gaseous) cavitation is triggered easily even with low-intensity sonication in the water, allowing us to buffer violent bubble collapse. Although particle removal efficiency is confirmed to be increased as the DO supersaturation is increased, there is no clear insight into the effect of the supersaturation on the cavitation inception dynamics.

It is a tremendous challenge to quantify the effects of cavitation, for the inception dynamics of cavitation bubbles (in very fast and small scale) depend significantly on the extent of contamination (such as gas bubble nuclei and solid particles) in liquids [35]. The thermodynamic stability of gas bubble nuclei, which float in a bulk of liquids or are attached to contaminant particles, is in principle determined by the concentration of dissolved gases and surfactants.

In the present study, we trigger bubble nucleation by an intense nanosecond laser irradiation in DO-supersaturated water and relate the supersaturation to the probability of having the bubble nucleation. The DO supersaturation is controlled by oxygen microbubble aeration. We also discuss the effect on the nucleation of contaminant particles floating in the water whose concentration is measured by nanoparticle tracking analysis.

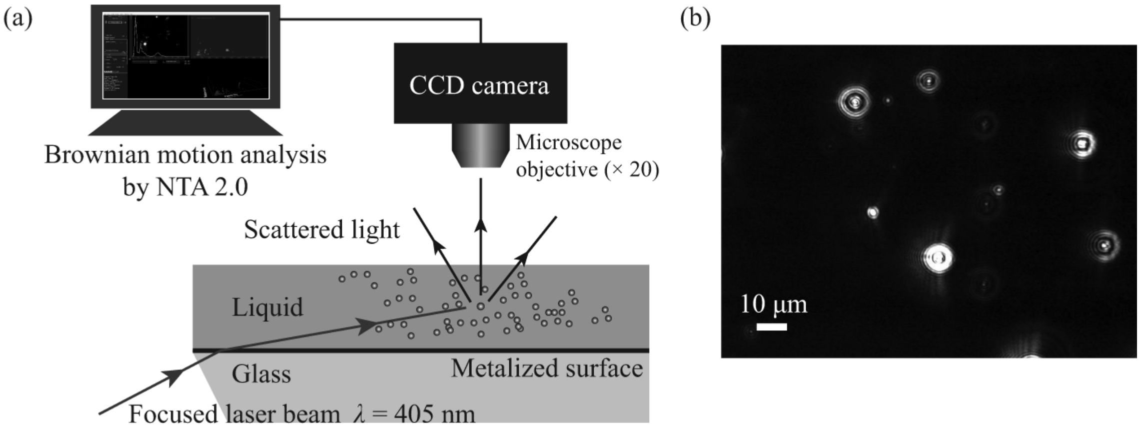

Fig 3.1: (a) Schematic of the NTA. A focused laser is passed through the liquid sample. The scattered lights from the particles in liquid are detected by a CCD camera. The NTA 2.0 identifies the Brownian motion of each particle to obtain its radius by Stokes-Einstein equation. (b) Typical photograph of the captured scattered light from the particles moving under Brownian motion (random walk).

3.2 Experimental methods

According to Chapter 2, DO supersaturation in tap water is produced by aeration with a microbubble generator of spiral flow type (Japan Patent No. 2011-088079). We select oxygen for the aeration since DO can easily be monitored by a fluorometric sensor (SG9, Mettler Toledo). According to Eq. (2.1), we define DO supersaturation ζ in the aerated water. Because of the purging effect of aeration with single gas species, the other dissolved gases such as nitrogen are effectively removed and DO is thus dominant. The DO supersaturation is controlled simply by leaving the aerated water under the atmosphere. The DO supersaturation in the range of $0 \leq \zeta \leq 4.7$ is studied. Surface tension in the water is measured by Wilhelmy method (DY-300, Kyowa Interface Science Co.) and turns out to be close to the value of pure water at 72 mN/m under the range of ζ.

Particle size distribution and concentration in the DO supersaturated water are measured by NANOSIGHT (LM10, NanoSight Ltd., Salisbury, UK) which uses particle tracking analysis [228]. The technique shown in Figure 3.1 is based on the simultaneous tracking and analysis of the trajectories of individual particles moving under Brownian motion with a random walk. As shown in Figure 3.1(a), NANOSIGHT irradiates a CW laser at the wave length of 405 nm and energy of 75 mW on nano-sized particles in liquid, captures

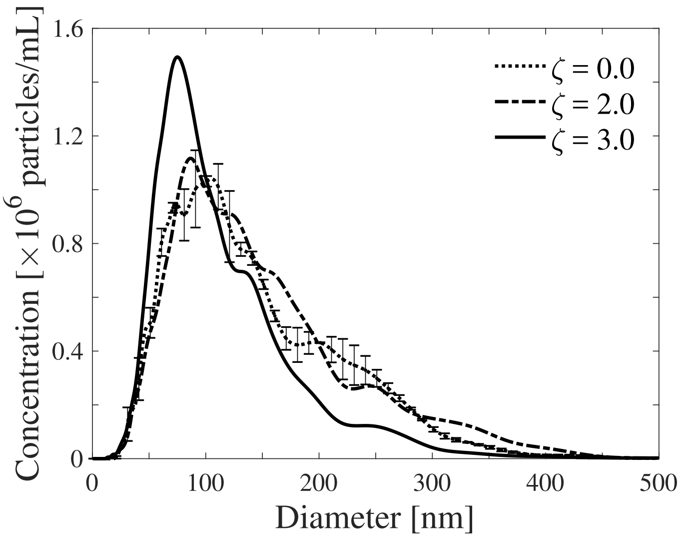

Fig 3.2: Concentration of particles (contaminant solid particles and possibly bubbles) as a function of their radius in the water at two different DO supersaturation. The total particle concentration (the number of particles per cm^3) at $\zeta = 0.0$, 2.0, and 3.0 is 1.51×10^8, 1.57×10^8, and 1.73×10^8, respectively.

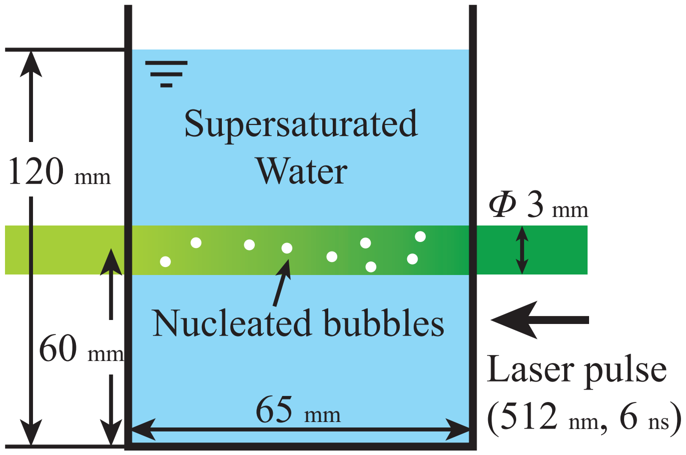

Fig 3.3: Schematic of laser-induced nucleation of gas bubbles by the pulse laser irradiation to the DO-supersaturated water.

the scattered light by a CCD camera at 30 frames per second with a microscope objective lens (×20). With an analytical software, nano-particle tracking analysis (NTA 2.0), we automatically obtains the particle size by analyzing the Brownian motion of the particles within its field of view (80 µm × 100 µm). The relationship between Brownian motion and the particle size is derived from Einstein-Stokes equation [228] $\overline{d}^2 = k_B T t_s / 6\pi R\mu$ where d is the displacement of a particle in two-dimensions, T is liquid temperature, t_s is the sampling time, and μ is liquid viscosity. The broad range of measurable size and concentration

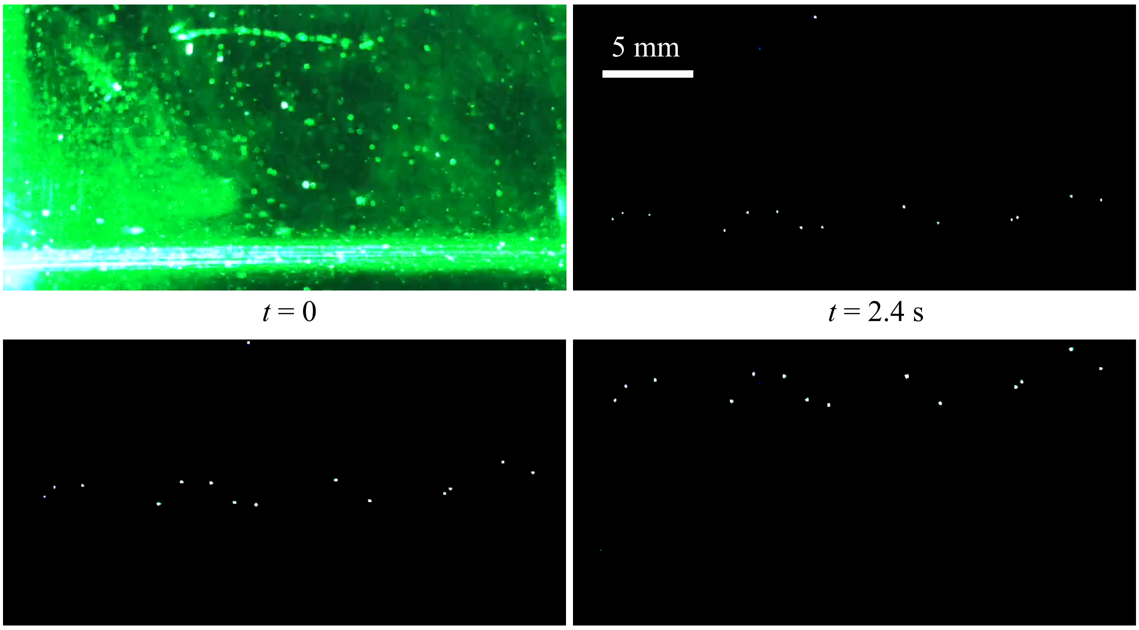

$t = 0$ $t = 2.4$ s $t = 3.6$ s $t = 4.8$ s

Fig 3.4: Typical images of nucleated gas bubbles by the pulse laser irradiation to DO-supersaturated water (ζ = 4.5).

of particles are from 10 – 1000 nm and 1×10^9 particles/mL, respectively. Samples of the aerated water with oxygen is examined with different ζ. Nano-sized particle tracking analysis shows that the size distribution and total number of contaminant particles in the water remain similar before and after the aeration (Fig. 3.2). This implies that the possibility of having nanometer-sized bubbles (the so-called bulk nanobubbles [185]) under the DO supersaturation may be excluded. But the total particle concentration increases with ζ, suggesting the possibility that larger number of stabilized gas bubble nuclei are expected to exist in the aerated water.

As shown in Fig. 3.3, the water in a glass container is exposed to a laser beam of 3 mm in diameter from a Q-switched Nd:YAG laser (ULTRA 50 GRM, Quantel), which produces a 6 ns pulse duration of the second harmonic light (532 nm). The average laser intensity is measured by a power meter (PE50BF-C, Ophir). We confirm that the absorption of laser energy is independent of DO supersaturation. At each laser energy, the laser is shot into the water once per every 30 seconds to trigger bubble nucleation. Nucleated gas bubbles of optically visible sizes are captured by a digital camera (EX-

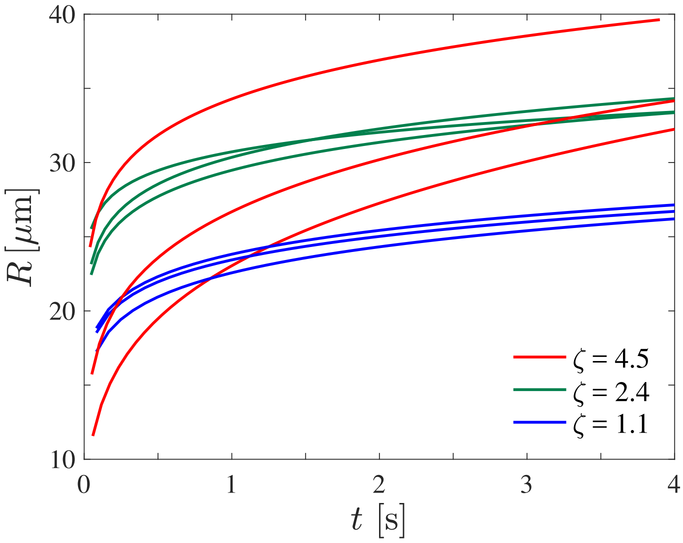

Fig 3.5: Diffusion-driven evolution of bubbles radii nucleated in the water under different DO supersaturation ζ.

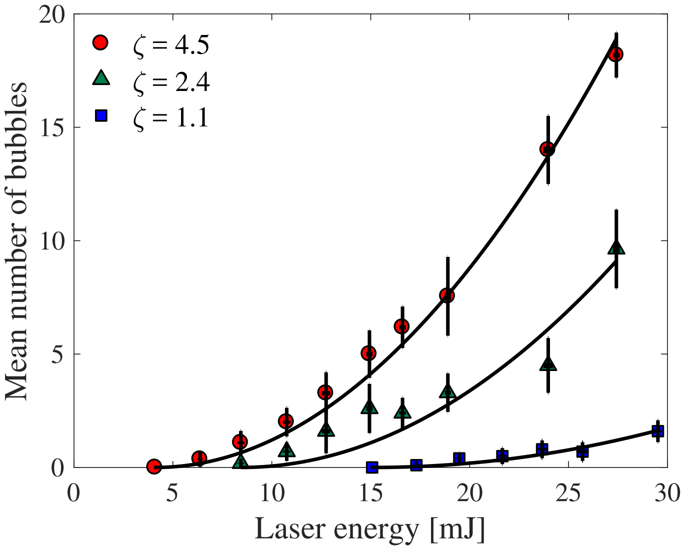

Fig 3.6: The number of nucleated bubbles (captured in the camera image) as a function of the laser energy with different DO supersaturation, ζ = 1.1, 2.4, and 4.5.

100PRO, Casio) at 30 frames per second. A LED light (SLG-150V, Revox) is illuminated at 90 degree from the camera axis to capture the scattered light from the bubbles. Note that plasma-induced vaporous bubbles are not observed in this experiment, which are often obtained by pulse laser focusing [35,229]. Filtered water by 0.2 μm membrane filters (Nalgene Rapid-Flow, Thermo Fisher Scientific) is also used for comparative purposes.

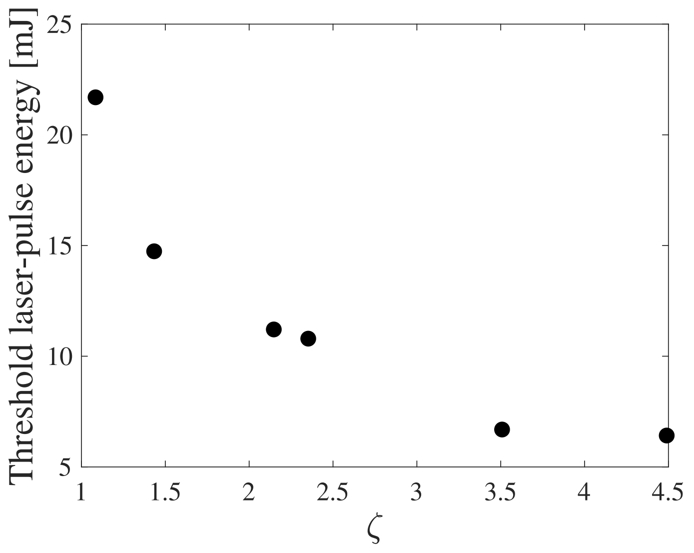

Fig 3.7: Threshold laser energy for nucleation of a gas bubble as a function of DO supersaturation ζ.

3.3 Results and discussion

A typical image of gas bubbles nucleated by the green laser pulse irradiation to the DO-supersaturated water ($\zeta = 4.5$) is presented in Fig. 3.4. As seen in Fig. 3.4, the laser light is scattered due to contaminant particles and nucleated bubbles in the water. The nucleated bubbles start to move upward by buoyancy. We observed that the bubble motion gets faster as the bubble grows due to the incoming transfer of DO under the supersaturation (Fig. 3.5). This trend becomes clearer as the DO supersaturation increases due to the larger gradient of DO concentration around the bubble. From the upward motion of bubbles, we roughly estimate the bubble size under different supersaturation. We confirm that each pulse produced a range of bubble sizes, suggesting bubbles nucleate and grow under slightly different conditions. We note that bubble nucleation does not occur in the saturated tap water with no aeration ($\zeta = 0$) and in the filtered water under the supersaturation even with the maximum laser energy approximately at 30 mJ, implying that bubbles are nucleated selectively from gas bubble nuclei trapped at the surface of contaminant particles [230] that are stabilized under DO supersaturation (see Fig. 1.3(b)).

In Fig. 3.6, we summarize the results from the parameter studies where the laser energy and the DO supersaturation are varied. Here, we plot the mean number of nucleated gas bubbles (captured in the camera image) as a function of the laser energy with varying DO supersaturation at ζ = 1.1, 2.4, and 4.5. The number of nucleated bubbles is found to increase non-linearly as the laser energy increases, as observed in the previous study using CO_2-supersaturated water [178,179]. These show that the nucleation event becomes more probable as the DO supersaturation increases, suggesting that a larger number of gas bubbles attaching at contaminant particles are stabilized under higher DO supersaturation and thus activated as cavitation nuclei by the laser irradiation. Finally, the threshold laser energy of the bubble nucleation is summarized in Fig. 3.7. The nucleation threshold decreases as the DO supersaturation increases.

3.4 Conclusion

We produced DO-supersaturated tap water (in which other dissolved gas species are effectively purged and the extent of contaminant particles remains similar) and irradiated green pulse laser to the water in order to trigger gas bubble nucleation. It follows from a series of the experiments with varying the DO supersaturation (and the laser energy) that the number of nucleated gas bubbles increases as the DO supersaturation increases, implying that the number of stable gas bubble nuclei attaching at contaminant particles is augmented under the supersaturation. As expected, the nucleation threshold is reduced by increasing the DO supersaturation.

Chapter 4

Low-intensity ultrasonic cleaning in oxygen-supersaturated water

A number of acoustic and fluid-dynamic phenomena appear in ultrasonic cleaning baths and contribute to physical cleaning of immersed surfaces. Propagation and repeated reflection of ultrasound within cleaning baths build standing-wave-like acoustic fields; when an ultrasound intensity gradient appears in the acoustic fields, it can in principle induce steady streaming flow. When the ultrasound intensity is sufficiently large, cavitation occurs and oscillating cavitation bubbles are either trapped in the acoustic fields or advected in the flow. These phenomena are believed to produce mechanical action to remove contaminant particles attached at material surfaces. Recent studies suggest that the mechanical action of cavitation bubbles is the dominant factor of particle removal in ultrasonic cleaning, but the bubble collapse resulting from high-intensity ultrasound may be violent enough to give rise to surface erosion. In this paper, we aim to carefully examine the role of cavitation bubbles from ultrasonic cleaning tests with varying dissolved gas concentration in water. In our cleaning tests using 28-kHz ultrasound, oxygen-supersaturated water is produced by oxygen-microbubble aeration and used as a cleaning solution, and glass slides spin-coated with silica particles of micron/submicron sizes are used to define cleaning efficiency. High-speed camera recordings and Particle Image Velocimetry analysis with a pressure oscillation amplitude of 1.4 atm at the pressure antinode show that the population of cavitation bubbles increases and streaming flow inside the bath is promoted, as the dissolved oxygen supersaturation increases. The particle removal is found to be achieved mainly by the action of cavitation bubbles, but there exists optimal gas supersaturation to maximize the removal efficiency. Our finding suggests that low-intensity ultrasound irradiation under the optimal gas supersaturation in cleaning solutions allows for having mild bubble dynamics without violent collapse and thus cleaning surfaces without cavitation erosion. Finally, observations of individual bubble dynamics and the resulting particle removal are reported to further support the role of cavitation bubbles as cleaning agents.

4.1 Introduction

The main objective of the present study is to develop an erosion-free ultrasound cleaning technique with the aid of cleaning solutions that are supersaturated with dissolved gases. Here, we produce dissolved oxygen (DO) supersaturation by applying oxygen-microbubble aeration to tap water and use the DO-supersaturated water as cleaning solutions. In our cleaning tests, 28-kHz ultrasound with a fixed power inputted to the ultrasound transducer is used to clean glass substrates at which silica particles of micron/submicron sizes are spin-coated. The acoustic and fluid-dynamic events in our cleaning bath are examined by high-speed camera recordings and Particle Image Velocimetry (PIV) analysis. To examine the cleaning efficiency as a function of DO supersaturation, the particle removal efficiency (PRE) is defined by an optical technique based on light scattering. In what follows, we first introduce the details of the experimental methods and then discuss the role of cavitation bubbles as cleaning agents from the visualization and the PRE tests with varying the DO supersaturation.

4.2 Experimental methods

4.2.1 Production of DO-supersaturated water

According to Chapter 2, DO-supersaturated water is produced by aerating tap water with a microbubble generator of spiral flow type [201] (Japan Patent No. 2011-088079). We employ pure oxygen gas for the aeration since DO can easily be monitored by a fluorometric

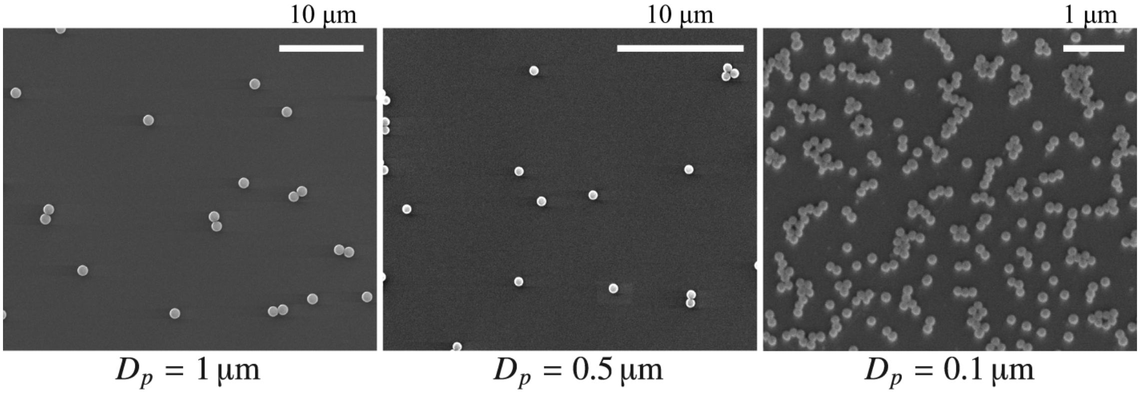

Fig 4.1: SEM images of the silica particles attached at the glass substrate of diameter D_p.

sensor (SG9, Mettler Toledo). According to Eq. (2.1), we define DO supersaturation ζ in the aerated water. Note that $\zeta = 0$ means the DO saturation level at the atmosphere that consists of 0.2 atm oxygen and 0.8 atm nitrogen. Because of the purging effect of oxygen aeration, the other dissolved gases such as nitrogen are effectively removed so that DO is dominant in the aerated water. The DO supersaturation of the water used as the cleaning solution is in the range of $0 < \zeta < 4.2$, which is obtained by leaving the aerated water (with the maximum DO supersaturation at $\zeta \approx 6.0$) in a container open to the atmosphere.

4.2.2 Preparation of cleaning samples

Silica particles whose size is fairly monodisperse ($D_p = 1.0\,\mu\text{m} \pm 0.2\,\mu\text{m}$, $0.5\,\mu\text{m} \pm 0.2\,\mu\text{m}$, or $0.10\,\mu\text{m} \pm 0.04\,\mu\text{m}$ in diameter) are used as contamination. For the particle sizes of our target, van der Waals force is the dominant adhesive force that is linearly proportional to the particle size [231]. The particles are suspended in isopropyl alcohol (IPA) and deposited by a spin drying method at 4,000 rpm for 30 s (1H-D7, Mikasa), on an optically polished, glass disk (30 mm in diameter and 1 mm in thickness) whose surface roughness is below 10 nm. Scanning Electron Microscope (SEM; FEI Inspect S50 or Hitachi S-4700) images of the particles are presented in Fig. 4.1. As will be explained in Section 4.2.4, the concentration of the particles attached at the glass substrate is quantified by an optical technique based on light scattering.

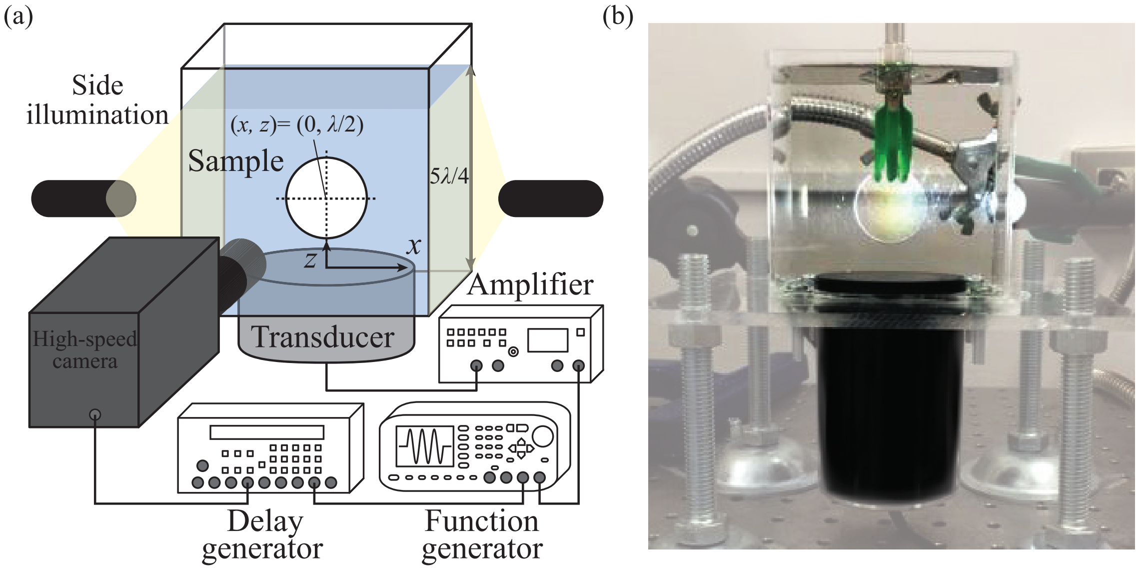

Fig 4.2: (a) Schematic of the ultrasonic cleaning test. Bubbly cavitation structure is captured by the high-speed camera with side illuminations. Individual bubble dynamics are captured with back illumination (not depicted) and a magnification lens. (b) Photograph of the ultrasonic cleaning bath. The diameter of the glass sample is 30 mm.

4.2.3 Ultrasonic cleaning system and acoustic pressure measurement

Figure 4.2 illustrates our ultrasonic cleaning tests. For visualization of acoustic and fluid-dynamic phenomena, we created an ultrasonic cleaning bath with transparent, acrylic plates. A cylindrical-shaped transducer with the resonant frequency at 28 kHz (0.028Z45I, Japan Probe) we used is a hermetically sealed structure in which a cylindrical piezoelectric ceramic of 45 mm in diameter is embedded in a cylindrical ABS container of 65 mm in diameter. The transducer is mounted on the bottom of a rectangular-shaped bath whose lateral dimensions are 90 mm × 90 mm. We measure the horizontal (x) and vertical (z) distances from the center of the transducer's surface. For the cleaning, 28-kHz sinusoidal wave in the bath is generated continuously for 30 s by a multi-function generator (WF1973, NF Co.), magnified by a power amplifier (HSA4014, NF Co.), and fed to the transducer.

The aerated water (with different DO supersaturation ζ) as the cleaning solution is poured into the cleaning bath. The water temperature is at the room temperature (approximately 20 °C), so that the corresponding wavelength of the ultrasound ($f = 28$ kHz) in

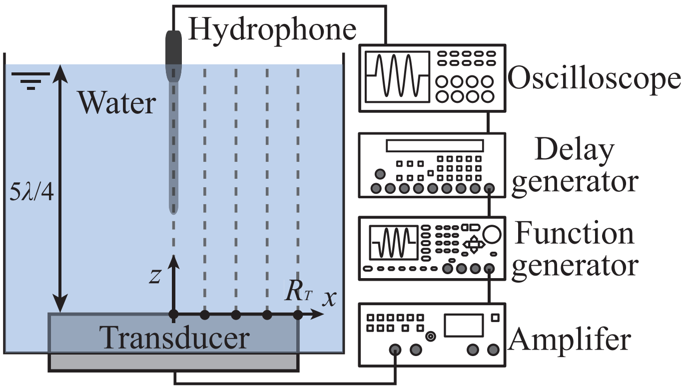

Fig 4.3: Schematic of pressure distributions measurement along the z direction at different horizontal positions $x = 0, R_T/4, R_T/2, 3R_T/4$, and R_T where R_T denotes the radius of the cylindrical transducer. Acoustic emission from the cavitation bubbles is also measured at $(x, z) = (0, \lambda/2)$ in the water with different DO supersaturation ζ.

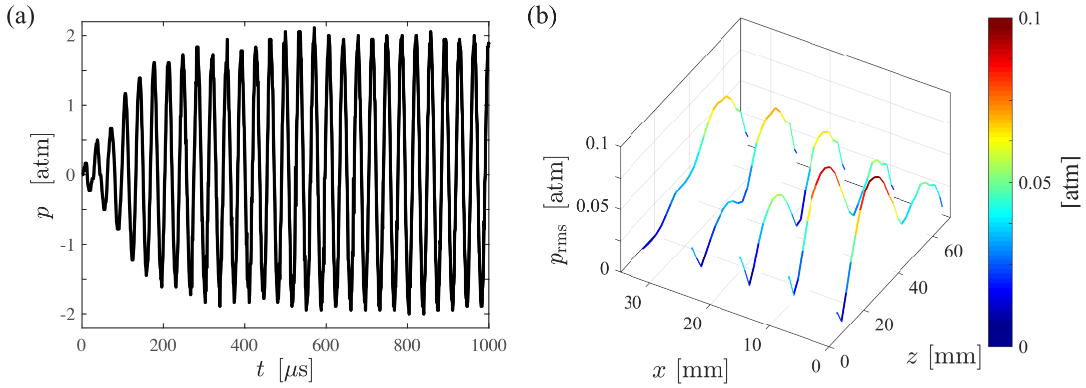

Fig 4.4: (a) The pressure waveform at the pressure antinode $(x, z) = (0, \lambda/2)$. (b) Effective pressure intensity distributions in the bath (without cavitation bubbles and the glass sample) along the z direction at five different horizontal positions x.

water of sonic speed $c_l = 1483$ m/s is computed as $\lambda = c_l/f = 53$ mm. The water surface is set at five quarters of the wavelength, $z = 5\lambda/4 = 66$ mm (see Fig. 4.2).

Pressure distributions (without inserting the glass sample) along the z direction at different horizontal positions at $x = 0, R_T/4, R_T/2, 3R_T/4$, and R_T (where $R_T = 32.5$ mm denotes the radius of the cylindrical transducer) are measured using a needle hydrophone of 3 mm in diameter (HCT0310, Onda Co.) and recorded with an oscilloscope (TDS2024C, Tektronix) at a sampling frequency of 1 MHz. In these pressure measurements, low-intensity ultrasound whose pressure amplitude is at most 0.1 atm inside the bath is used to prevent bubble nucleation that can give rise to the liquid pressure field contamination and the hydrophone damage from bubble collapse. Each measurement is performed during

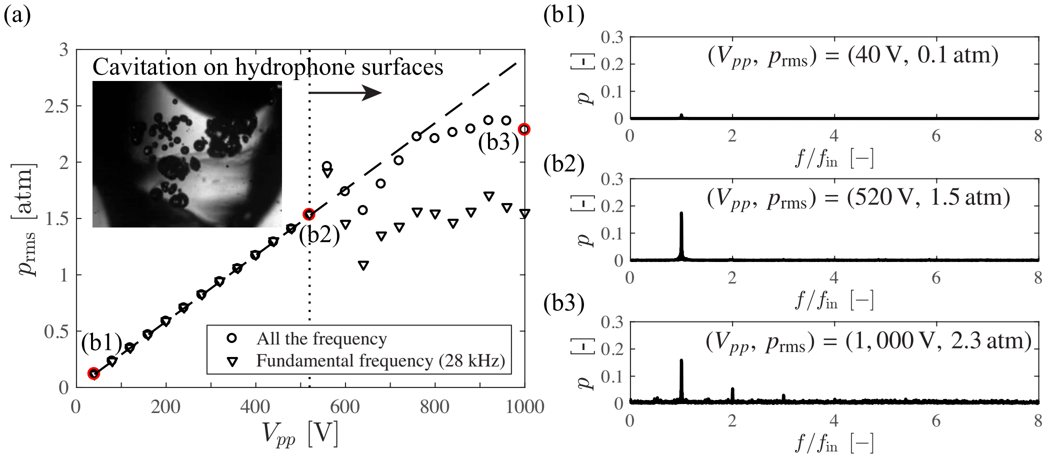

Fig 4.5: (a) Effective acoustic intensity of fundamental (driving) frequency and all the frequency as a function of input voltage. (b) Frequency spectra of acoustic emission under different effective acoustic intensity.

1-ms sonication and the root-mean-square value (or the effective value) of the pressure signal is extracted; this procedure is repeated ten times to calculate the average of the effective pressure intensity. The measurements showed that the pressure oscillations reach a steady state approximately 0.3 ms after the sonication starts (Fig. 4.4(a)). All the measurements are summarized in Fig. 4.4(b) that presents the distribution of the effective pressure intensity. It turns out that a standing-wave-like acoustic field appears along the z direction, which results from superposition of repeated wave reflections within the water column. Pressure antinodes appear around $z = \lambda/2$ and $z = \lambda$ (measured from the transducer), while one pressure node will appear exactly at the water surface ($z = 5\lambda/4$) that remains atmospheric and two more pressure nodes appear between the two antinodes ($z = 3\lambda/4$) and close to the transducer ($0 < z < \lambda/4$). We note that the acoustic intensity distribution is non-uniform in the x direction; such a multidimensional pressure field results from wave reflection from the side walls [232] and non-uniform ultrasound emission from the (finite-sized) transducer surface. In particular, the acoustic intensity at the pressure node ($z = 3\lambda/4$) near the z axis does not approach zero amplitude, which is the so-called damped standing wave [233].

Additionally, in order to examine nonlinearity of acoustic cavitation bubbles in bubbly structure, acoustic emission from the cavitation bubbles is measured at $(x, z) = (0, \lambda/2)$

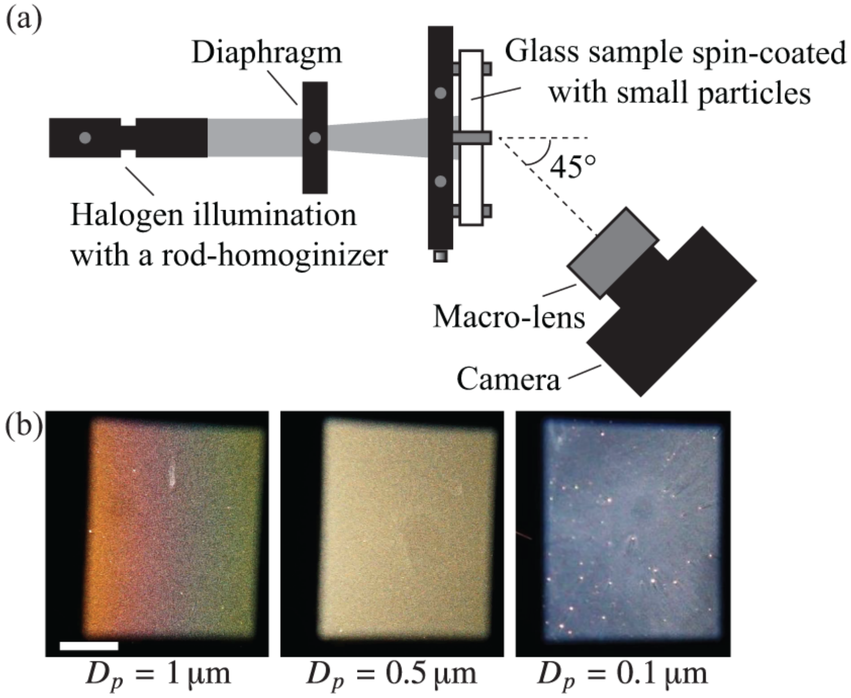

Fig 4.6: (a) Schematic of the optical system for the PRE measurement in a dark room. (b) Images of the scattered light from the glass sample with different particle diameters ($D_p = 1, 0.5$, and 0.1 μm). The scale bar shows 5 mm.

in the water with different ζ. Each measurement is performed during 5 ms sonication at a sampling frequency of 250 kHz. We extract the frequency spectra of the pressure signal, which is the average over a large number of acoustic emissions from the oscillating bubbles [234]. Figure 4.5(a) shows effective acoustic intensity p_{rms} of fundamental (driving) frequency and all the frequency as a function of input voltage V_{pp}. Below cavitation threshold $p_{\mathrm{rms}} \approx 1.5$ atm, p_{rms} linearly increases with V_{pp} and frequency spectrum contains only fundamental frequency (Figure 4.5(b1) and (b2)). With acoustic cavitation bubbles nucleated above the threshold, p_{rms} nonlinearly increases with V_{pp} and its component of the fundamental frequency suddenly decreases. Then the harmonic frequencies begin to emerge and their intensity grow as input voltage is increased (Figure 4.5(b3)). Thus, the acoustic emission at subharmonic and ultraharmonic peaks can be taken as the indictor of cavitation inception and the nonlinear level of the bubbles' oscillations, depending on the void fraction.

The glass sample spin-coated with the small particles (see Section 4.2.2) is immersed vertically into the bath and its center is located at the pressure antinode at $z = \lambda/2$, where cleaning effects are expected to be maximal. A cramp (not depicted in Fig. 4.2(a)) is used to position the glass sample in the cleaning spot (see Fig. 4.2(b)). The power inputted to the transducer is tuned to obtain $p_{\mathrm{rms}} = 1$ atm at the pressure antinode $z = \lambda/2$ for the case of saturated water ($\zeta = 0$). When the glass samples coated with the three-sized particles are sonicated under $p_{\mathrm{rms}} \mid_{z=\lambda/2}= 1$ atm in the saturated water ($\zeta = 0.0$), each cleaning efficiency (obtained from haze method in Section 4.2.4) is achieved about 10% in maximum. Thus the fixed power input is adopted for all the subsequent experiments. See Appendix E for cleaning tests under higher ultrasound intensity at $p_{\mathrm{rms}} = 1.4$ atm. Note that this sonication intensity (1 atm) is lower than that in commercial ultrasonic cleaning baths (several atm). The sonication with the fixed power is applied continuously for 30 s to each sample. Finally we note that the DO saturation level in the water remains unchanged before and after the sonication. In other words, the effect of ultrasonic degassing is minor in this sonication period (30 s).

4.2.4 Evaluation of the ultrasonic cleaning efficiency and cavitation erosion

In order to evaluate the concentration field of the surface-attached particles, scattered light from the glass sample in a dark room is captured by a digital camera (ILCE-6000, Sony) equipped with a macro-lens (SEL30M35, Sony) at 45° from back illumination by a halogen lamp (SHLA-150, Sigma Koki) (see Fig. 4.6(a) for the optical setup), which is the so-called haze method [235,236]. The light passes through a rod homogenizer (RHO-13S-E2, Sigma Koki) and shows a rectangular projected area (15 mm × 15 mm) on the sample. The captured images in Fig. 4.6(b) show that the particles are attached uniformly on the glass surface. Average intensity of the scattered light is measured using an image processing software ImageJ [237]. Under the assumption that there exists a proportionality between the light scattering intensity and the residual particle density, we define particle removal efficiency (PRE) according to

$$\mathrm{PRE} = \frac{\sigma_0 - \sigma}{\sigma_0} \times 100\ [\%]\,, \tag{4.1}$$

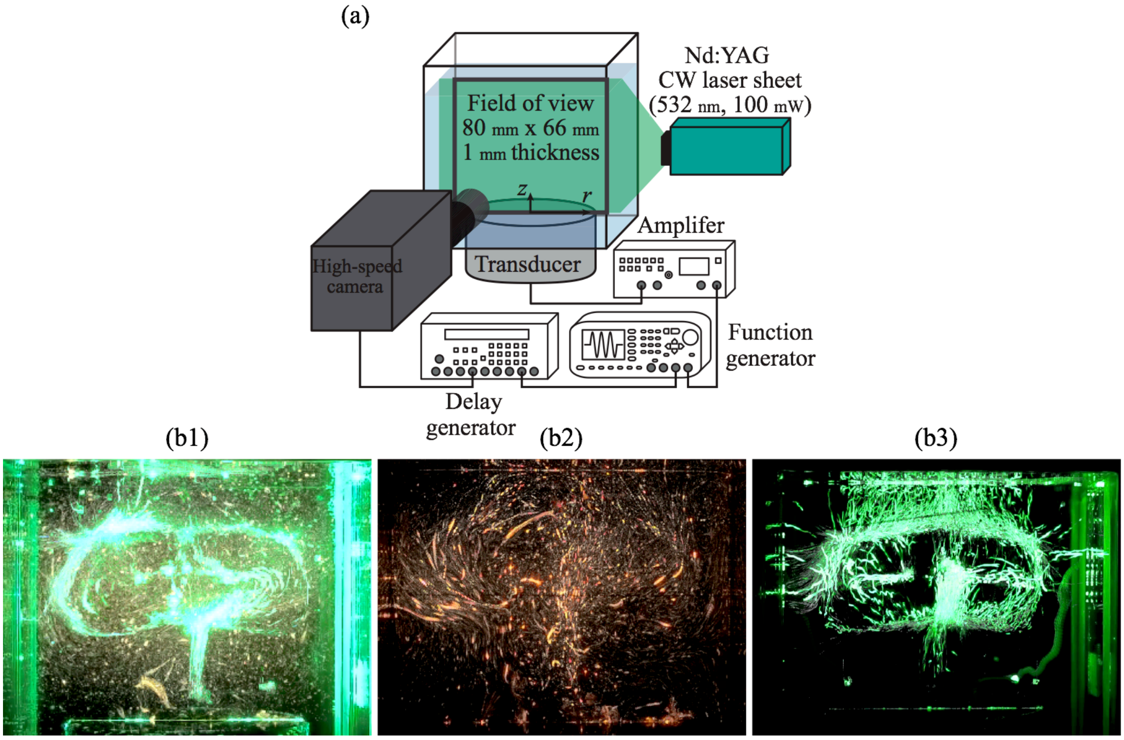

Fig 4.7: (a) Schematic and demonstrating images for the PIV analysis: (b1) Original image including both the fluorescence from the seeding particles and the scattered light from the cavitation bubbles. (b2) Fluorescence from the seeding particles captured by filtering the scattered light (green). (b3) Scattered light from the cavitation bubbles. Note that these images post-processed by analyzing the maximum intensity from the 3-s sonication.

where σ_0 and σ are the area-averaged intensities of the light scattering, respectively, before and after the cleaning tests.

In order to evaluate surface erosion by mechanical effects of cavitation bubbles, we perform the classical test [121,238–240], in which an aluminum foil (65 mm × 66 mm and 11 μm in thickness) is aligned with z axis in the bath and subjected to a continuous sonication for 10 s under the same power input to the transducer as in the cleaning tests.

4.2.5 Video recording of bubbly cavitation structure and individual bubble dynamics

Video recording at different scales is performed to visualize acoustic and fluid-dynamic phenomena associated with ultrasound-induced cavitation inside the cleaning bath. To explore the relation between the ultrasound-induced bubble dynamics and PRE (Section

4.2.2), the front view of bubbly cavitation structure with the glass sample immersed in the bath is recorded, at 60 frames per second (with exposure time of 1.33 ms), by high-speed camera units (VW-9000 and VW-300M, Keyence) equipped with a microscope (VW-Z5, Keyence). The spatial resolution is 163 μm per pixel. LED light sources (SLG-150V, Revox) are used as side lighting (see Fig. 4.2) in order to effectively capture light scattering due to the ultrasound-induced bubbles. The sonication and the video recording are synchronized through a digital delay generator (DG535, Stanford Research Systems). The same recording is repeated, but without the glass sample, for clearer visualization of bubbly cavitation structure.

Bubbly cavitating flow (for the case without the glass sample) is analyzed by PIV [241]. Fluorescent particles (FA-207, Sinloihi Co.) whose diameter and density are 4 μm and 1,300 kg/m^3, respectively, are seeded as tracers in the water in order to extract the liquid-phase velocity. According to [242], we confirm that our particles seeded in the liquid are so small that the hydrodynamic drag force overwhelms the acoustic radiation force; the particles' slip caused by the acoustic radiation force is expected to be negligible. See Appendix C for detailed calculation of the threshold diameter of the seeding particles. An Nd:YAG CW laser sheet (G100-KA, Kato Koken Co.), whose wavelength, thickness, and mean energy are 532 nm, 1 mm, and 100 mW, respectively, is illuminated along the z-axis from the top. A filter is used to reduce scattered light of 532 nm from the cavitation bubbles. The fluorescence (610 nm) is recorded, at 60 frames per second (with exposure time of 4 ms) by the high-speed camera units (VW-9000, VW-300M, and VW-Z5, Keyence). A field of view of the recording is set in the range of $-40 \leq x \leq 40$ mm and $0 \leq z \leq 66$ mm with the resolution of 155 μm per pixel. The recording is performed for the 10-s sonication (with the same power input to the ultrasound transducer) that is applied to the water with different ζ. PIV analysis, using a commercial software (Flow Expert 2D2C, Kato Koken Co.) with a direct cross correlation method, is applied to the recorded images and the evolution of the liquid velocity averaged over 10 frames is obtained every 10 frames. In addition, the bubbles' translation is analyzed by tracking their scattering of the

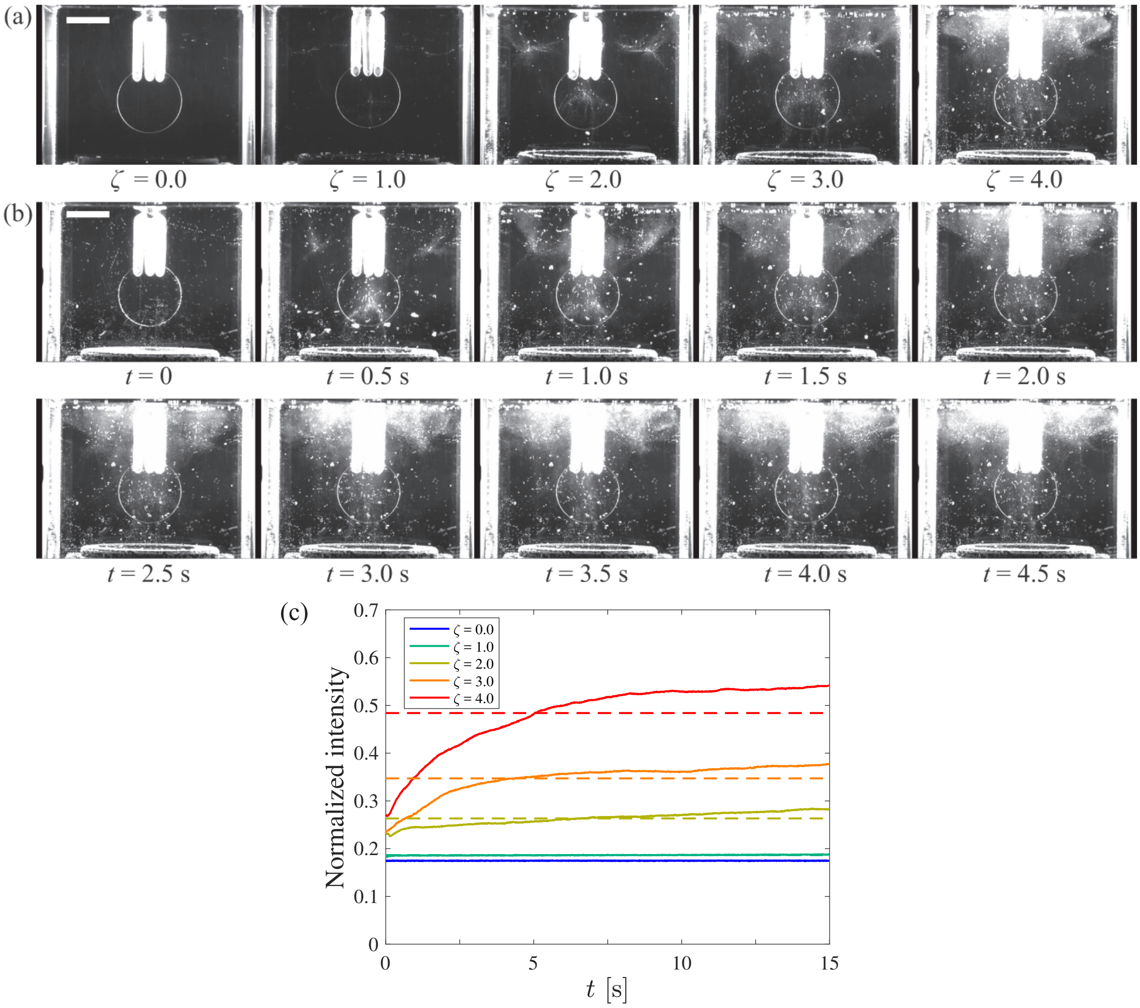

Fig 4.8: (a) Typical snapshots of steady-state bubbly structure of acoustic cavitation in the water (at DO supersaturation ζ = 0.0, 1.0, 2.0, 3.0, and 4.0) with the cleaning sample (2.5 s after the sonication started). (b) Initial evolution of the cavitation structure at DO supersaturation ζ = 4.0. Each scale bar shows 20 mm. (c) Evolution of the normalized intensity of the scattered light from the cavitation bubbles.

laser sheet in the x-z plane. In this case, the fluorescent particles are not added to the water. Here, the scattered light is recorded, at 1,000 frames per second (with exposure time of 998 μs), by a high-speed camera (FASTCAM SA-X2, Photron) equipped with a lens (AI AF Zoom-Nikkor 80–200mm, Nikon) and a teleconverter (Teleplus MC7, Kenko). The recording is performed for the 5-s sonication (with the same power input). A field of view of the recording is set at $-40 \le x \le 40$ mm and $0 \le z \le 66$ mm with the resolution of 110 μm per pixel.

Finally, the dynamics of individual bubbles nucleated at the glass surface near the pressure antinode (at $z = \lambda/2$) are recorded, at 200,000 frames per second (with exposure time of 4 μs), by the high-speed camera (FASTCAM SA-X2, Photron) equipped with a lens (CX-5040SZ, Hirox). Its optical system is similar to Fig. 4.2, but with the back illumination, instead of the side illuminations. The spatial resolution is 3.0–9.2 μm per pixel. Technically, DO-supersaturated water ($\zeta > 0$) is used to promote bubble nucleation at the sample surface. Surface-attached bubble nuclei are first captured by the camera and the subsequent dynamics driven by the sonication are recorded by the high-speed camera. Note that the rectified mass diffusion does not play a role during this observation period. Moreover, to see whether the particle removal is achieved by the bubble dynamics, the largest-sized ($D_p = 1$ μm) particles of density approximately at 2,000 kg/m^3, are tracked via light scattering from the 30°-off-axis back illumination.

4.3 Results and discussion

4.3.1 Macroscopic observation of cavitation in the bath

First, we present the macroscopic observations of (steady-state) cavitation activity that was recorded at $t = 2.5$ s after the sonication started. Figure 4.8(a) shows entire view of the cavitation activity in the water (DO supersaturation $\zeta = 0.0$, 1.0, 2.0, 3.0, and 4.0) with the cleaning sample. We can clearly see that there appears a larger number of (visible-sized) cavitation bubbles in the bath as ζ increases, meaning a reduction in the cavitation inception threshold under DO supersaturation. This tendency is quantified by analyzing the intensity of the scattered light from the cavitation bubbles (see Fig. 4.8(c)). For the cases of $\zeta = 0.0$ and 1.0, the intensity remains unchanged, which originates from the scattered light from the cramp or acrylic wall. However, when $\zeta \geq 2$, the evolution rate of the intensity is enhanced due to the higher nucleation rate under higher DO supersaturation. Under higher DO supersaturation, there will exist a larger number of oxygen bubble nuclei stabilized in the water or at the bath and the rectified mass diffusion rate will be augmented under the sonication. It is also interesting to note that the surface tension is reduced under gas supersaturation [170, 171] and cavitation can in principle occur more easily.

For the cases of $\zeta = 2.0$ and 3.0, we can see jellyfish structures (the so-called Acoustic Lichtenberg Figure [134,243–245]) around $(x, z) = (0, \lambda/2)$ and $(\pm R_T, \lambda)$ where the pressure amplitude has the local maximum (see Fig. 4.4) and bubbles smaller than the resonant size are thus expected to migrate toward its center [50,246]. When the DO supersaturation is further increased to $\zeta = 4.0$, the population of cavitation bubbles seems to be dense enough to absorb a large part of the incident ultrasound and thus these bubbles destroy the standing-wave-like acoustic field as observed in Fig. 4.4. This may support the fact that the jellyfish structure does not appear in the highest supersaturation case.

In Fig. 4.8(b), we present the transient evolution of the cavitation activity for the case of the highest DO supersaturation ($\zeta = 4.0$); see also Appendix D with and without the cleaning sample (for the cases of $\zeta = 0.0, 1.0, 2.0, 3.0$, and 4.0) as supplemental materials. Before the steady state (Fig. 4.8(a)) is achieved roughly at $t = 2.5$ s, the population of visible-sized bubbles is gradually increased via the rectified mass diffusion. Before the sonication ($t = 0$), the transducer's surface shows significant light scattering (due to a large number of oxygen bubble nucleation under the DO supersaturation) and is thus a major nucleation site for the cavitation bubble. Shortly after the sonication starts (say, up to $t = 1$ s), bubbles nucleated from the transducer's surface translate upward, i.e., in the direction of the incident ultrasound propagation and form a jellyfish structure around $(x/R_T,\ z/\lambda)= (0,1/2)$ and $(\pm 1,1)$ as simulated by Louisnard [247]. Thereafter, the bubble population is further increased via the rectified mass diffusion and becomes dense enough to destroy the standing-wave-like acoustic field in the bath. It is expected that a large amount of the ultrasound energy from the transducer is absorbed into cavitation bubble dynamics and the incident wave thus shows a significant decay before reaching the water surface or the bath wall, leading to the formation of a traveling-wave-like acoustic field, not a standing-wave-like one [247]. Under such a traveling-wave-like field, bubbles are no longer trapped midway and show a strong bubbly streaming after the steady state is achieved, say, at $t = 2$ s. These bubbles either escape from the water through the free surface or circulate inside the bath; the bubbles' translation (and the induced liquid

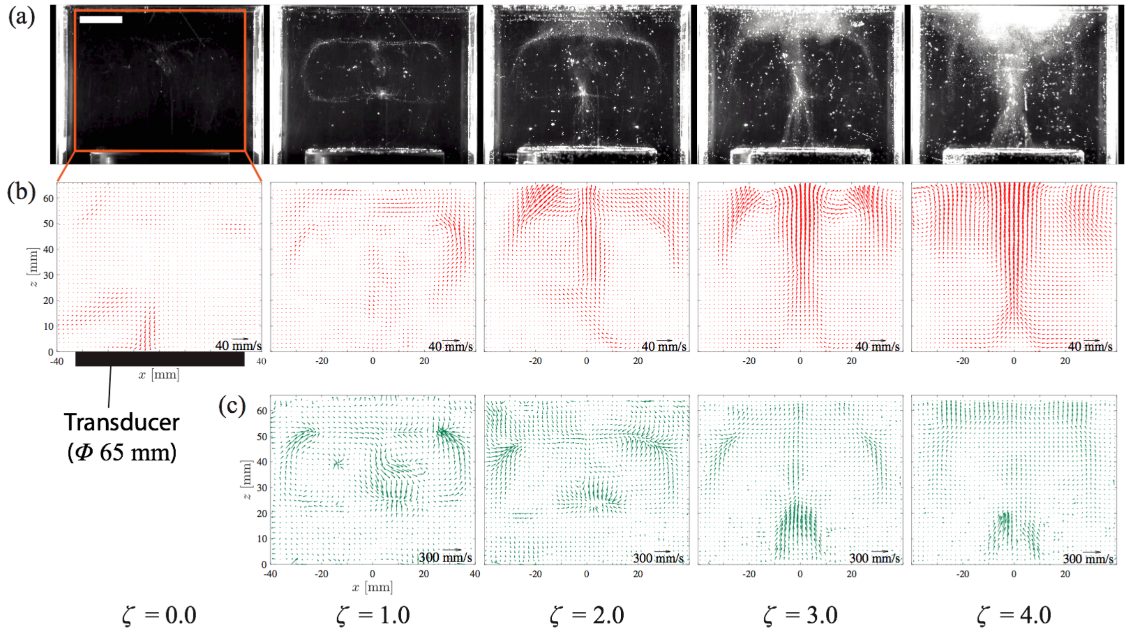

Fig 4.9: (a) As Fig. 4.8(a), but without inserting the cleaning sample. The scale bar shows 20 mm. (b) Liquid-phase velocity field extracted from the PIV analysis based on the fluorescent particles. (c) Translating bubbles' velocity field extracted from the PIV analysis based on the light scattering from the bubbles.

motion) without the cleaning sample will be examined by PIV in Section 4.3.2. Finally, we note again that the DO supersaturation was almost unchanged before and after the sonication; namely, the sonication period was short enough to ignore ultrasound degassing effect.

Finally, we report on the phenomenon in the bath after the sonication stopped If the DO supersaturation is sufficiently high (say, $\zeta > 2$), strong light scattering appears after the sonication and its intensity looks almost uniform within the bath. In this case, acoustic waves propagating and reflecting within the bath are expected to be damped via bubble-dynamic dissipation soon after the sonication stopped, implying that the primary Bjerknes force disappears in the post-sonication phase. That is, bubbles grow gradually under the supersaturation and tend to be distributed uniformly within the bath.

4.3.2 PIV analysis of liquid flow and bubbles' translation

To more clearly see liquid flow and bubbles' translation in the bath, we performed the same experiment as in Section 4.3.1, but without the cleaning sample. In Fig. 4.9(a),

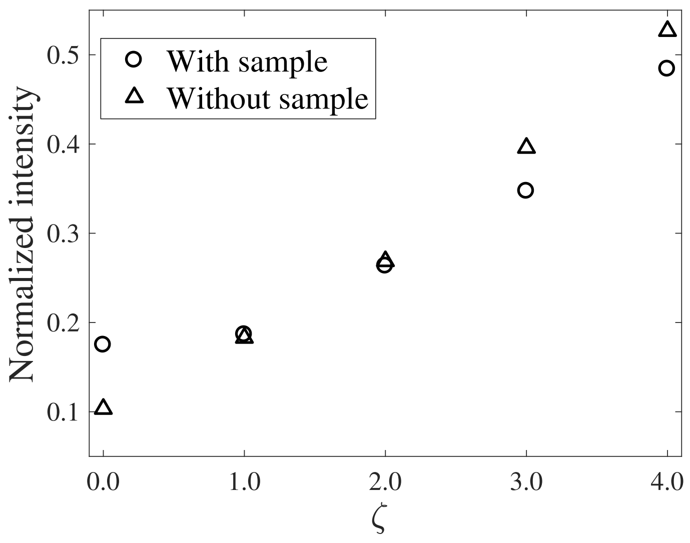

Fig 4.10: Normalized intensity of the scattered light from the cavitation bubbles with and without inserting the cleaning sample in Fig. 4.8(a) and 4.9(a), respectively, as a function of DO supersaturation ζ.

we present the images of the steady-state cavitation activity that were recorded with the LED side lighting. We postprocessed the scattered light from cavitation bubbles with and without inserting the cleaning sample, in (the movie version of) Fig. 4.8(a) and 4.9(a), respectively, with imageJ, calculated the average of the scattering intensity over the sonication time (15 s) and the captured area (65 mm × 66 mm), and plotted it as a function of DO supersaturation ζ in Fig. 4.10. As expected, the light scattering intensity, for both cases of with and without inserting the cleaning sample increases, monotonically as the supersaturation increases, supporting our claim that the cavitation inception threshold can be reduced by having higher DO supersaturation. For PIV analysis, as explained in Section 4.2.5, we used the green laser sheet, instead of the LED lighting; the liquid-phase velocity, $\bar{\mathbf{u}} = (\bar{u}_x, \bar{u}_z)$, was calculated based on the fluorescent particles seeded in the water and the velocity of translating bubbles, $\bar{\mathbf{v}} = (\bar{v}_x, \bar{v}_z)$, was extracted from light scattering from the bubbles.

We summarize the velocity fields of the liquid (with varying ζ) and the bubbles, respectively, in Fig. 4.9(b) and (c). For the case of the saturated water ($\zeta = 0.0$), visible-sized bubbles did not appear and the light scattering was insufficient for the PIV analysis; the velocity field of the bubbles cannot be defined. In this case, the liquid is found to

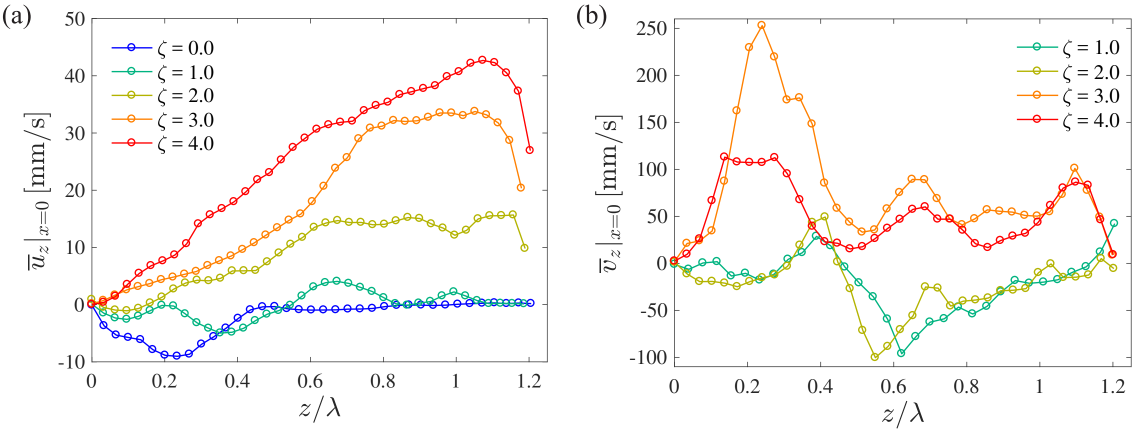

Fig 4.11: Distribution of the averaged z-velocity (at $x = 0$) obtained from the PIV analysis in Fig. 4.9: (a) liquid-phase velocity $\overline{u}_z$ and (b) translating bubbles' velocity $\overline{v}_z$.

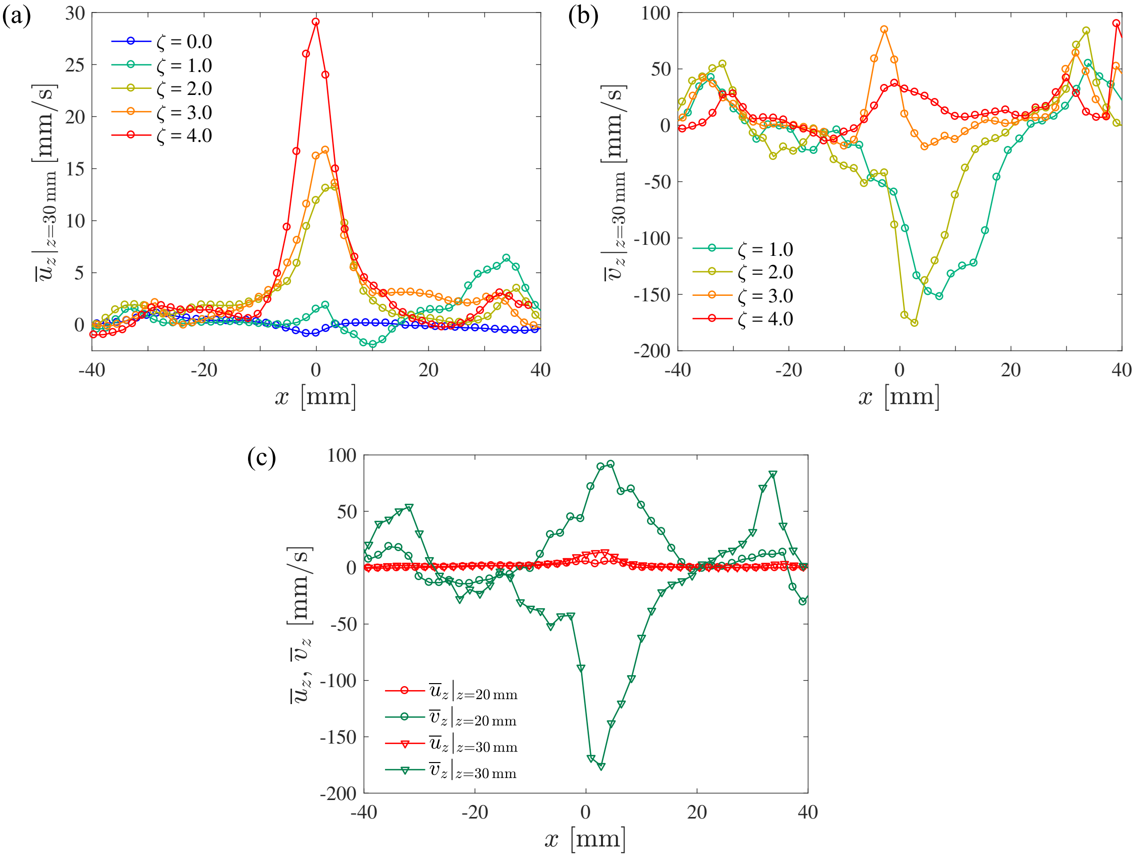

Fig 4.12: Distribution of the averaged z-velocity (at $z = 30$ mm) obtained from the PIV analysis in Fig. 4.9: (a) liquid-phase velocity $\overline{u}_z$ and (b) translating bubbles' velocity $\overline{v}_z$. (c) Comparison of $\overline{u}_z$ and $\overline{v}_z$ at $z = 20$ and 30 mm at $\zeta = 2.0$.

be essentially stagnant, which is consistent with the fact that acoustic streaming in water (having no bubbles) is very weak for the case of low-frequency (say, several 10 kHz) ultrasound. On the other hand, once visible bubbles appear in the water under the higher

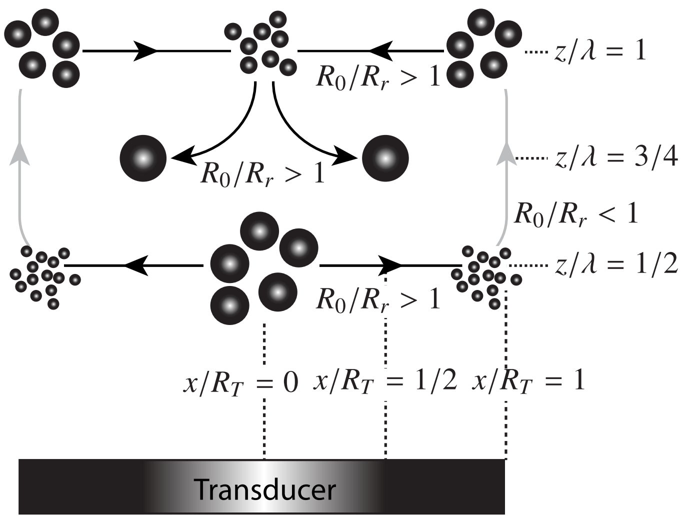

Fig 4.13: Illustration of the translation directions of bubbles (of equilibrium radius R_0) for the cases of DO supersaturation $\zeta = 1.0$ and 2.0 ($0 \leq r/R_T \leq 1$ and $1/2 \leq z/\lambda \leq 1$). Superresonant-sized bubbles ($R_0 > R_r$) translate toward the pressure node (black lines) but subresonant-sized bubbles ($R_0 < R_r$) translate toward the pressure antinode (gray lines).

DO supersaturation, the liquid streaming is built up and its structure looks similar to the bubbles' streaming. This suggests that the liquid phase is entrained by bubbles translating by the primary Bjerknes force. However, the entrainment effect is rather limited; the liquid-phase velocity is one-order-magnitude lower than the bubbles' velocity. Upward liquid streaming becomes dominant under higher DO supersaturation. Such upward streaming is generated under the ultrasound intensity gradient caused by populated cavitation bubbles [60]. The relatively-slow streaming of liquid is expected to continuously generate shear flow on the cleaning target, which may possibly assist in preventing reattachment of removed particles from the cleaning sample [248]. In Fig. 4.11, we plot the averaged z-velocity along z-axis (at $x = 0$) , obtained from the PIV analysis (Fig. 4.9) of the velocity fields from both the liquid and bubbles. The upward liquid streaming from the transducer becomes faster as the DO supersaturation increases (see Fig. 4.11(a)). In Fig. 4.12, we plot the averaged z-velocity along x-axis (at $z = 0.56\lambda$). For the cases of $\zeta = 1.0$ and 2.0 (where the standing-wave-like structure as in Fig. 4.4(b) is expected to exist), we see downward movement (or negative velocity $\bar{v}_z$) of bubbles around $z = 0.56\lambda$ (below the pressure antinode $z = \lambda = 53$ mm), which can be explained according to the primary Bjerknes force (see the following paragraph). Although the liquid streaming globally follows the bubbles translation, the liquid streaming does not partially correspond with that of the bubbles' streaming (see Fig. 4.12(c)). On the contrary, when bubbles are populated more densely ($\zeta = 3.0$ and 4.0 in Fig. 4.9(a)), the bubbles' entrapment becomes weak, meaning that the standing-wave-like pressure field is broken by dissipative effects associated with bubble dynamics. To be more specific, the energy of the ultrasound propagation from the transducer is effectively converted into dynamics of the densely populated bubbles, resulting in formation of the pressure field where the component of traveling waves is more dominant. The bubbles' upward translation from the transducer becomes faster as the DO supersaturation increases (see Fig. 4.9(c)), which is consistent with the observation that the primary Bjerknes force becomes stronger when the component of traveling waves is dominating over that of standing waves [247].

Finally, we carefully examine the bubbles' translation for the relatively low DO cases ($\zeta = 1.0$ and 2.0) with relevance to the pressure field; we can see bubbles trapped at the node and antinode of the standing-wave-like pressure field (as well as bubbles' translation between the node and antinode). In these cases, bubbles are less populated and the pressure field is expected to be similar to that for the case without bubbles (Fig. 4.4(b)). We now relate the PIV analysis in Fig. 4.9(c) and 4.12 to the pressure field for the case without bubbles (Fig. 4.4 (b)). Note that the resonant radius corresponding to the ultrasound frequency f is approximated by Minnaert's formula $R_r = \sqrt{3\gamma p_\infty/\rho_l}/(2\pi f) = 103\,\mu\text{m}$ [249], where $\gamma = 1.4$ is the ratio of specific heats for oxygen gas, p_∞ is the ambient pressure (one atmosphere), and $\rho_l = 998$ kg/m^3 is the water density. According to the primary Bjerknes force, oscillating bubbles translate along the acoustic intensity gradient; namely, superresonant-sized bubbles ($R_0 > R_r$ where R_0 is the equilibrium radius of gas bubble nuclei) translate toward the pressure node but subresonant-sized bubbles ($R_0 < R_r$) translate toward the pressure antinode (see Fig. 4.13). When oscillating bubbles experience pressure gradients in both the x and z directions, they will translate favorably toward the stronger gradient where the primary Bjerknes force is larger. Although the bubble size is not fully resolved in Fig. 4.9(a), the relatively larger bubbles are expected to have super-

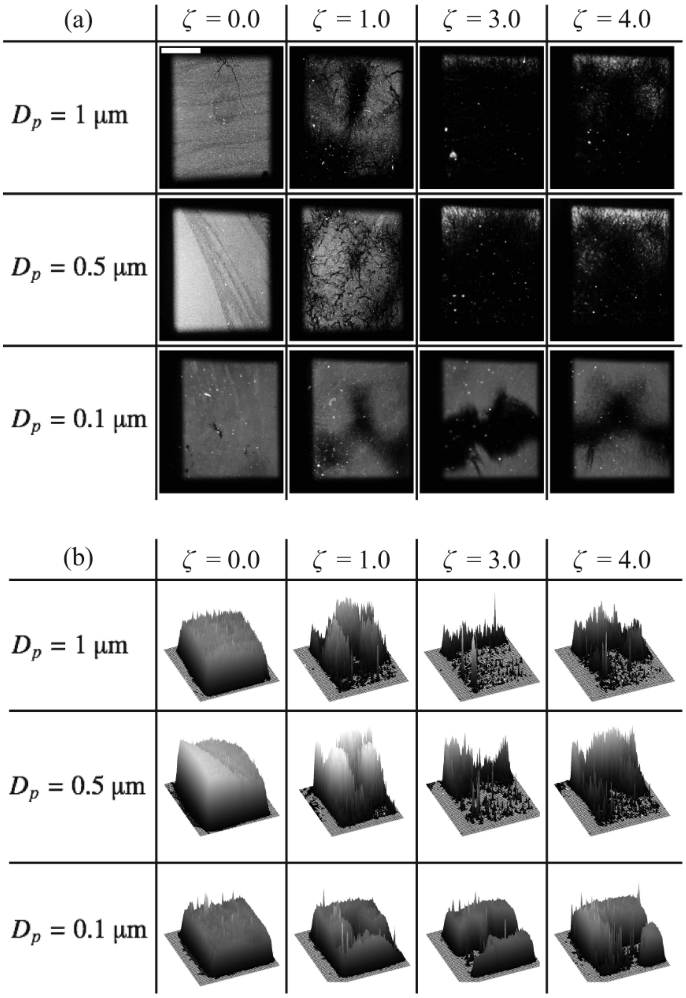

Fig 4.14: (a) Examples of the haze-method-based images of the backlight scattering from the cleaning sample (with different particle diameters D_p) after the 30-s sonication with varying the DO supersaturation ζ. The scale bar shows 5 mm. (b) Spatial distributions of the light scattering intensity from the haze-method-based images (a).

resonant size ($R_0 > R_r$) and some seem to be trapped at the node $z = 3\lambda/4$. It is interesting to note that around the pressure antinode $(x, z) = (0, \lambda/2)$, there exists an inflection point of the translating bubbles' velocity (see Fig. 4.11(b) and 4.12(c)), suggesting that oscillating bubbles are attracted, from its upper and lower points, toward the jellyfish's center. We speculate that this attraction is caused by the secondary Bjerknes force among densely populated bubbles in the jellyfish-structure cloud of bubbles.

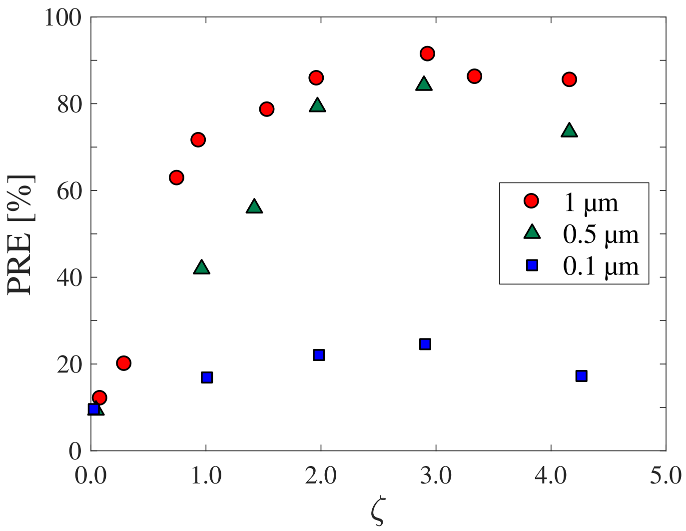

Fig 4.15: PRE from the ultrasonic cleaning tests as a function of DO supersaturation ζ.

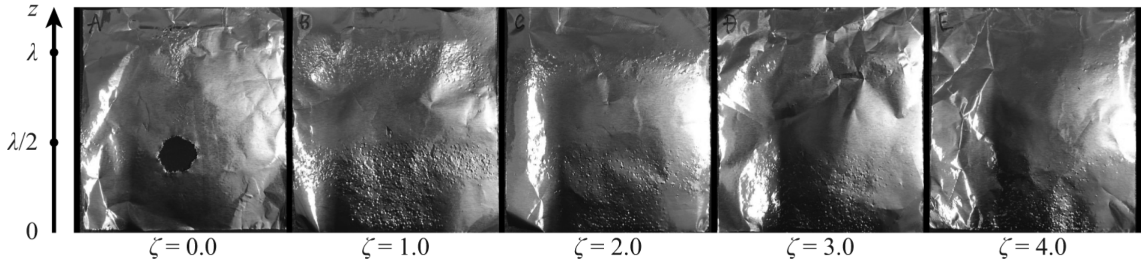

Fig 4.16: Cavitation erosion on an aluminum foil after the 10-s sonication under different DO supersaturation ζ.

4.3.3 PRE and erosion by the sonication in DO-supersaturated water

To evaluate the cleaning efficiency of the ultrasound irradiation in DO-supersaturated water, we present the haze-method-based images of the cleaning samples after the sonication; in Fig. 4.14(a), representative images of backlight scattering of the samples are presented with varying the DO supersaturation ζ and the particles' diameter D_p. We postprocessed these images with ImageJ and obtained the scattering intensity maps (see Fig. 4.14(b)), which allows us to define PRE according to Eq. (4.1). In Fig. 4.15, all the PRE results for each value of D_p are summarized as a function of ζ. The case of the saturated water (ζ = 0.0) results in very low PRE, regardless of the size of the attached particles. Noting that visible-sized cavitation bubbles do not appear in this case (Fig. 4.8(a)), mechanical actions directly from the 28-kHz ultrasound (such as fluid acceleration by instantaneous pressure gradients or acoustic streaming) do not play a major role in the particle removal, which is consistent with finding from the previous studies [29,32,33,77,87]. On the other hand, cavitation bubbles appear in the DO supersaturated water and their dynamics play a more important role as cleaning agents; the PRE becomes much higher in the supersaturated cases, provided that the particle size is large ($D_p = 1$ µm and 0.5 µm). Taking a careful look at the light scattering pattern in Fig. 4.14, we may say that cleaned spots appear preferentially in the vertical direction, particularly in the samples after the sonication with the supersaturated water. This suggests that bubbles advected vertically in the cleaning spot by the Bjerknes force, as observed in Section 4.3.2, contribute to the particle removal through their dynamics. It is interesting to note that there exists an optimal DO supersaturation to maximize PRE. In our cleaning tests, the optimal supersaturation is found approximately at $\zeta_{\mathrm{opt}} \approx 3$, regardless of the particle diameter D_p. We speculate that beyond the optimal DO supersaturation, the bubbles' population becomes large enough to absorb a large part of the energy of the ultrasound propagating from the transducer, which is consistent with the observation in Section 4.3.2 that bubbly streaming flow is augmented by increasing the DO supersaturation. Once the ultrasound attenuates in the cleaning spot, the forced oscillation of cavitation bubbles tends to be damped, giving rise to a reduction in their fluid-dynamic effects [250]. In other words, the optimal supersaturation is determined by the trade-off between individual bubble dynamics and bubbly streaming. We may say that, to be more specific, bubbly streaming where bubble oscillation is yet active is a key phenomenon toward realization of effective ultrasound cleaning. Finally, we discuss the case of the smallest particles ($D_p = 0.1$ µm) that resulted in the lowest PRE. We note that when it comes to modeling flow around such small particles, continuum assumptions may fail. When steep velocity gradients exist above solid surfaces, flow can slip, giving rise to a reduction in wall shear stress [251]. When the size of attached particles is approaching the slip length, shear stress acting on the particles may be smaller than the prediction from continuum theory equipped with the no-slip boundary condition.

To demonstrate the possibility of making the cleaning less erosive with the use of

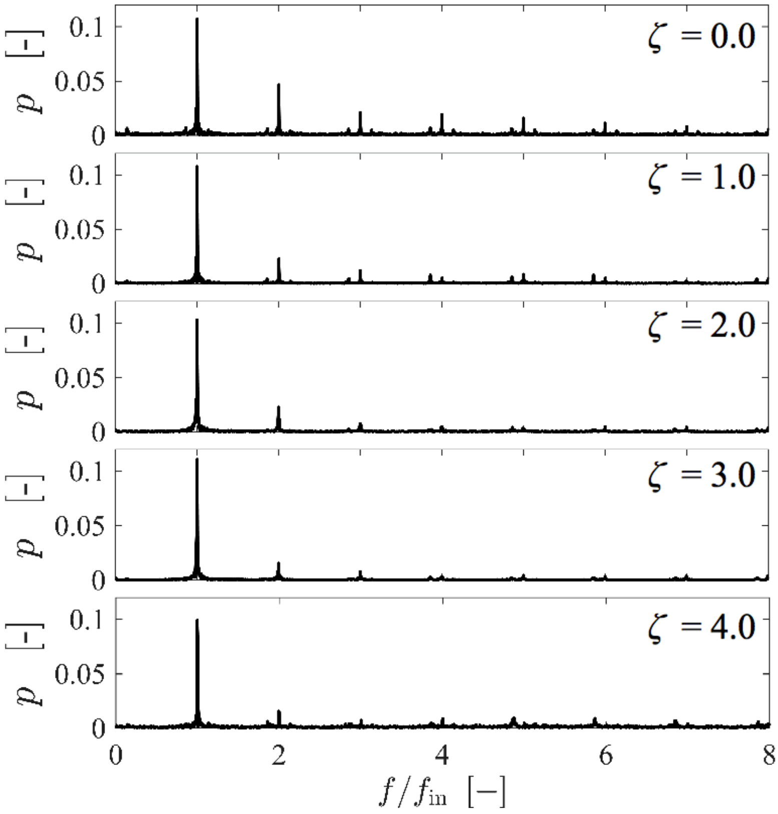

Fig 4.17: Frequency spectra of acoustic emission in the bath under different DO supersaturation.

DO-supersaturated water, we next present results of the erosion test using the aluminum foil; see Fig. 4.16. For the case of the saturated water ($\zeta = 0.0$), the large hole that is centered near the first pressure antinode (see Fig. 4.4(b)) at $(x, z) = (0, \lambda/2)$ was created by continuous attack from oscillating bubbles during the 10-s sonication. Also note that a number of micropits, rather than such a large hole, was created near the second pressure antinode at $(x, z) = (0, 3\lambda/2)$. Since the pressure amplitude at the second pressure antinode is lower, erosive effects of cavitation bubbles will become milder. However, once DO supersaturation is created in the cleaning solution, such a large hole created in the case of the saturated water does not appear. For the case of relatively low DO supersaturation ($\zeta = 1.0$ and 2.0), micropits appear preferentially near the first and second pressure antinodes. When the DO supersaturation increases further ($\zeta = 3.0$ and 4.0), the extent of micropits is reduced especially near the second pressure antinode. This definitely means that much of the ultrasound energy is absorbed into dynamics of cavitation bubbles that exist between the transducer's surface and the first pressure antinode. Namely, the DO supersaturation can contribute to mild bubble dynamics (and thus less erosive cleaning), but may give rise to less efficient cleaning as observed in the PRE results. Note that, even for the cases of the higher DO supersaturation, such micropits still appear near the transducer's surface, suggesting that more nucleation sites exist or stronger secondary Bjerknes force (attractive force on bubbles) appear on the edge of the aluminum foil whose roughness surpasses the lateral surfaces (captured surfaces). Finally, we point out the effect of DO supersaturation on individual bubble collapse. Since the content of cavitation bubbles under DO supersaturation is expected to be gaseous (not vaporous), their collapse will be milder, in comparison to vaporous bubble collapse, by compressibility of the (noncondensible) gas [150, 186, 187]. To be more precise, collapsing gaseous bubbles can rebound before reaching a very small collapse size (and a very fast collapsing speed) by high pressure of the compressed gas. As a result, shock emission from gaseous bubble collapse is believed to be weaker, which is another reason to support the result of smaller damage under higher DO supersaturation in our erosion test.

Figure 4.17 shows frequency spectra from acoustic cavitation bubbles in the water at different ζ over the sonication time (5 ms) under the same power input to the transducer as in the cleaning and erosion tests. As mentioned in Section 4.2.3, averaged acoustic emission from the individual bubbles shows frequency spectra whose subharmonic and ultraharmonic peaks can be taken as the indictor of cavitation inception and the nonlinear level of the bubbles' oscillations. Under the lower DO supersaturation (ζ = 0.0 and 1.0), peaks at harmonic and several ultraharmonic frequencies are observed over the whole frequency range. Ultraharmonic peaks are expected to be caused by acoustic emissions from bubbles smaller than the resonant size. We observe almost no broadband signal (namely, white-noise) and even subharmonic peaks, which originates from violent collapse of bubbles causing shock waves, supporting the relatively mild oscillation of gas bubbles under low-intensity ultrasound . When ζ is further increased, bumps at ultraharmonic frequencies decreases with increasing the DO supersaturation and harmonic component remains

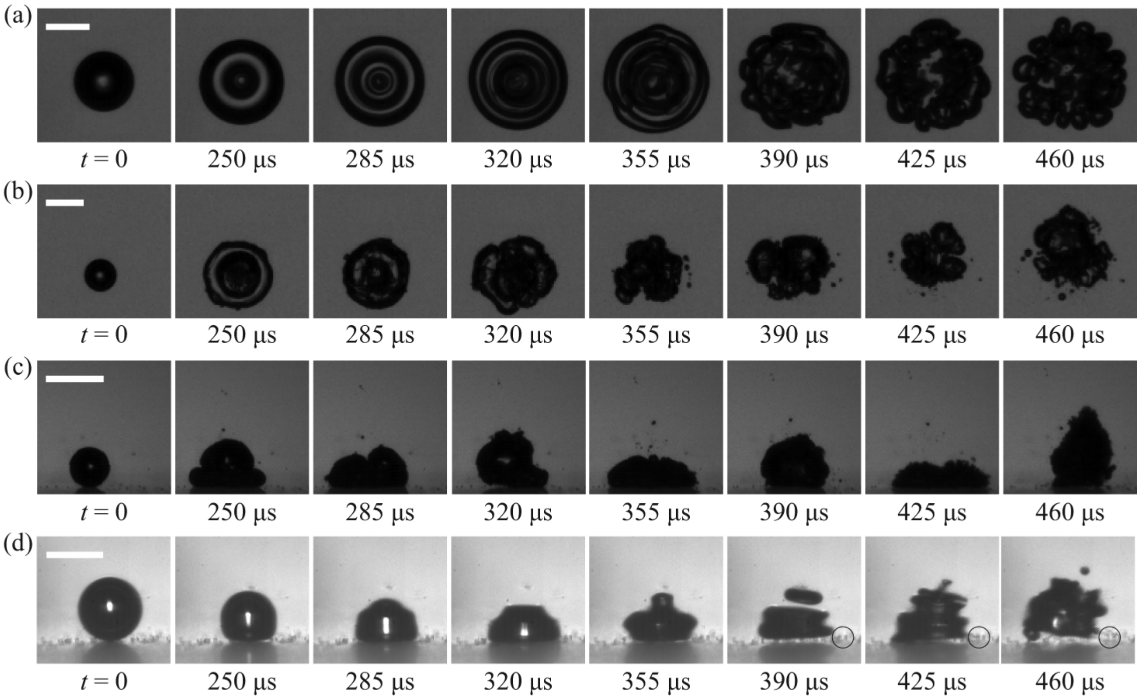

Fig 4.18: Evolution of the dynamics of individual surface cavitation in top view (normal to the glass surface): (a) $R_0/\hat{R}_r = 1.56$, (b) $R_0/\hat{R}_r = 1.14$, and in side view: (c) $R_0/\hat{R}_r = 1.22$. (d) Particle removal by single bubble oscillation ($R_0/\hat{R}_r = 0.8$). Each scale bar shows 200 µm.

unchanged. This suggests that, at higher DO supersaturation (namely, under higher void fraction), bubbles' oscillation becomes less intense due to attenuation of effective ultrasound energy and bubble-bubble interaction [44], which also supports the result of smaller damage under higher DO supersaturation in our erosion test.

4.3.4 Individual bubble dynamics at the glass surface

We report on observations of individual bubble dynamics on the sample under the same sonication amplitude as the cleaning test. Here, we put a focus on the dynamics of the resonant-sized bubble, which is expected to produce the major cleaning effect. Now that the bubbles of our concern is attached to the glass surface, the resonant radius is decreased from the Minnaert prediction R_r and may be approximated by $\hat{R}_r = 0.82R_r$ with the assumption that the glass surface is rigid and hydrophilic [252]. In Fig. 4.18(a), we present the temporal evolution of a surface-attached bubble (top view) whose radius is a bit larger than the resonant radius ($R_0/\hat{R}_r = 1.56$) just after the sonication starts. Note that this

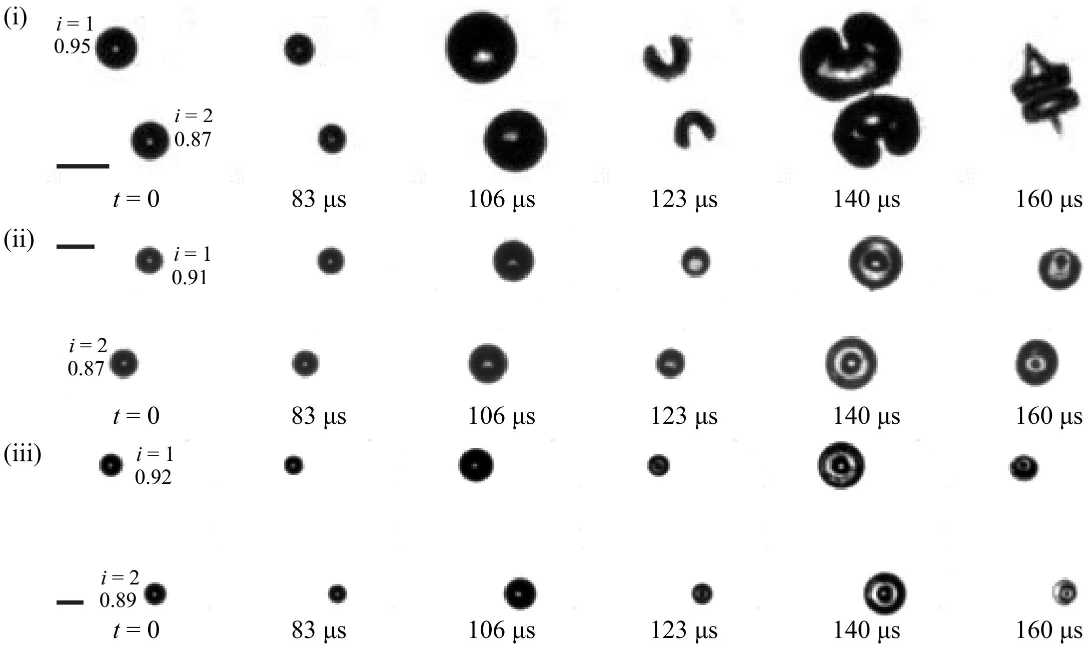

Fig 4.19: Evolution of the dynamics of two-equally-sized cavitation bubbles on surfaces in top view (normal to the glass surface) for the cases of different initial inter-bubble distances: (i) 374 µm, (ii) 552 µm, and (iii) 1.0 mm. The numbers in the first frame ($t = 0$) show $R_i(t = 0)/\hat{R}_r$ for each bubble. Each scale bar shows 200 µm.

bubble is located at the first pressure antinode ($z = \lambda/2$) and the pressure amplitude shows a transient increase in the observation period (see Fig. 4.4(a)). It follows that the dynamics of the bubble are nonspherical due to the existence of the glass surface in its neighbor [137], involving jetting toward the glass surface, fission, and cloud oscillation [253]. As the bubble size approaches further toward the resonant size ($R_0/\hat{R}_r = 1.14$), the bubble oscillation becomes more violent and its fission appears sooner (Fig. 4.18(b)). It is important to note that the bubble images in Fig. 4.18(a) and Fig. 4.18(b) remain clear (without a blur) during the observation period. This indicates that the oscillating bubbles keep their position near the rigid boundary via the secondary Bjerknes force that arises from interaction with the imaginary bubble at the opposite side of the boundary [254,255], this fact is indeed confirmed by the side view of a surface bubble near the resonant condition (see Fig. 4.18(c)) and is of great importance to achieve cleaning effect continuously from the dynamics of surface cavitation bubbles. The effective stand-off distance from the single bubble collapse is well-documented in a previous study [33]. Figure 4.18(d) shows the side view of the bubble dynamics ($R_0/\hat{R}_r = 0.80$) on the glass surface. Once the

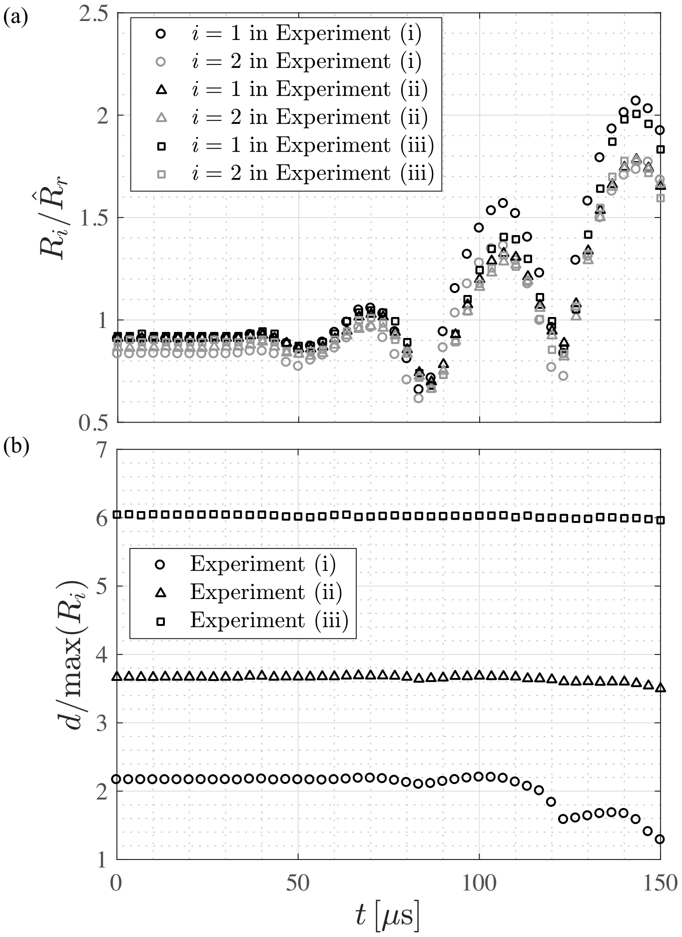

Fig 4.20: Evolution of (a) nondimensional radii $R_i/\hat{R}_r$ and (b) nondimensional inter-bubble distance between the bubbles centres $d/\max(R_i)$ as a function of time for each bubble obtained from Fig. 4.19.

cloud is formed between $t = 425\,\mu$s and 460 µs, we can clearly see effective removal of particles ($D_p = 1$ µm in diameter) as suggested in [256]; the removed particles are marked with a black circle in the figure.

The case of two surface-attached bubbles with equally sized of the resonant radius ($R_0/\hat{R}_r \approx 1$) are shown in Fig. 4.19 and 4.20 under three different initial inter-bubble distances: (i) 374 µm, (ii) 552 µm, and (iii) 1.0 mm. These oscillating bubbles are attracted via the secondary Bjerknes force [47,48] and the inter-bubble distance d becomes shorter as time progresses whose acceleration becomes larger when initial inter-bubble distance is shorter. For the case of the strong bubble-bubble interaction in experiment (i), the displacement of each bubble's centre can be clearly seen to follow its radial oscillation: attracts and repels each other during its expansion and shrink, respectively. At

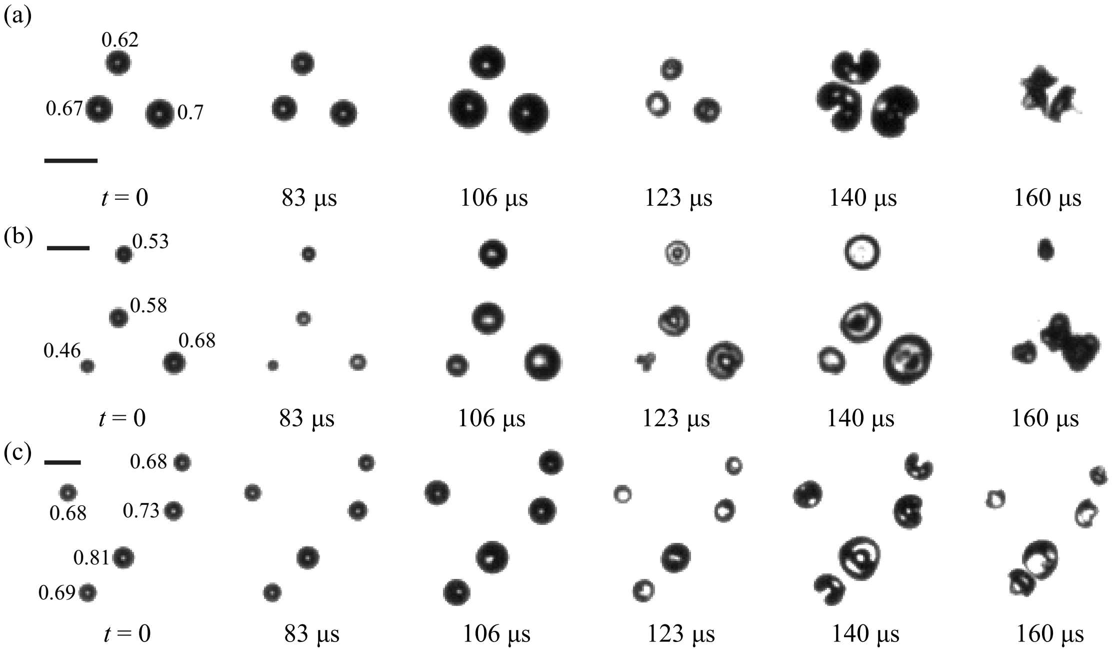

Fig 4.21: Evolution of the dynamics of multi cavitation bubbles on surfaces in top view (normal to the glass surface) for the cases of (a) three bubbles, (b) four bubbles, and (c) five bubbles. The numbers in the first frame ($t = 0$) show $R_i(t = 0)/\hat{R}_r$ for each bubble. Each scale bar shows 200 µm.

$t = 123$ µs and 140 µs, the bubbles' collapse accompanies reentrant jet formation due to the strong bubble-bubble interaction. Eventually, these bubbles merge at $t = 160$ µs. While the direction of the reentrant jet is normal to the wall in the cases of single bubble collapse or relatively weak bubble-bubble interaction as in experiment (ii) and (iii), these jets are attracted as well through the bubble-bubble interaction and their direction is thus tilted as in experiment (i) [257–259]. This tendency depends on the relative strength of the secondary Bjerknes force from nearby bubbles or nearby solid surfaces (mirror effect). As a result of the tilted jet impact against the wall, the bubble-bubble interaction, which plays a more important role among more populated cavitation bubbles at the higher DO supersaturation, will result in suppression of both the generated wall shear stress (cleaning effect) and water-hammer pressure (damaging effect), supporting the dependency of PRE and erosion on the supersaturation (see Section 4.3.3). The case of multi surface-attached bubbles (three-bubbles, four-bubbles, and five-bubbles) with equally sized less than the resonant radius ($0.5 < R_0/\hat{R}_r < 1$) are shown in Fig. 4.21. When $d/\max(R_i) < 5$,

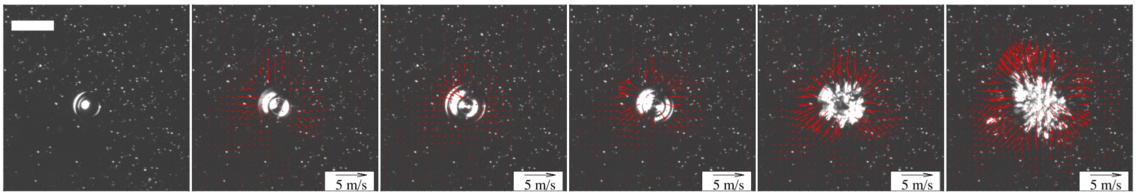

$t = 0$ 70 μs 75 μs 80 μs 130 μs 250 μs

Fig 4.22: Images of the particles (white dots) of $D_p = 1$ μm in the vicinity of an oscillating bubble of $R_0 = 0.78\hat{R}_r = 66$ μm at different times after the sonication starts. The velocity field of the removed particles (red arrows) are obtained by PIV analysis. The scale bar shows 200 μm.

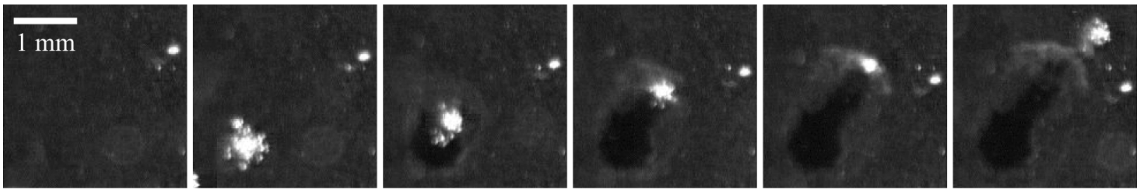

$t = 0$ 1 ms 2 ms 3 ms 4 ms 5 ms

Fig 4.23: Macroscopic images of the particles removal (white dots) of $D_p = 1$ μm in the vicinity of an oscillating cloud of bubbles .

individual bubble initially moves toward and merge with the nearest bubble, and then the merged bubbles subsequently attract with each other, forming a single cloud of bubbles. This suggests the cloud dynamics is dominant for the case of more populated cavitation bubbles at the higher DO supersaturation due to the strong bubble-bubble interaction.

Finally, we apply PIV analysis based on the scattering light from the largest particles ($D_p = 1$ μm in diameter) removed by the dynamics of a surface cavitation bubble $R_0/\hat{R}_r = 0.78$ (Fig. 4.22). Here, the oblique backlighting was used to track motion of the removed particles, so that the bubble image becomes unclear. Yet, we can confirm that the bubble shows nonspherical dynamics (including jetting and fission) as observed in Fig. 4.18. The scattering light was recorded in the direction normal to the glass surface. Since the lens has a depth of field (≈ 100 μm), comparable to the bubble size, spatially-averaged liquid velocity in the tangential direction approximately 100 μm above the glass surface can be extracted from the captured particle images as PIV tracers. The instantaneous liquid flow is built up by the oscillation of the resonant-sized bubbles or a cloud of split bubble fragments; the visible range of the induced flow is found to be several times larger than the bubble size [260]. The liquid flow (outward/inward) pulsation is also found to be in phase with the bubble (growth/shrinkage) oscillation, for the liquid's velocity field is essentially incompressible. After the sonication, the removed particles are advected away from the sample [260–262] perhaps by microstreaming from the bubble oscillation (see Fig. 4.23).

4.4 Conclusions

In summary, we experimentally clarified, from both macroscopic and microscopic observations, the role of cavitation bubbles in ultrasonic cleaning from our tests with varying DO supersaturation in water.

From the macroscopic observation, we obtained the findings as follows. The cavitation inception threshold is reduced by having higher DO supersaturation in the water, so that the population of cavitation bubbles is increased. As the bubble population becomes denser, the bubbles' advection is found to be strengthened by the primary Bjerknes force. The liquid flow is induced by entrainment effect of the moving bubbles but is rather limited in our tests. However, we may say that the liquid streaming may possibly assist in preventing the reattachment of removed particles. It is found from the PRE result that the particle removal is achieved mainly by the action of cavitation bubbles, but there exists the optimal supersaturation to maximize the cleaning efficiency, which is determined by the trade-off relation between individual bubble dynamics and bubbly liquid steaming. Furthermore, it follows from the simple erosion tests with aluminum foils that DO supersaturation could play a role in minimizing cavitation erosion with milder bubble dynamics.

From the microscopic observation of individual bubble dynamics, we confirm that cloud dynamics of split bubble fragments play a dominant role in particle removal. As a result of the tilted jet impact against the wall, the bubble-bubble interaction, which plays a more important role among more populated cavitation bubbles at the higher DO supersaturation, will result in suppression of both the generated wall shear stress (cleaning effect) and water-hammer pressure (damaging effect), supporting the dependency of PRE and erosion on the supersaturation. In conclusion, our findings suggest that low-intensity ultrasound irradiation under optimal gas supersaturation in cleaning solutions allows for having mild bubble dynamics (without violent collapse) and thus cleaning surfaces effectively with minimal cavitation erosion.

In the present study, we put a focus on the case of low-frequency ultrasound that matters in degrease cleaning. The present finding indicates that the use of dissolved gas supersaturated water is also useful in the case of higher-frequency ultrasound such as megasonic cleaning for silicon wafers. The cavitation inception threshold even for the case of megasonic waves can in principle be reduced under the supersaturation, which allows for nucleating bubbles with lower-intensity acoustic power and thus for less erosive cleaning with milder bubble dynamics. Stronger acoustic bubbly flow is expected under the higher-frequency ultrasound irradiation and may contribute to more efficient particle removal.

Chapter 5

Conclusions and outlook

5.1 Conclusions

In this thesis, we have investigated the gas bubble nuclei driven by mass diffusion under gas supersaturation, and acoustics cavitation with underwater ultrasound and gas supersaturation. The overall objective of this thesis was to experimentally develop an erosion-free ultrasound cleaning technique with the aid of cleaning solutions that are supersaturated with dissolved gases.

First, to study whether nitrogen gas originally dissolved in water can be purged by aeration with oxygen microbubbles, we devised a technique to measure the concentration of DN. Oxygen microbubbles were continuously injected to the circulation system of tap water that was originally saturated with gases at one atmosphere or was first aerated with nitrogen microbubbles. The gradual growth of a surface-attached bubble in the aerated water was visualized and was then compared with the extended Epstein–Plesset theory that accounts for mass diffusions of multiple gas species. In the comparison, the (unknown) DN concentration is treated as a fitting parameter. It follows from the fitting that the DN can be effectively purged by the oxygen aeration, regardless of the initial state of dissolved gases in the water. From the supplemental experiment, such a purging effect was confirmed also in the case of aeration with nitrogen microbubbles. We say that these purging effects, which are well known particularly in food industry and fishery, can be evaluated quantitatively by our technique based on the bubble growth observation and its fitting to the extended Epstein–Plesset theory.

Second, to relate DO supersaturation to the probability of having cavitation bubble nucleation, we irradiated green pulse laser to the DO-supersaturated water in order to trigger gas bubble nucleation. It follows from a series of the experiments with varying the DO supersaturation (and the laser energy) that the number of nucleated gas bubbles increases as the DO supersaturation increases, implying that the number of stable gas bubble nuclei attaching at contaminant particles is augmented under the supersaturation. As expected, the nucleation threshold is reduced by increasing the DO supersaturation.

Finally, we experimentally clarified, from both macroscopic and microscopic observations, the role of cavitation bubbles in ultrasonic cleaning from our tests with varying DO supersaturation in water. From the macroscopic observation, we obtained the findings as follows. The cavitation inception threshold is reduced by having higher DO supersaturation in the water, so that the population of cavitation bubbles is increased. As the bubble population becomes denser, the bubbles' advection is found to be strengthened by the primary Bjerknes force. The liquid flow is induced by entrainment effect of the moving bubbles but is rather limited in our tests. However, we may say that the liquid streaming may possibly assist in preventing the reattachment of removed particles. It is found from the PRE result that the particle removal is achieved mainly by the action of cavitation bubbles, but there exists the optimal supersaturation to maximize the cleaning efficiency, which is determined by the trade-off relation between individual bubble dynamics and bubbly liquid steaming. Furthermore, it follows from the simple erosion tests with aluminum foils that DO supersaturation could play a role in minimizing cavitation erosion with milder bubble dynamics, which is supported by the frequency spectrum analysis of the acoustic emissions from the oscillating bubbles. From the microscopic observation of individual bubble dynamics, we confirm that cloud dynamics of split bubble fragments play a dominant role in particle removal. As a result of the tilted jet impact against the wall, the bubble-bubble interaction, which plays a more important role among more populated cavitation bubbles at the higher DO supersaturation, will result in suppression of both the generated wall shear stress (cleaning effect) and water-hammer pressure (damaging effect), supporting the dependency of PRE and erosion on the supersaturation. In conclusion, our findings suggest that low-intensity ultrasound irradiation under optimal gas supersaturation in cleaning solutions allows for having mild bubble dynamics (without violent collapse) and thus cleaning surfaces effectively with minimal cavitation erosion.

5.2 Outlook

In this thesis, we have contributed to better understand the diffusion-driven dynamics under gas supersaturation, and acoustics and fluid dynamics with underwater ultrasound and gas supersaturation. There are still many topics and questions that could be tackled in future.

For generating gas-supersaturated water, we have mainly applied oxygen gas due to the availability of the commercial DO meter. However, in more practical viewpoints, it is important to apply air for the aeration and fundamental understanding of air-supersaturated water is necessary such as solubility of nitrogen and oxygen gas and cleaning ability of the water, which will be taken up using the similar experimental set-up in this thesis. Additionally, it would be interesting to further study the neglected effect in this thesis, which includes the surface wettability and diffusion through solid surfaces. As for diffusion-driven dynamics under sonication, the rectified diffusion phenomena also could be studied to evaluate the promoted nucleation with area and shell effect [41].

In topic of acoustics and fluid dynamics with underwater ultrasound and gas supersaturation, there is a long way to pursue because of the complicated external parameters described in Section 1.1. Here, we pick up several approaches related to the acoustics and fluid dynamics influenced by mass transfer under gas supersaturation. It would be interesting to study the void fraction using capillary technique [263] or electric sensor [219] to improve the accuracy of scattered light analysis in this thesis. The void fraction measurement could estimate the degassing effect by acoustic cavitation compared with dissolved gas measurement. Acoustic shielding effect and the resulting bubbly acoustic streaming could be evaluated experimentally using additional transducer [51] and numerically using a comercial Finite Element Method (FEM) software (COMSOL) [73]. We believe that the void fraction, the acoustic shielding, and the bubbly acoustic streaming could be quantitatively correlated in future.

For a better understanding of the cleaning force on particle removal by acoustic cavitation, it is desirable to directly measure wall shear stress induced by the dynamics of ultrasonic cavitation bubbles. The wall shear stress for the case with laser-induced bubbles has been measured together with a high-speed recording and a hydrophone measurement [78]. It is also possible to extend the experiment for the case of acoustic cavitation dynamics [45,264]. In order to control acoustic cavitation in time and space, we propose here the generation of a single bubble from a gas-filled micro-pippete by a single cycle of ultrasound. The method is believed to be applied for the direct measurement of wall shear stress induced by the dynamics of acoustic cavitation bubble. In addition, although the particles attaching force is inversely proportional to their size, the smallest particles have resulted in the lowest PRE in this thesis, which might be caused by the re-attachment of particles removed once. It would be interesting to study the removal of such submicron-sized pariticles by total internal reflection fluoresence (TIRF) technique using focused CW laser [265] and electron-multiplying charge coupled device (EMCCD) camera [266,267] that can detect weak intensity of fluorescence at nanometer spatial resolution, minimizing both autofluorescence and detector noise. Following the previous study of bacteria detachment by moving air-liquid interface in microchannel [268] with additional attachment of a transducer onto the channel, we also could drive acoustic cavitation and study its cleaning force on surface-attached particles.

For a better understanding of the surface attachment force of particles, it would be interesting to devise a microchannels in which surface-attached particles are removed by laminar flow of liquid. In this study, particles are removed by wall shear stress or by moving three-phase contact line [89]. The volume flow rate and thus the liquid velocity is changed to detect the threshold wall shear stress or the threshold velocity of the contact line for particle removal. The experimental data is compared with the analytical solution of laminar flow [269] and particle removal model [270].

As for frequency dependence on ultrasonic cleaning, it is interesting to study the ultrasonic cleaning under higher frequency (100kHz–1MHz) with gas-supersaturated water in more detail. In the present study, we put a focus on the case of low-frequency ultrasound that matters in degrease cleaning. The present finding indicates that the use of dissolved gas supersaturated water is also useful in the case of higher-frequency ultrasound such as megasonic cleaning for silicon wafers. The cavitation inception threshold even for the case of megasonic waves can in principle be reduced under the supersaturation, which allows for nucleating bubbles with lower-intensity acoustic power and thus for less erosive cleaning with milder bubble dynamics. Stronger acoustic bubbly flow is expected under the higher-frequency ultrasound irradiation and may contribute to more efficient particle removal. Schlieren imaging could be feasible for such higher frequency case and compared with the acoustic pressure measurement [271]. Finally it is noted that silicon wafers have relatively rough surfaces, which is expected to include three-dimensional configurations and thus to cause the secondary Bjerkness force on the bubbles movement attracted toward the walls. As described in Section 1.2 and 4.3.3, cavitation phenomena can preferentially and continuously happen on such rough surfaces, likely to be sensitive to surface erosion.

Appendix A

Image analysis for bubble size distribution

The bubble images under aeration with the commercial microbubble generator are captured by a high-speed camera (FASTCAM SA-X2, Photron) with a microscope (×1.25, 16 μm per pixel) at the frame rate 50,000 frames per second and the shutter speed 1/3410526 s^{-1}; a typical image is presented in Fig. A.1(a). Bubble size distribution is determined by image processing with MATLAB, based on Otsu's method [220]. The histogram of the measured bubble size is shown in Fig. A.1(b). The size distribution (up to 846 μm) is normalized by the mode radius ($R_{\mathrm{mode}} = 13\,\mu\mathrm{m}$) and is then fitted to the log-normal distribution [272, 273]

$$f\,(R/R_{\mathrm{mode}}\,|\,\mu,\sigma) = \frac{R_{\mathrm{mode}}}{R\sigma\sqrt{2\pi}}\exp\left[-\frac{\{\mathrm{In}\,(R/R_{\mathrm{mode}})-\mu\}^2}{2\sigma^2}\right], \tag{A.1}$$

where the most probable radius is given by $R = R_{\mathrm{mode}}e^{\mu}$ and σ is the standard deviation. It follows from Fig. A.1(b) that the distribution has its most probable radius at 59 μm and its standard deviation at 1.0. It is confirmed that the fitted values (μ and σ) are fairly repeatable with different bubble images.

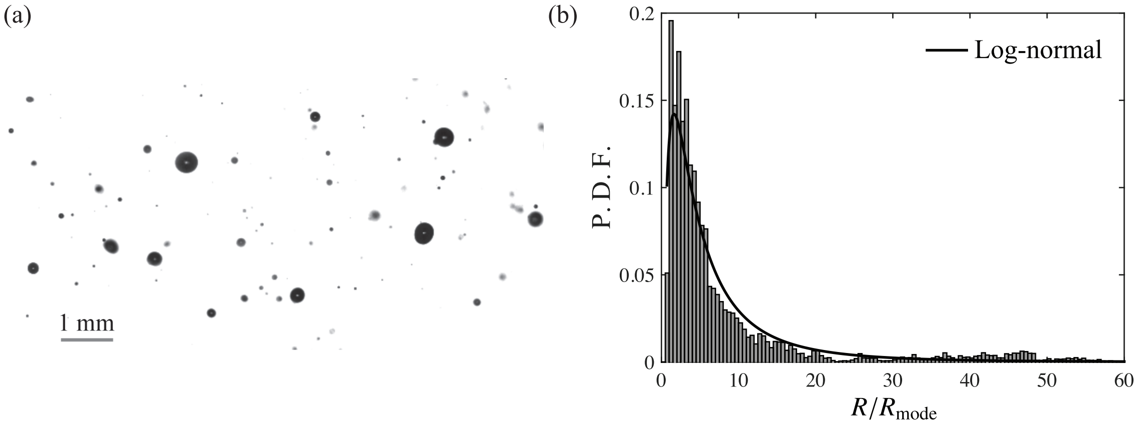

Fig A.1: (a) Typical image of the bubbles obtained from the commercial microbubble generator. (b) Bubble size distribution detected from (a). The detected distribution is fitted to the log-normal probability density function (P.D.F.). The mode radius in (a) is $R_{\mathrm{mode}} = 13\,\mu\mathrm{m}$.

Appendix B

Maximum supersaturation

We discuss the effect of bubble size on the maximum DO supersaturation, $\max(\zeta_1)$. The microbubble aeration results in $\max(\zeta_1) \approx 6.0$, while we obtained $\max(\zeta_1) \approx 2.7$ with the millibubbles aeration (see Fig. B.1). It is of interest that we do not observe strong bubble formation at the container surfaces even under such a supersaturation state. Namely, the oxygen supersaturation is metastable against bubble nucleation at solid boundaries. One possible reason to explain the metastable supersaturation is the existence of nanobubbles that are closely populated in the bulk of the aerated water. In other words, Laplace pressure effects at bubble interfaces can be manifested as gas supersaturation uniformly in the bulk phase [274]. From Young–Laplace equation and Henry's law that are considered to hold even at nanometer scales [156,275], the critical radius of a gas bubble that is stable under supersaturation ζ can be computed by [276]

$$R_{\mathrm{cr}} = \frac{2\gamma}{p_\infty \zeta} \,. \tag{B.1}$$

It follows from Eq. (B.1) that bubbles that are stable under supersaturation ζ needs to be singe-sized at R_{cr}. According to Eq. (B.1), the critical radius of bubbles that are stable under the supersaturation $\zeta_{\max} = 5.0$ is calculated by $R_{\mathrm{cr}} = 243$ nm. Hence, there may in principle exist nanobubbles in the water aerated with microbubbles. Additionally, bulk nanobubble can achieve a diffusion-equilibrium when the bubble is partially covered with hydrophobic material which significantly hinders gas flux [157]. The stable bubble radius R_{eq} is plotted in Fig. B.2 as functions of gas supersaturation ζ and fraction of hydrophobic coverage. This model (so-called dynamic equilibrium model) suggests that the bulk

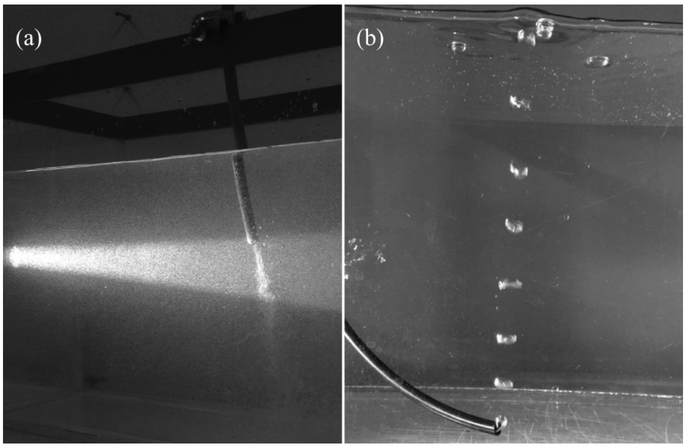

Fig B.1: Images of the aeration with (a) microbubbles produced by the commercial microbubble generator and (b) millibubbles. In either case, oxygen gas is ejected from a polyurethane tube whose inner and outer diameters are 7 mm and 4 mm, respectively.

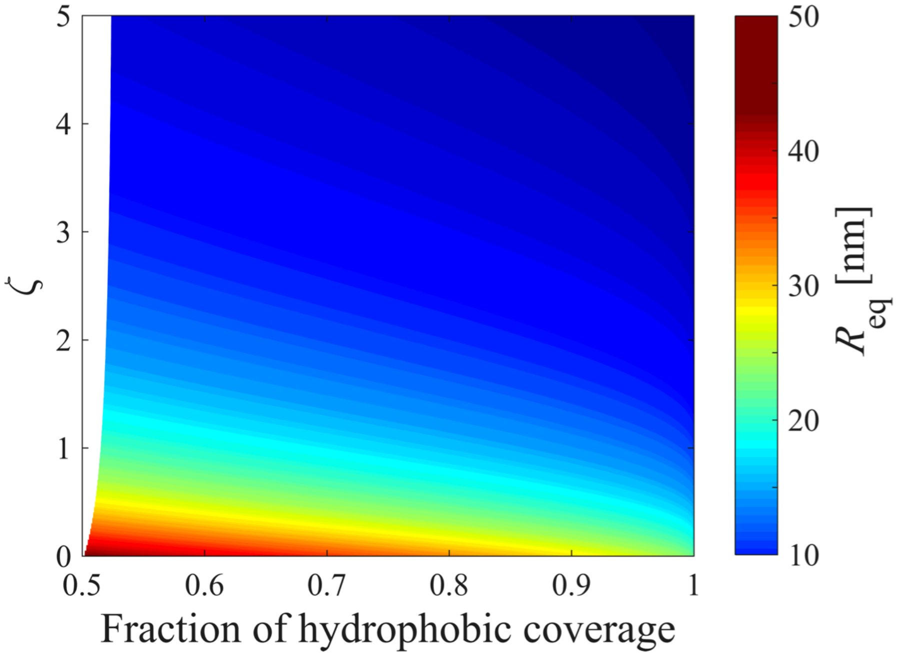

Fig B.2: Bubble radius under dynamic equilibrium as a function of the fraction of hydrophobic coverage and gas supersaturation ζ.

nanobubble can be thermodynamically stable whose size decreases as gas supersaturation or fraction of hydrophobic coverage increase.

Appendix C

Threshold diameter of the seeding particles

According to [242], we can estimate the threshold diameter for the seeding particles below which the drag force becomes dominant over the acoustic radiation force:

$$D_{p,\text{thresh}} = 2\sqrt{\frac{9\mu_l U\lambda}{\kappa_l\,(1-\kappa_l/\kappa_p)p^2}} \approx 2.8\,\text{mm}, \tag{C.1}$$

where $\mu_l = 1.0\times10^{-3}$ Pa·s is the water viscosity, $U = 10$ mm/s is the characteristic velocity of water, $\lambda = 53$ mm is the wavelength of the 28-kHz ultrasound, $\kappa_l = 0.45$ (GPa)$^{-1}$ and $\kappa_p = 0.21$ (GPa)$^{-1}$ is the compressibility of water and the particles, respectively, and $p = 0.1$ MPa is the characteristic acoustic intensity. The particles' diameter in the present study (4 μm) is confirmed to be much smaller than the threshold diameter, suggesting that our seeding particles are good PIV particles to extract liquid-phase velocity. It is noted that since some physical parameters (sound of speed and shear modulus) of the seeding particles (Melamine) are not available, we adopt those of acryl as a similar material to estimate the threshold diameter.

Appendix D

Evolution of the cavitation structure and surface erosion

In Fig. D.1 and D.2, we show supplemental materials for the transient evolution of the cavitation activity with and without inserting the cleaning sample, respectively, under different ζ. The bubbly structure of acoustic cavitation in the water is highlighted using imageJ and the $z-$distribution of normalized intensity of scattered light from bubbles is plotted in Fig. D.3 and D.4. The transducer's surface and air-water interface have a bright intensity due to the surface-attached bubbles and floating bubbles, respectively. In Fig. D.3(b), we can clearly see that, as ζ increases, there appears a larger number of (visible-sized) cavitation bubbles on the cleaning surfaces, whose center is located at $z/\lambda = 0.5$. This supports the higher cleaning efficiency at higher ζ, enhanced by the translation of acoustic cavitation bubble under attraction to the cleaning surfaces by the secondary Bjerknes force. Thus we can say that, in our cleaning tests, there is no need to move the cleaning samples in the tank because the cavitation bubble preferentially translates toward the surface and uniform cleaning is expected by the enlarged area of active cavitation.

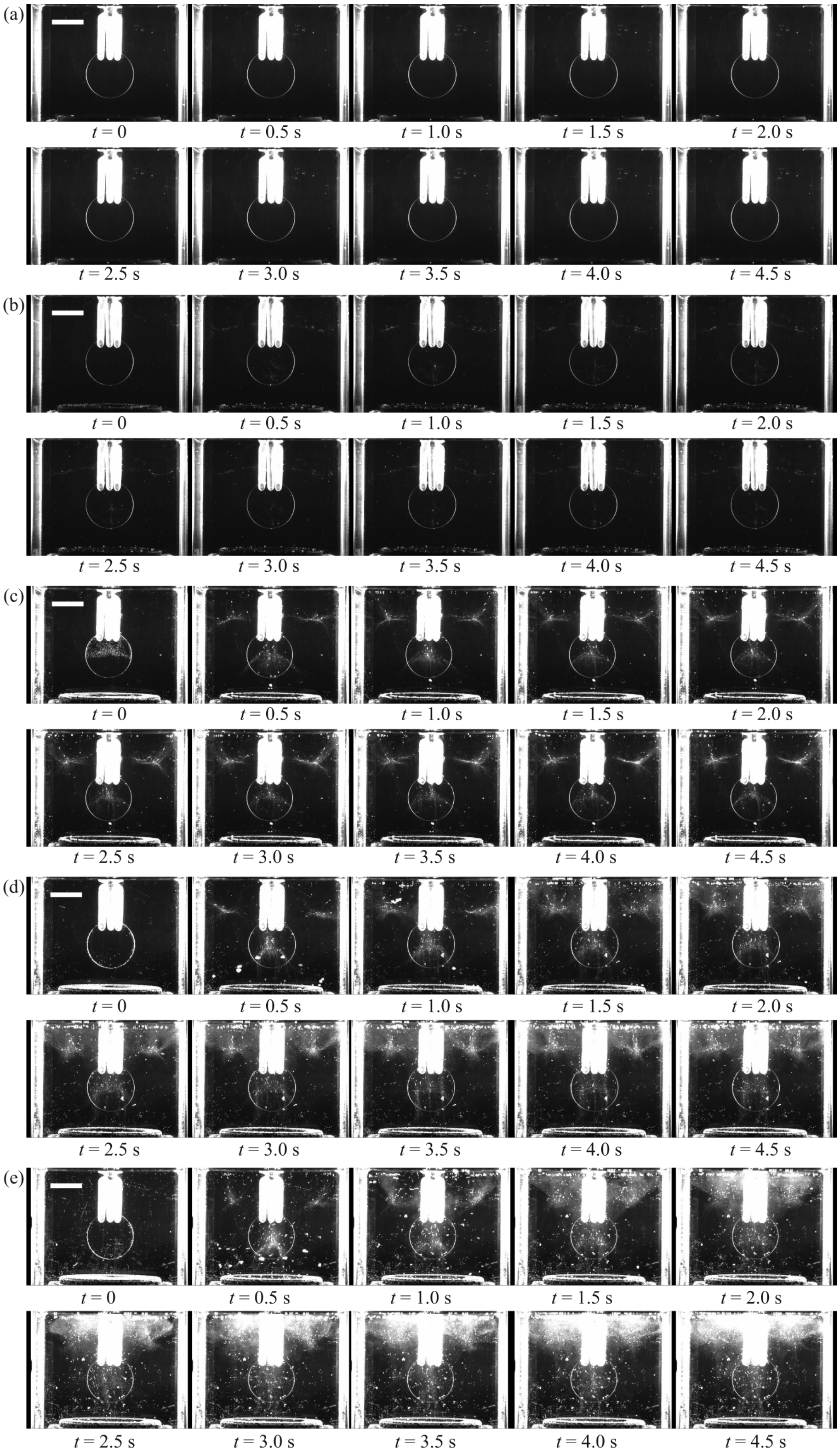

Fig D.1: Evolution of the cavitation structure with the cleaning sample in the water with different DO supersaturation (a) $\zeta = 0.0$, (b) $\zeta = 1.0$, (c) $\zeta = 2.0$, (d) $\zeta = 3.0$, and (d) $\zeta = 4.0$. Each scale bar shows 20 mm.

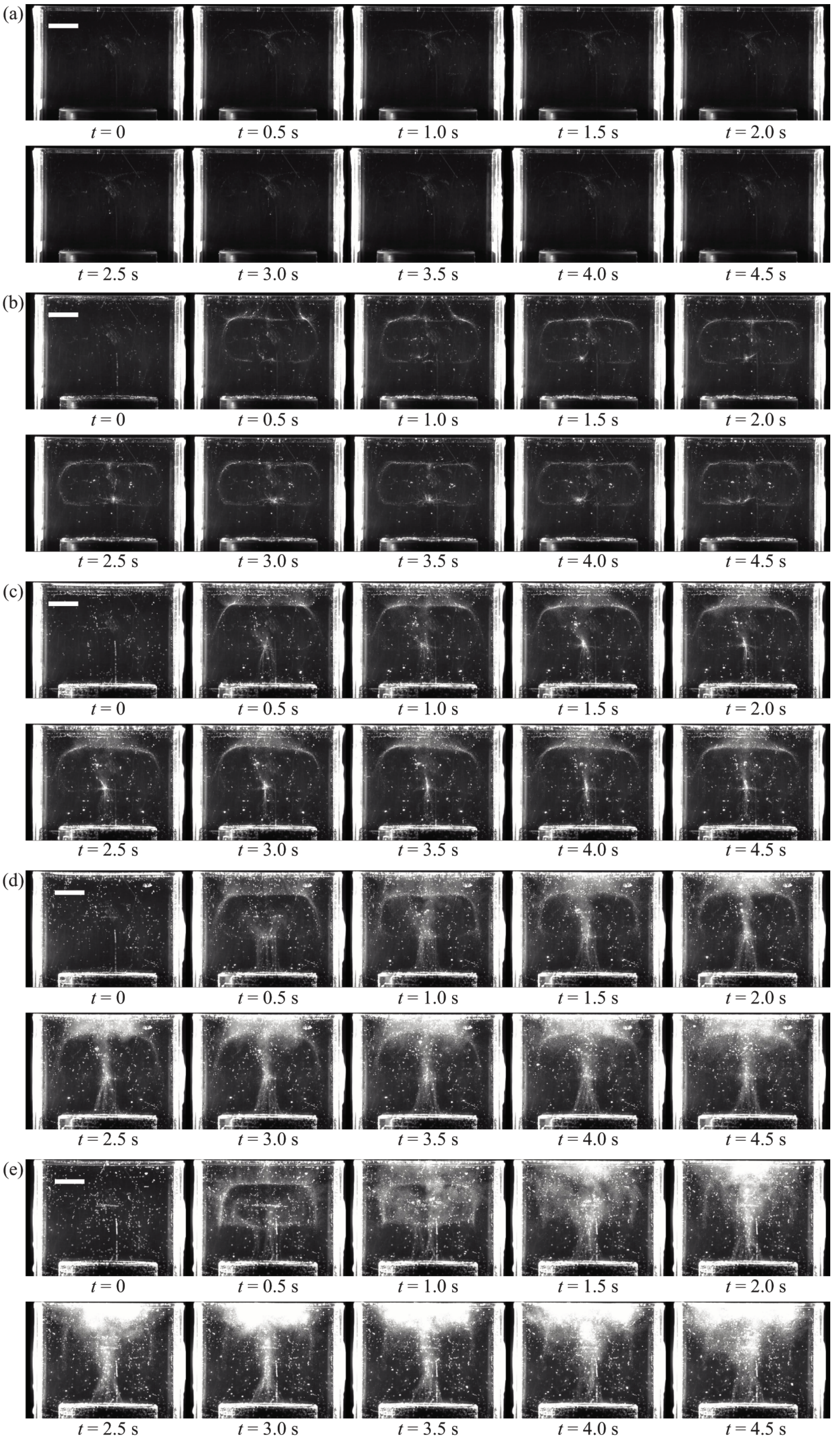

Fig D.2: As Fig. D.1, but without inserting the cleaning sample. Each scale bar shows 20 mm.

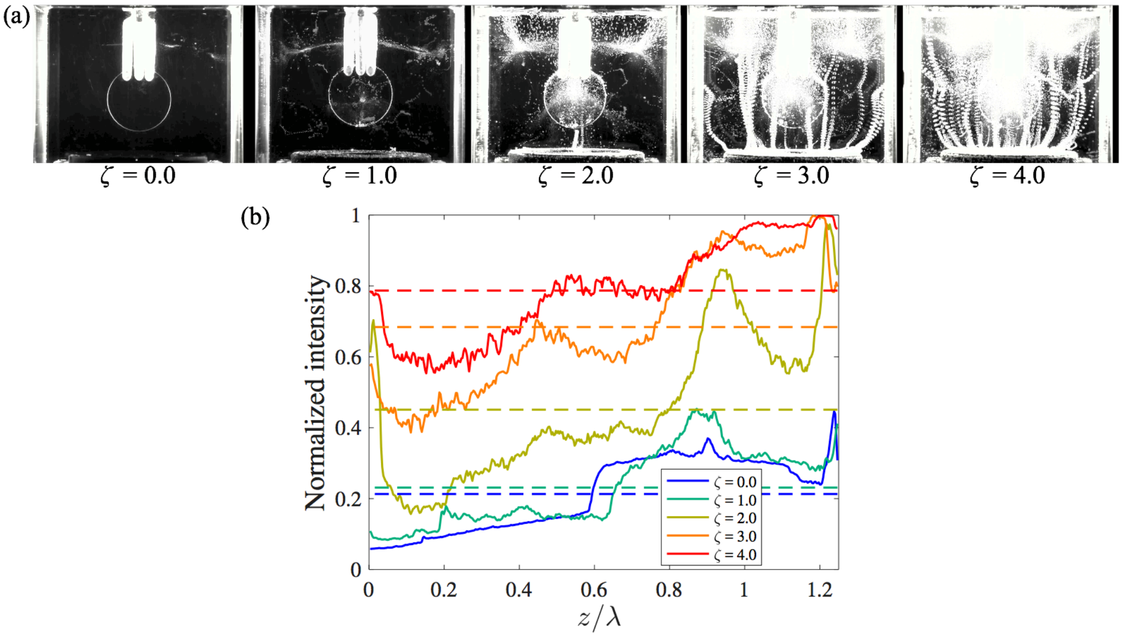

Fig D.3: (a) As Fig. 4.8, but the snapshots (without inserting the cleaning sample) are post-processed with imageJ to highlight the bubbly structure of acoustic cavitation in the water at different ζ. (b) Intensity profile of the scattered light from the cavitation bubbles, which are obtained from (a).

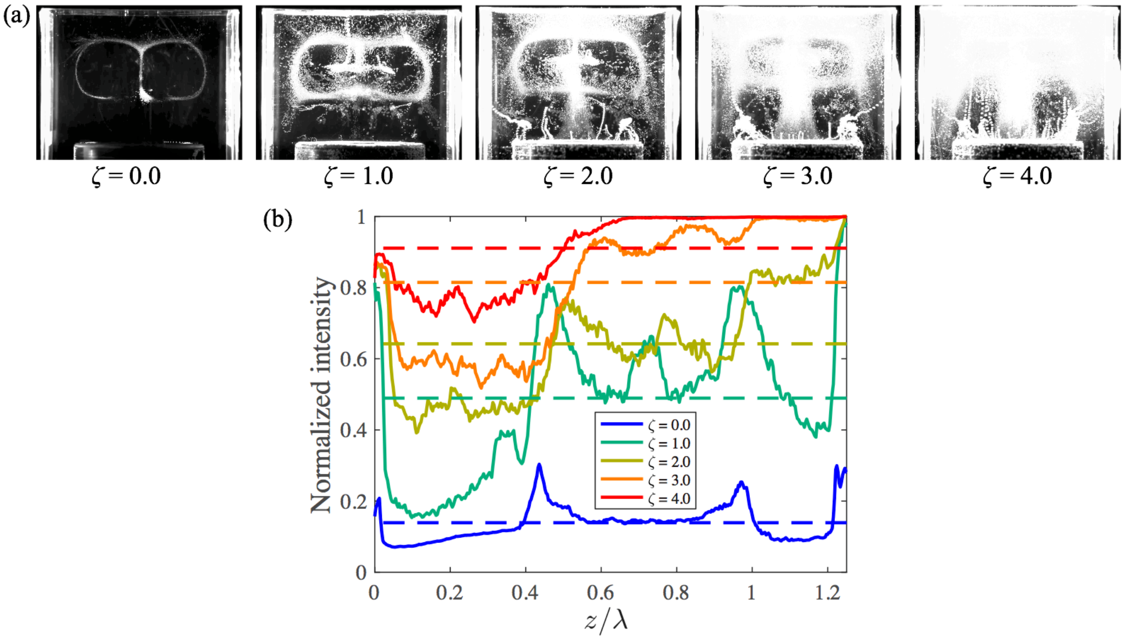

Fig D.4: (a) As Fig. D.3, but without inserting the cleaning sample.

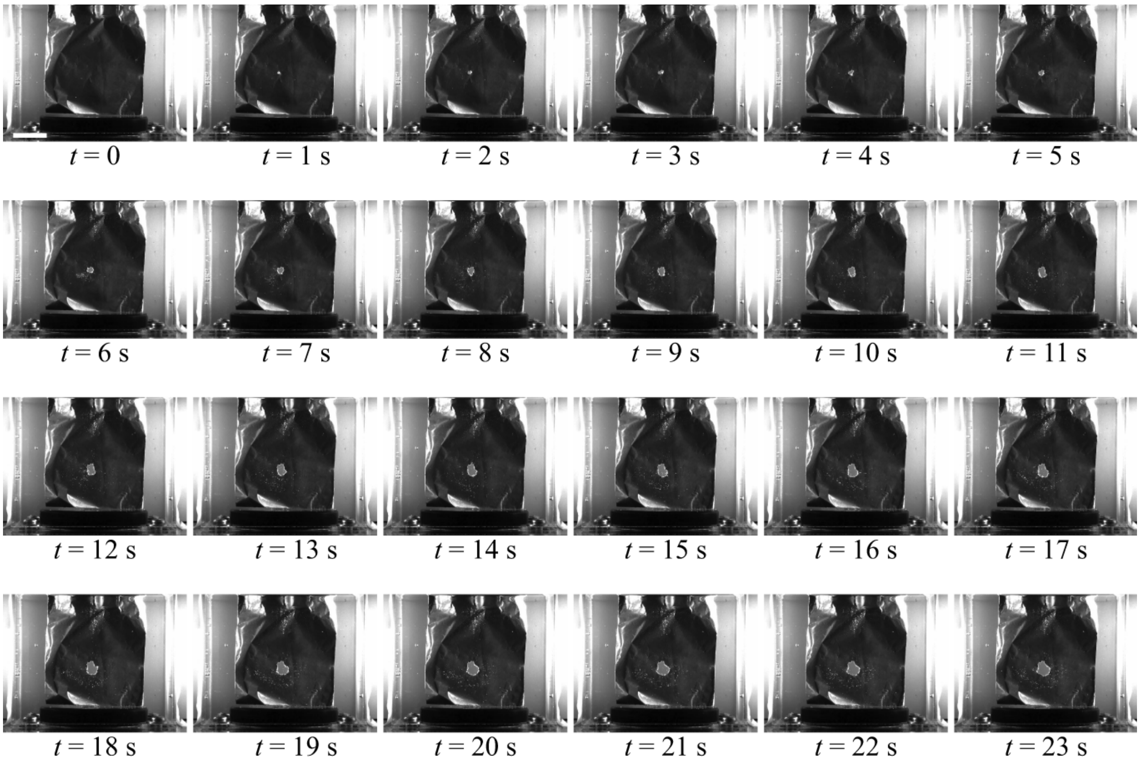

$t = 0$ $t = 1$ s $t = 2$ s $t = 3$ s $t = 4$ s $t = 5$ s

$t = 6$ s $t = 7$ s $t = 8$ s $t = 9$ s $t = 10$ s $t = 11$ s

$t = 12$ s $t = 13$ s $t = 14$ s $t = 15$ s $t = 16$ s $t = 17$ s

$t = 18$ s $t = 19$ s $t = 20$ s $t = 21$ s $t = 22$ s $t = 23$ s

Fig D.5: Cavitation erosion on an aluminum foil during the sonication under DO supersaturation $\zeta = 0.0$.

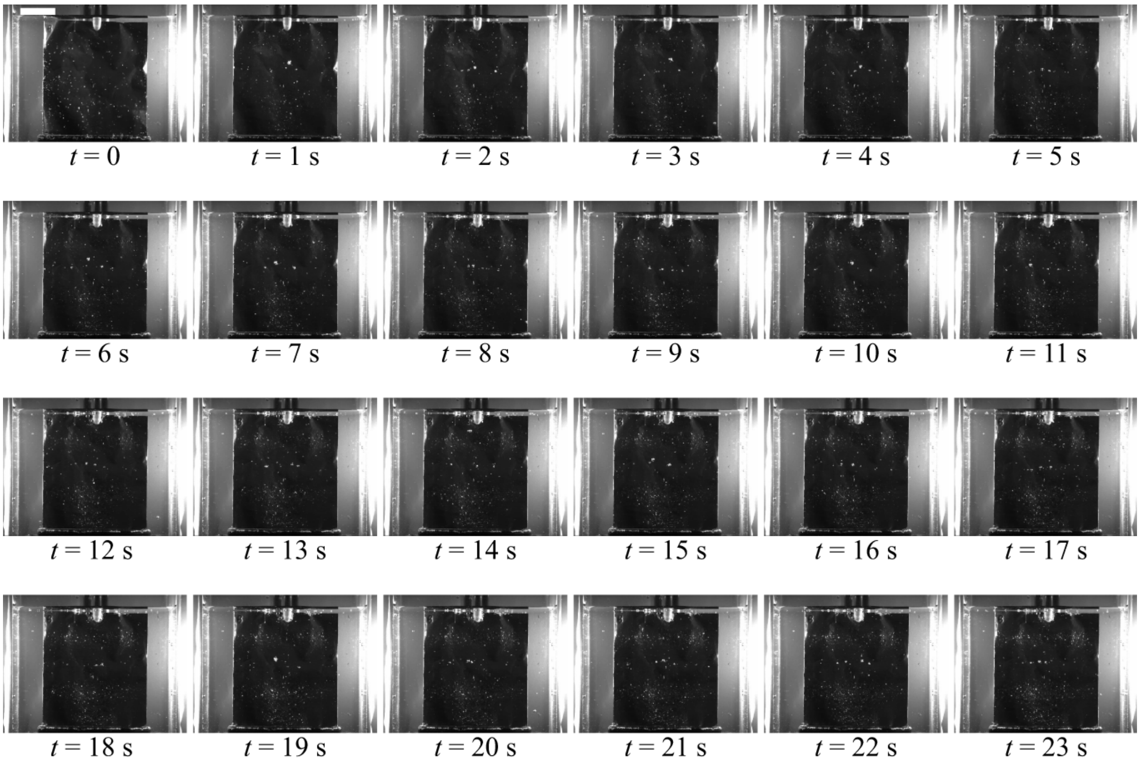

$t = 0$ $t = 1$ s $t = 2$ s $t = 3$ s $t = 4$ s $t = 5$ s

$t = 6$ s $t = 7$ s $t = 8$ s $t = 9$ s $t = 10$ s $t = 11$ s

$t = 12$ s $t = 13$ s $t = 14$ s $t = 15$ s $t = 16$ s $t = 17$ s

$t = 18$ s $t = 19$ s $t = 20$ s $t = 21$ s $t = 22$ s $t = 23$ s

Fig D.6: Cavitation erosion on an aluminum foil during the sonication under DO supersaturation $\zeta = 1.0$.

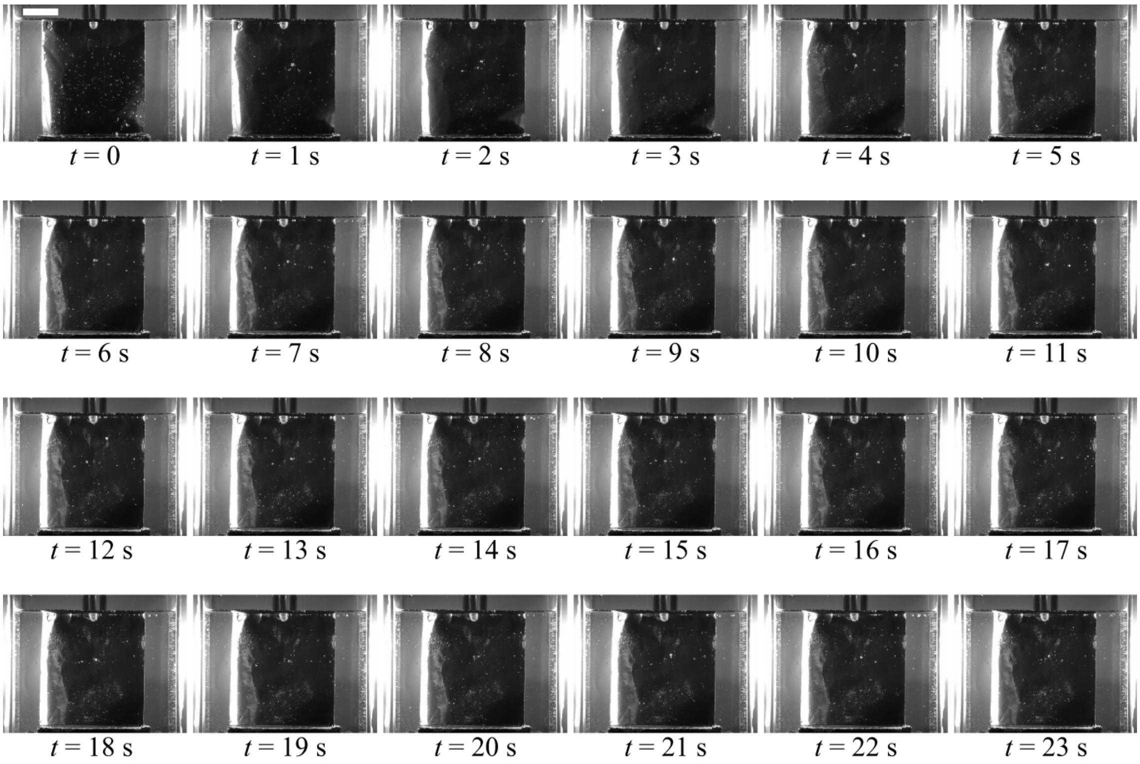

$t = 0$ $t = 1$ s $t = 2$ s $t = 3$ s $t = 4$ s $t = 5$ s

$t = 6$ s $t = 7$ s $t = 8$ s $t = 9$ s $t = 10$ s $t = 11$ s

$t = 12$ s $t = 13$ s $t = 14$ s $t = 15$ s $t = 16$ s $t = 17$ s

$t = 18$ s $t = 19$ s $t = 20$ s $t = 21$ s $t = 22$ s $t = 23$ s

Fig D.7: Cavitation erosion on an aluminum foil during the sonication under DO supersaturation $\zeta = 2.0$.

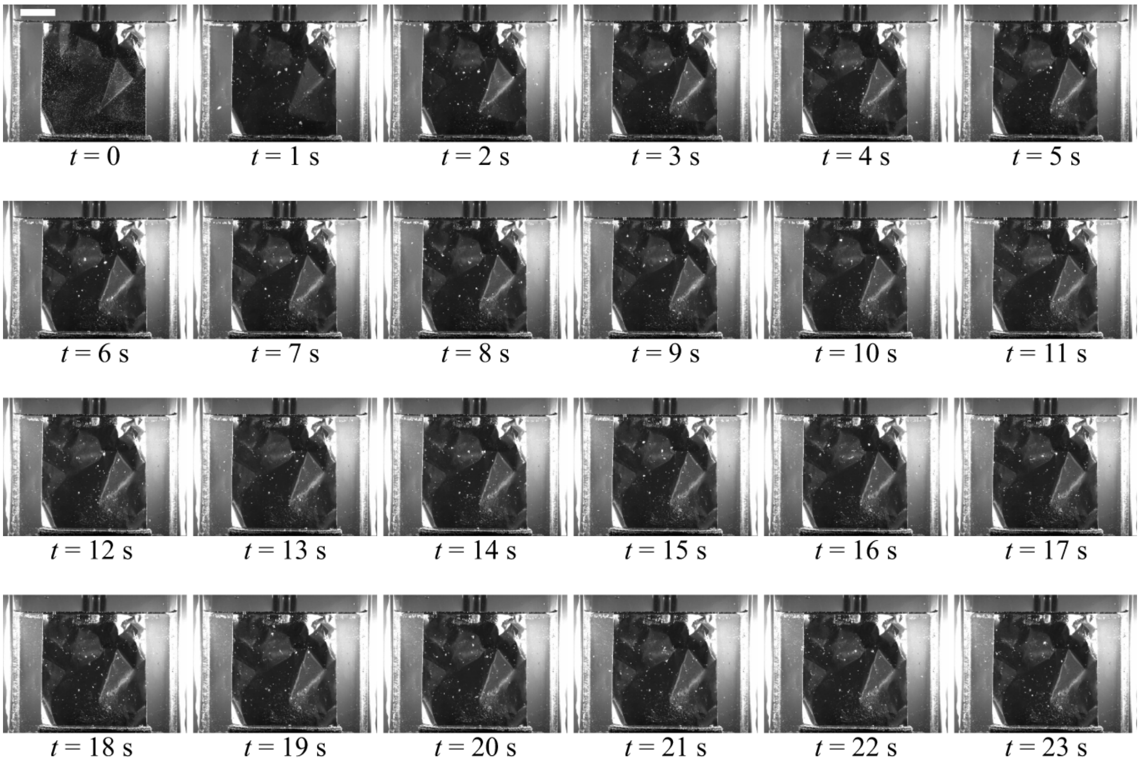

$t = 0$ $t = 1$ s $t = 2$ s $t = 3$ s $t = 4$ s $t = 5$ s

$t = 6$ s $t = 7$ s $t = 8$ s $t = 9$ s $t = 10$ s $t = 11$ s

$t = 12$ s $t = 13$ s $t = 14$ s $t = 15$ s $t = 16$ s $t = 17$ s

$t = 18$ s $t = 19$ s $t = 20$ s $t = 21$ s $t = 22$ s $t = 23$ s

Fig D.8: Cavitation erosion on an aluminum foil during the sonication under DO supersaturation $\zeta = 3.0$.

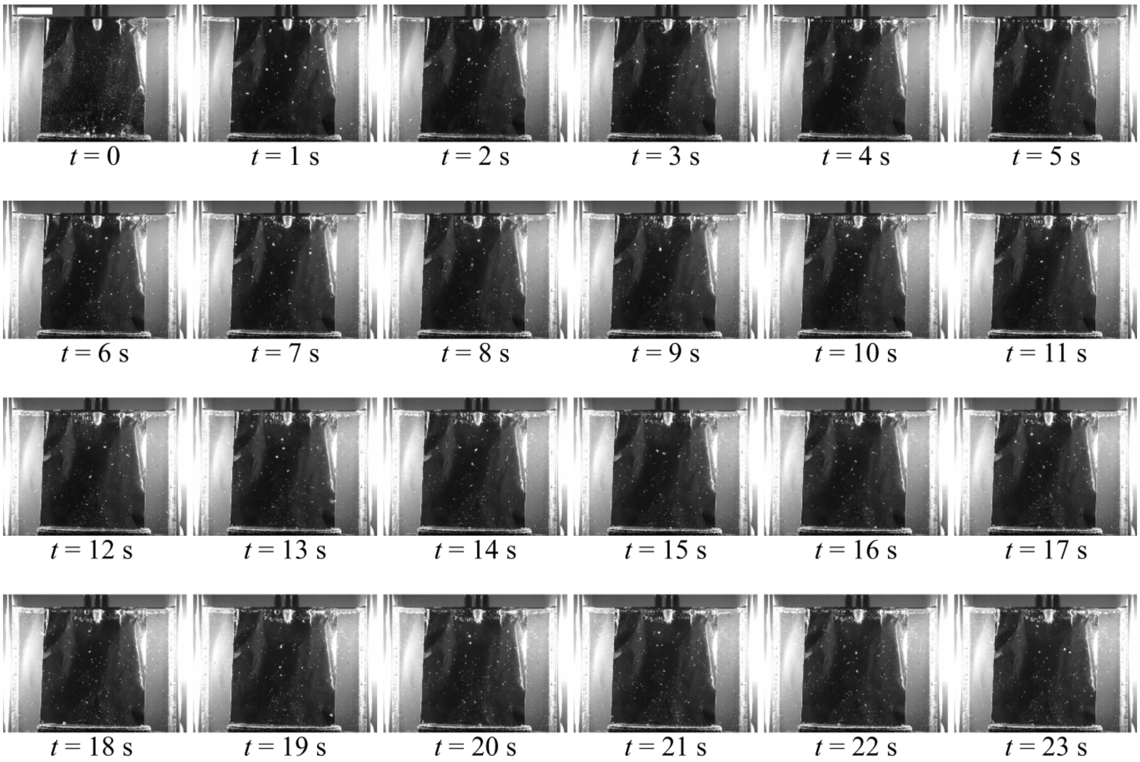

$t = 0$ $t = 1$ s $t = 2$ s $t = 3$ s $t = 4$ s $t = 5$ s

$t = 6$ s $t = 7$ s $t = 8$ s $t = 9$ s $t = 10$ s $t = 11$ s

$t = 12$ s $t = 13$ s $t = 14$ s $t = 15$ s $t = 16$ s $t = 17$ s

$t = 18$ s $t = 19$ s $t = 20$ s $t = 21$ s $t = 22$ s $t = 23$ s

Fig D.9: Cavitation erosion on an aluminum foil during the sonication under DO supersaturation $\zeta = 4.0$.

In Fig. D.5 to D.9, we show supplemental materials for the transient evolution of the cavitation activity on aluminum surfaces under different ζ. There appears a larger number of (visible-sized) cavitation bubbles on the aluminum surfaces as ζ increases. However, as mentioned in Section 4.3.3, a large hole does not created except for the case of the saturated water ($\zeta = 0.0$), which is caused by the milder bubble dynamics under higher DO supersaturation. A number of micropits seem to be created by sub-resonant bubble near the second pressure antinode at $(x, z) = (0, \lambda)$. Although the super-resonant bubbles are observed around the first pressure node at $(x, z) = (0, \lambda)$, there seems to negligible erosion by their dynamics, suggesting their milder dynamics. For the case of higher DO supersaturation ($\zeta = 3.0$ and 4.0), bubbles appear preferentially near the transducer's surface at ($z = 0$), which is the main cause for a larger number of micropits. Near the transducer's surface, attenuation of ultrasonic energy is still weak, so that the cavitation becomes more intense than the location at higher z.

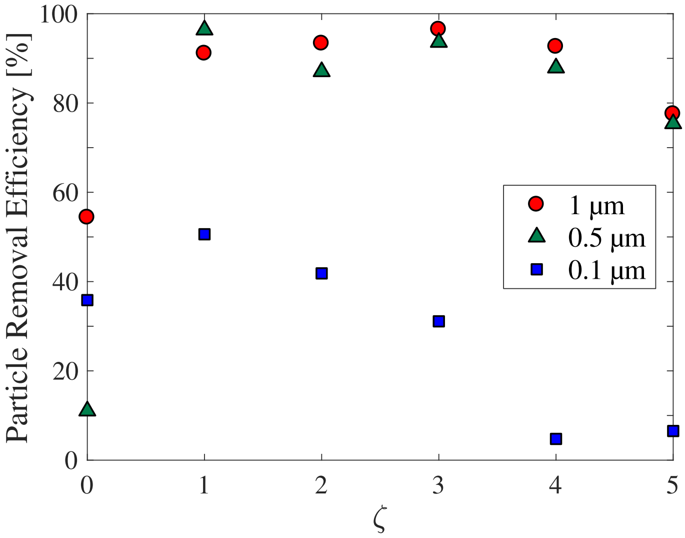

Fig D.10: PRE from the ultrasonic cleaning tests ($p_{\mathrm{rms}}(z = \lambda/2) = 1.4$ atm) as a function of DO supersaturation ζ.

Appendix E

PRE under higher ultrasound intensity

Figure D.10 shows the supplementary results of the PRE after a higher-intensity sonication at $p_{\mathrm{rms}}(z = \lambda/2) = 1.4$ atm. For the cases of 0.5 and 1 μm particles, PRE reaches up to mostly 100%. For all the particles, PRE decreases as increasing the supersaturation above $\zeta \approx 1.0$, which has the optimal supersaturation to maximum PRE. This also supports the trade-off between individual bubble dynamics and bubbly streaming as discussed in Section 4.3.3. However, higher input voltage will give rise thermal damage of the transducer. To stress that our results are for the case of low-intensity ultrasound only, we put the adjective ”low-intensity” in the main section.

References

[1] A. Manbachi and R. S. C. Cobbold, "Development and application of piezoelectric materials for ultrasound generation and detection," *Ultrasound*, vol. 19, no. 4, pp. 187–196, 2011.

[2] A. Shoh, "Industrial applications of ultrasound - A review I. High-Power Ultrasound," *IEEE Trans. Sonics Ultrason.*, vol. 22, no. 2, pp. 60–71, 1975.

[3] H. M. Kyllönen, P. Pirkonen, and M. Nyström, "Membrane filtration enhanced by ultrasound: A review," *Desalination*, vol. 181, pp. 319–335, 2005.

[4] B. Avvaru, N. Venkateswaran, P. Uppara, S. B. Iyengar, and S. S. Katti, "Current knowledge and potential applications of cavitation technologies for the petroleum industry," *Ultrason. Sonochem.*, vol. 42, pp. 493–507, 2018.

[5] X. Luo, J. Cao, H. Gong, H. Yan, and L. He, "Phase separation technology based on ultrasonic standing waves: A review," *Ultrason. Sonochem.*, vol. 48, pp. 287–298, 2018.

[6] F. Chemat, Zill-E-Huma, and M. K. Khan, "Applications of ultrasound in food technology: Processing, preservation and extraction," *Ultrason. Sonochem.*, vol. 18, no. 4, pp. 813–835, 2011.

[7] D. Pingret, A. S. Fabiano-Tixier, and F. Chemat, "Degradation during application of ultrasound in food processing: A review," *Food Control*, vol. 31, no. 2, pp. 593–606, 2013.

[8] M. Ashokkumar, “Applications of ultrasound in food and bioprocessing,” *Ultrason. Sonochem.*, vol. 25, no. 1, pp. 17–23, 2015.

[9] I. Majid, G. A. Nayik, and V. Nanda, “Ultrasonication and food technology: A review,” *Cogent Food Agric.*, vol. 1, no. 1, pp. 1–11, 2015.

[10] K. S. Ojha, T. J. Mason, C. P. O’Donnell, J. P. Kerry, and B. K. Tiwari, “Ultrasound technology for food fermentation applications,” *Ultrason. Sonochem.*, vol. 34, pp. 410–417, 2017.

[11] L. Paniwnyk, “Applications of ultrasound in processing of liquid foods: A review,” *Ultrason. Sonochem.*, vol. 38, pp. 794–806, 2017.

[12] K. S. Suslick, S.-B. Choe, A. A. Cichowlas, and M. W. Grinstaff, “Sonochemical synthesis of amorphous iron,” *Nature*, vol. 353, no. 6343, pp. 414–416, 1991.

[13] A. Kotronarou, G. Mills, and M. R. Hoffmann, “Decomposition of parathion in aqueous solution by ultrasonic irradiation,” *Environ. Sci. Technol.*, vol. 26, no. 7, pp. 1460–1462, 1992.

[14] P. R. Gogate, “Cavitational reactors for process intensification of chemical processing applications: A critical review,” *Chem. Eng. Process. Process Intensif.*, vol. 47, no. 4, pp. 515–527, 2008.

[15] T. Leong, L. Johansson, P. Juliano, S. L. McArthur, and R. Manasseh, “Ultrasonic separation of particulate fluids in small and large scale systems: A review,” *Ind. Eng. Chem. Res.*, vol. 52, no. 47, pp. 16555–16576, 2013.

[16] S. V. Sancheti and P. R. Gogate, “A review of engineering aspects of intensification of chemical synthesis using ultrasound,” *Ultrason. Sonochem.*, vol. 36, pp. 527–543, 2017.

[17] S. Koch, P. Pohl, U. Cobet, and N. G. Rainov, "Ultrasound enhancement of liposome-mediated cell transfection is caused by cavitation effects," *Ultrasound Med. Biol.*, vol. 26, no. 5, pp. 897–903, 2000.

[18] G. Ter Haar, "Therapeutic applications of ultrasound," *Prog. Biophys. Mol. Biol.*, vol. 93, pp. 111–129, 2007.

[19] R. Karshafian, P. D. Bevan, R. Williams, S. Samac, and P. N. Burns, "Sonoporation by ultrasound-activated microbubble contrast agents: Effect of acoustic exposure parameters on cell membrane permeability and cell viability," *Ultrasound Med. Biol.*, vol. 35, no. 5, pp. 847–860, 2009.

[20] L. Serpe and F. Giuntini, "Sonodynamic antimicrobial chemotherapy: First steps towards a sound approach for microbe inactivation," *J. Photochem. Photobiol. B Biol.*, vol. 150, pp. 44–49, 2015.

[21] X. Guo, C. Cai, G. Xu, Y. Yang, J. Tu, P. T. Huang, and D. Zhang, "Interaction between cavitation microbubble and cell: A simulation of sonoporation using boundary element method (BEM)," *Ultrason. Sonochem.*, vol. 39, pp. 863–871, 2017.

[22] W. J. Tyler, S. W. Lani, and G. M. Hwang, "Ultrasonic modulation of neural circuit activity," *Curr. Opin. Neurobiol.*, vol. 50, pp. 222–231, 2018.

[23] A. E. Crawford, "A practical introduction to ultrasonic cleaning," *Ultrasonics*, vol. 1, no. 2, pp. 65–69, 1963.

[24] T. J. Mason, "Ultrasonic cleaning: A historical perspective," *Ultrason. Sonochem.*, vol. 29, pp. 519–523, 2016.

[25] G. W. Gale and A. A. Busnaina, "Removal of particulate contaminants using ultrasonics and megasonics: A review," *Part. Sci. Technol.*, vol. 13, no. 3-4, pp. 197–211, 1995.

[26] R. Kohli and K. L. Mittal, *Developments in Surface Contamination and Cleaning*. William Andrew, 2011.

[27] W. J. Colclough, “The chemistry of solvents used for ultrasonic cleaning,” *Ultrasonics*, vol. 6, no. 1, pp. 21–23, 1968.

[28] P. Cintas and J.-L. Luche, “Green chemistry: The sonochemical approach,” *Green Chem.*, vol. 1, no. 3, pp. 115–125, 1999.

[29] M. O. Lamminen, H. W. Walker, and L. K. Weavers, “Mechanisms and factors influencing the ultrasonic cleaning of particle-fouled ceramic membranes,” *J. Memb. Sci.*, vol. 237, no. 1-2, pp. 213–223, 2004.

[30] Y. Tanimura, K. Yoshida, and Y. Watanabe, “A study on cleaning ability of oscillating bubbles driven by low-frequency ultrasound,” *Jpn. J. Appl. Phys.*, vol. 49, no. 7 PART 2, p. 07HE20, 2010.

[31] C. Otto, S. Zahn, F. Rost, P. Zahn, D. Jaros, and H. Rohm, “Physical methods for cleaning and disinfection of surfaces,” *Food Eng. Rev.*, vol. 3, no. 3-4, pp. 171–188, 2011.

[32] G. L. Chahine, A. Kapahi, J.-K. Choi, and C.-T. Hsiao, “Modeling of surface cleaning by cavitation bubble dynamics and collapse,” *Ultrason. Sonochem.*, vol. 29, pp. 528–549, 2016.

[33] F. Reuter and R. Mettin, “Mechanisms of single bubble cleaning,” *Ultrason. Sonochem.*, vol. 29, pp. 550–562, mar 2016.

[34] N. S. M. Yusof, B. Babgi, Y. Alghamdi, M. Aksu, J. Madhavan, and M. Ashokkumar, “Physical and chemical effects of acoustic cavitation in selected ultrasonic cleaning applications,” *Ultrason. Sonochem.*, vol. 29, pp. 568–576, 2016.

[35] K. Ando, A. Q. Liu, and C.-D. Ohl, “Homogeneous nucleation in water in microfluidic channels,” *Phys. Rev. Lett.*, vol. 109, no. 4, pp. 1–5, 2012.

[36] G. Menzl, M. A. Gonzalez, P. Geiger, F. Caupin, J. L. F. Abascal, C. Valeriani, and C. Dellago, “Molecular mechanism for cavitation in water under tension,” *Proc. Natl. Acad. Sci.*, vol. 113, no. 48, pp. 13582–13587, 2016.

[37] L. A. Crum, “Measurements of the growth of air bubbles by rectified diffusion,” *J. Acoust. Soc. Am.*, vol. 68, no. 1, pp. 203–211, 1980.

[38] L. A. Crum and G. M. Hansen, “Generalized equations for rectified diffusion,” *J. Acoust. Soc. Am.*, vol. 72, no. 5, pp. 1586–1592, 1982.

[39] M. M. Fyrillas and A. J. Szeri, “Dissolution or growth of soluble spherical oscillating bubbles: The effect of surfactants,” *J. Fluid Mech.*, vol. 289, pp. 295–314, 1995.

[40] L. A. Crum and Y. Mao, “Acoustically enhanced bubble growth at low frequencies and its implications for human diver and marine mammal safety,” *J. Acoust. Soc. Am.*, vol. 99, no. 5, pp. 2898–2907, 1996.

[41] O. Louisnard and F. Gomez, “Growth by rectified diffusion of strongly acoustically forced gas bubbles in nearly saturated liquids,” *Phys. Rev. E*, vol. 67, no. 3, p. 036610, 2003.

[42] M. Devaud, T. Hocquet, J.-C. Bacri, and V. Leroy, “The Minnaert bubble: An acoustic approach,” *Eur. J. Phys.*, vol. 29, no. 6, pp. 1263–1285, 2008.

[43] M. A. Ainslie and T. G. Leighton, “Review of scattering and extinction cross-sections, damping factors, and resonance frequencies of a spherical gas bubble,” *J. Acoust. Soc. Am.*, vol. 130, no. 5, pp. 3184–3208, 2011.

[44] N. Bremond, M. Arora, C.-D. Ohl, and D. Lohse, “Controlled multibubble surface cavitation,” *Phys. Rev. Lett.*, vol. 96, no. 22, p. 224501, 2006.

[45] I. van der Kroon, P. A. Quinto-Su, F. Li, and C.-D. Ohl, “Acoustically driven cavitation cluster collapse in planar geometry,” *Phys. Rev. E*, vol. 82, no. 6, p. 066311, 2010.

[46] A. Tiwari, C. Pantano, and J. B. Freund, “Growth-and-collapse dynamics of small bubble clusters near a wall,” *J. Fluid Mech.*, vol. 775, pp. 1–23, 2015.

[47] N. Ochiai and J. Ishimoto, “Numerical investigation of multiple-bubble behaviour and induced pressure in a megasonic field,” *J. Fluid Mech.*, vol. 818, no. May, pp. 562–594, 2017.

[48] U. Rasthofer, F. Wermelinger, P. Hadijdoukas, and P. Koumoutsakos, “Large scale simulation of cloud cavitation collapse,” *Proc. Comput. Sci.*, vol. 108, pp. 1763–1772, 2017.

[49] J. Ma, C.-T. Hsiao, and G. L. Chahine, “Numerical study of acoustically driven bubble cloud dynamics near a rigid wall,” *Ultrason. Sonochem.*, vol. 40, pp. 944–954, 2018.

[50] T. G. Leighton, A. J. Walton, and M. J. W. Pickworth, “Primary Bjerknes forces,” *Eur. J. Phys.*, vol. 11, no. 1, pp. 47–50, 2000.

[51] J. Lee, M. Ashokkumar, K. Yasui, T. Tuziuti, T. Kozuka, A. Towata, and Y. Iida, “Development and optimization of acoustic bubble structures at high frequencies,” *Ultrason. Sonochem.*, vol. 18, no. 1, pp. 92–98, 2011.

[52] Y. Lu, J. Katz, and A. Prosperetti, “Dynamics of cavitation clouds within a high-intensity focused ultrasonic beam,” *Phys. Fluids*, vol. 25, no. 7, pp. 1–17, 2013.

[53] L. A. Crum, “Bjerknes forces on bubbles in a stationary sound field,” *J. Acoust. Soc. Am.*, vol. 57, no. 6, pp. 1363–1370, 1975.

[54] R. Mettin, I. Akhatov, U. Parlitz, C. Ohl, and W. Lauterborn, “Bjerknes forces between small cavitation bubbles in a strong acoustic field,” *Phys. Rev. E*, vol. 56, no. 3, pp. 2924–2931, 1997.

[55] J. Jiao, Y. He, K. Yasui, S. E. Kentish, M. Ashokkumar, R. Manasseh, and J. Lee, “Influence of acoustic pressure and bubble sizes on the coalescence of two contacting bubbles in an acoustic field,” *Ultrason. Sonochem.*, vol. 22, pp. 70–77, 2015.

[56] C. Lazarus, A. N. Pouliopoulos, M. Tinguely, V. Garbin, and J. J. Choi, “Clustering dynamics of microbubbles exposed to low-pressure 1-MHz ultrasound,” *J. Acoust. Soc. Am.*, vol. 142, no. 5, pp. 3135–3146, 2017.

[57] C. E. Brennen, “Fission of collapsing cavitation bubbles,” *J. Fluid Mech.*, vol. 472, pp. 153–166, 2002.

[58] W. Lauterborn and R. Mettin, “Acoustic cavitation,” in *Power Ultrason.*, pp. 37–78, Elsevier, 2015.

[59] S. Nomura and M. Nakagawa, “Analysis of an ultrasonic field attenuated by oscillating cavitation bubbles,” *Acoust. Sci. Technol.*, vol. 22, pp. 283–291, 2001.

[60] K. Yasui, T. Kozuka, T. Tuziuti, A. Towata, Y. Iida, J. King, and P. Macey, “FEM calculation of an acoustic field in a sonochemical reactor,” *Ultrason. Sonochem.*, vol. 14, no. 5, pp. 605–614, 2007.

[61] M. M. van Iersel, N. E. Benes, and J. T. F. Keurentjes, “Importance of acoustic shielding in sonochemistry,” *Ultrason. Sonochem.*, vol. 15, no. 4, pp. 294–300, 2008.

[62] Y. Son, M. Lim, and J. Khim, “Investigation of acoustic cavitation energy in a large-scale sonoreactor,” *Ultrason. Sonochem.*, vol. 16, no. 4, pp. 552–556, 2009.

[63] O. Louisnard, “A simple model of ultrasound propagation in a cavitating liquid. Part I: Theory, nonlinear attenuation and traveling wave generation,” *Ultrason. Sonochem.*, vol. 19, no. 1, pp. 56–65, 2012.

[64] O. Louisnard, “A viable method to predict acoustic streaming in presence of cavitation,” *Ultrason. Sonochem.*, vol. 35, pp. 518–524, 2017.

[65] F. J. Trujillo, “A strict formulation of a nonlinear Helmholtz equation for the propagation of sound in bubbly liquids. Part I: Theory and validation at low acoustic pressure amplitudes,” *Ultrason. Sonochem.*, vol. 47, pp. 75–98, 2018.

[66] A. A. Doinikov, “Acoustic radiation forces: Classical theory and recent advances,” *Recent Res. Devel. Acoust.*, vol. 1, pp. 39–67, 2003.

[67] A. O. Maksimov and T. G. Leighton, “Acoustic radiation force on a parametrically distorted bubble,” *J. Acoust. Soc. Am.*, vol. 143, no. 1, pp. 296–305, 2018.

[68] H. Mitome, T. Kozuka, T. Tuziuti, and L. Wang, “Quasi acoustic streaming induced by generation of cavitation bubbles,” *IEEE Ultrason. Symp. Proc.*, vol. 1, pp. 533–536, 1997.

[69] S. Sakamoto and Y. Watanabe, “Effects of Existence of Microbubbles for Increase of Acoustic Streaming,” *Jpn. J. Appl. Phys.*, vol. 38, no. Part 1, No. 5B, pp. 3050–3052, 1999.

[70] T. Okabe, S. Sakamoto, and Y. Watanabe, “Experimental study on acoustic streaming in water containing microcapsules,” *Jpn. J. Appl. Phys.*, vol. 40, no. Part 1, No. 5B, pp. 3861–3864, 2001.

[71] S. Nomura, S. Mukasa, M. Kuroiwa, Y. Okada, and K. Murakami, “Cavitation bubble streaming in ultrasonic-standing-wave field,” *Jpn. J. Appl. Phys.*, vol. 44, no. 5A, pp. 3161–3164, 2005.

[72] Y. Kojima, Y. Asakura, G. Sugiyama, and S. Koda, “The effects of acoustic flow and mechanical flow on the sonochemical efficiency in a rectangular sonochemical reactor,” *Ultrason. Sonochem.*, vol. 17, no. 6, pp. 978–984, 2010.

[73] Z. Xu, K. Yasuda, and S. Koda, “Numerical simulation of liquid velocity distribution in a sonochemical reactor,” *Ultrason. Sonochem.*, vol. 20, no. 1, pp. 452–459, 2013.

[74] Y. Uemura, K. Sasaki, K. Minami, T. Sato, P. K. Choi, and S. Takeuchi, “Observation of cavitation bubbles and acoustic streaming in high intensity ultrasound fields,” *Jpn. J. Appl. Phys.*, vol. 54, no. 7, pp. 1–6, 2015.

[75] T. Nowak, C. Cairós, E. Batyrshin, and R. Mettin, “Acoustic streaming and bubble translation at a cavitating ultrasonic horn,” *AIP Conf. Proc.*, vol. 1685, p. 020002, 2015.

[76] X. Ma, B. Huang, G. Wang, and M. Zhang, “Experimental investigation of conical bubble structure and acoustic flow structure in ultrasonic field,” *Ultrason. Sonochem.*, vol. 34, pp. 164–172, 2017.

[77] C.-D. Ohl, M. Arora, R. Dijkink, V. Janve, and D. Lohse, “Surface cleaning from laser-induced cavitation bubbles,” *Appl. Phys. Lett.*, vol. 89, no. 7, pp. 1–3, 2006.

[78] R. Dijkink and C.-D. Ohl, “Measurement of cavitation induced wall shear stress,” *Appl. Phys. Lett.*, vol. 93, no. 25, p. 254107, 2008.

[79] F. Reuter, S. R. Gonzalez-Avila, R. Mettin, and C.-D. Ohl, “Flow fields and vortex dynamics of bubbles collapsing near a solid boundary,” *Phys. Rev. Fluids*, vol. 2, no. 6, pp. 1–34, 2017.

[80] P. Koukouvinis, G. Strotos, Q. Zeng, S. R. Gonzalez-Avila, A. Theodorakakos, M. Gavaises, and C.-D. Ohl, “Parametric investigations of the induced shear stress by a laser-generated bubble,” *Langmuir*, vol. 34, no. 22, pp. 6428–6442, 2018.

[81] F. Reuter and R. Mettin, "Electrochemical wall shear rate microscopy of collapsing bubbles," *Phys. Rev. Fluids*, vol. 3, no. 6, p. 063601, 2018.

[82] Q. Zeng, S. R. Gonzalez-Avila, R. Dijkink, P. Koukouvinis, M. Gavaises, and C.-D. Ohl, "Wall shear stress from jetting cavitation bubbles," *J. Fluid Mech.*, vol. 846, pp. 341–355, 2018.

[83] P. Marmottant and S. Hilgenfeldt, "Controlled vesicle deformation and lysis by single oscillating bubbles," *Nature*, vol. 423, no. 6936, pp. 153–156, 2003.

[84] A. Marin, M. Rossi, B. Rallabandi, C. Wang, S. Hilgenfeldt, and C. J. Kähler, "Three-dimensional phenomena in microbubble acoustic streaming," *Phys. Rev. Appl.*, vol. 3, no. 4, p. 041001, 2015.

[85] R. Bolaños-Jiménez, M. Rossi, D. Fernandez Rivas, C. J. Kähler, and A. Marin, "Streaming flow by oscillating bubbles: Quantitative diagnostics via particle tracking velocimetry," *J. Fluid Mech.*, vol. 820, no. May, pp. 529–548, 2017.

[86] P. Sharma, M. Flury, and J. Zhou, "Detachment of colloids from a solid surface by a moving air-water interface," *J. Colloid Interface Sci.*, vol. 326, no. 1, pp. 143–150, 2008.

[87] W. Kim, T. H. Kim, J. Choi, and H. Y. Kim, "Mechanism of particle removal by megasonic waves," *Appl. Phys. Lett.*, vol. 94, no. 8, p. 81908, 2009.

[88] A. Thiemann, T. Nowak, R. Mettin, F. Holsteyns, and A. Lippert, "Characterization of an acoustic cavitation bubble structure at 230 kHz," *Ultrason. Sonochem.*, vol. 18, no. 2, pp. 595–600, 2011.

[89] S. Khodaparast, F. Boulogne, C. Poulard, and H. A. Stone, "Water-based peeling of thin hydrophobic films," *Phys. Rev. Lett.*, vol. 119, no. 15, p. 154502, 2017.

[90] A. A. Busnaina, H. Lin, N. Moumen, J. W. Feng, and J. Taylor, “Particle adhesion and removal mechanisms in post-CMP cleaning processes,” *IEEE Trans. Semicond. Manuf.*, vol. 15, no. 4, pp. 374–382, 2002.

[91] H. F. Okorn-Schmidt, F. Holsteyns, A. Lippert, D. Mui, M. Kawaguchi, C. Lechner, P. E. Frommhold, T. Nowak, F. Reuter, M. B. Pique, C. Cairos, and R. Mettin, “Particle cleaning technologies to meet advanced semiconductor device process requirements,” *ECS J. Solid State Sci. Technol.*, vol. 3, no. 1, pp. N3069–N3080, 2014.

[92] C. Henry and J.-P. Minier, “Progress in particle resuspension from rough surfaces by turbulent flows,” *Prog. Energy Combust. Sci.*, vol. 45, no. C, pp. 1–53, 2014.

[93] T. J. Bulat, “Macrosonics in industry. 3. Ultrasonic cleaning,” *Ultrasonics*, vol. 12, no. 2, pp. 59–68, 1974.

[94] K. I. Busnaina A.A. and G. G. W, “An experimental study of megasonic cleaning of Silicon Wafer,” *J. Electrochem. Soc.*, vol. 142, no. 8, p. 2812, 1995.

[95] L. Yuan, H. Y. Cheng, M. C. Chu, and P. T. Leung, “Physical parameters affecting sonoluminescence: A self-consistent hydrodynamic study,” *Phys. Rev. E - Stat. Physics, Plasmas, Fluids, Relat. Interdiscip. Top.*, vol. 57, no. 4, pp. 4265–4280, 1998.

[96] S. Muthukumaran, S. E. Kentish, G. W. Stevens, and M. Ashokkumar, “Application of ultrasound in membrane separation processes: A review,” *Rev. Chem. Eng.*, vol. 22, no. 3, pp. 155–194, 2006.

[97] B. Niemczewski, “Cavitation intensity of water under practical ultrasonic cleaning conditions,” *Ultrason. Sonochem.*, vol. 21, no. 1, pp. 354–359, 2014.

[98] B. K. Tiwari, “Ultrasound: A clean, green extraction technology,” *Trends Anal. Chem.*, vol. 71, pp. 100–109, 2015.

[99] H. Xu, J. Tu, F. Niu, and P. Yang, "Cavitation dose in an ultrasonic cleaner and its dependence on experimental parameters," *Appl. Acoust.*, vol. 101, pp. 179–184, 2016.

[100] N. Pokhrel, P. K. Vabbina, and N. Pala, "Sonochemistry: Science and Engineering," *Ultrason. Sonochem.*, vol. 29, pp. 104–128, 2016.

[101] R. J. Wood, J. Lee, and M. J. Bussemaker, "A parametric review of sonochemistry: Control and augmentation of sonochemical activity in aqueous solutions," *Ultrason. Sonochem.*, vol. 38, pp. 351–370, 2017.

[102] B. P. Barber, C. C. Wu, R. Löfstedt, P. H. Roberts, and S. J. Putterman, "Sensitivity of sonoluminescence to experimental parameters," *Phys. Rev. Lett.*, vol. 72, no. 9, pp. 1380–1383, 1994.

[103] G. E. Vazquez and S. J. Putterman, "Temperature and pressure dependence of sonoluminescence," *Phys. Rev. Lett.*, vol. 85, no. 14, pp. 3037–3040, 2000.

[104] W. Gaertner, "Frequency dependence of ultrasonic cavitation," *J. Acoust. Soc. Am.*, vol. 26, no. 6, pp. 977–980, 1954.

[105] D. McQueen, "Frequency dependence of ultrasonic cleaning," *Ultrasonics*, vol. 24, no. 5, pp. 273–280, 1986.

[106] A. A. Busnaina, H. Lin, and N. Moumen, "Surface cleaning mechanisms and future cleaning requirements," *ASMC (Advanced Semicond. Manuf. Conf. Proc.*, pp. 328–333, 2000.

[107] G. J. Price, N. K. Harris, and A. J. Stewart, "Direct observation of cavitation fields at 23 and 515 kHz," *Ultrason. Sonochem.*, vol. 17, no. 1, pp. 30–33, 2010.

[108] T. J. Mason, A. J. Cobley, J. E. Graves, and D. Morgan, "New evidence for the inverse dependence of mechanical and chemical effects on the frequency of ultrasound," *Ultrason. Sonochem.*, vol. 18, no. 1, pp. 226–230, 2011.

[109] S. R. Gonzalez-Avila, F. Prabowo, A. Kumar, and C. D. Ohl, “Improved ultrasonic cleaning of membranes with tandem frequency excitation,” *J. Memb. Sci.*, vol. 415-416, pp. 776–783, 2012.

[110] B. Babgi, M. Zhou, M. Aksu, Y. Alghamdi, and M. Ashokkumar, “Initial growth of sonochemically active and sonoluminescence bubbles at various frequencies,” *Ultrason. Sonochem.*, vol. 29, pp. 55–59, 2016.

[111] L. Zhang, C. Zhou, B. Wang, A. E. G. A. Yagoub, H. Ma, X. Zhang, and M. Wu, “Study of ultrasonic cavitation during extraction of the peanut oil at varying frequencies,” *Ultrason. Sonochem.*, vol. 37, pp. 106–113, 2017.

[112] R. Ji, R. Pflieger, M. Virot, and S. I. Nikitenko, “Multibubble sonochemistry and sonoluminescence at 100 kHz: The missing link between low- and high-frequency ultrasound,” *J. Phys. Chem. B*, vol. 122, no. 27, pp. 6989–6994, 2018.

[113] W. Z. Chen, X. Chen, M. J. Lu, G. Q. Miao, and R. J. Wei, “Single bubble sonoluminescence driven by non-simple-harmonic ultrasounds,” *J. Acoust. Soc. Am.*, vol. 111, pp. 2632–2637, 2002.

[114] D. Chen, L. K. Weavers, and H. W. Walker, “Ultrasonic control of ceramic membrane fouling by particles: Effect of ultrasonic factors,” *Ultrason. Sonochem.*, vol. 13, no. 5, pp. 379–387, 2006.

[115] K. Suzuki, K. Han, S. Okano, J. Soejima, and Y. Koike, “Novel ultrasonic cleaning equipment using waveguide mode,” *Jpn. J. Appl. Phys.*, vol. 48, no. 7, p. 07GM05, 2009.

[116] K. Kerboua and O. Hamdaoui, “Ultrasonic waveform upshot on mass variation within single cavitation bubble: Investigation of physical and chemical transformations,” *Ultrason. Sonochem.*, vol. 42, pp. 508–516, 2018.

[117] T. Janssens, G. Doumen, S. Halder, K. Wostyn, P. W. Mertens, and J. Straka, “The influence of standing waves on cleaning with a megasonic nozzle,” *Solid State Phenom.*, vol. 145-146, pp. 23–26, 2009.

[118] S. Brems, M. Hauptmann, E. Camerotto, X. M. Xu, S. De Gendt, M. M. Heyns, and P. W. Mertens, “The influence of the angle of incidence in megasonic cleaning,” *Solid State Phenom.*, vol. 187, pp. 163–166, 2012.

[119] S. Brems, M. Hauptmann, E. Camerotto, P. Mertens, M. Heyns, H. Struyf, and S. De Gendt, “Physical forces exerted by microbubbles on a surface in a traveling wave field,” *Ultrasonics*, vol. 54, no. 2, pp. 706–709, 2014.

[120] W. Zhai, H. Liu, Z. Hong, W. Xie, and B. Wei, “A numerical simulation of acoustic field within liquids subject to three orthogonal ultrasounds,” *Ultrason. Sonochem.*, vol. 34, pp. 130–135, 2017.

[121] Z. Zhang, T. Gao, X. Liu, D. Li, J. Zhao, Y. Lei, and Y. Wang, “Influence of sound directions on acoustic field characteristics within a rectangle-shaped sonoreactor: Numerical simulation and experimental study,” *Ultrason. Sonochem.*, vol. 42, no. 66, pp. 787–794, 2018.

[122] W. Tangsopa and J. Thongsri, “Development of an industrial ultrasonic cleaning tank based on harmonic response analysis,” *Ultrasonics*, vol. 91, pp. 68–76, 2019.

[123] K. V. B. Tran, Y. Asakura, and S. Koda, “Influence of transducer structure on mechanical and chemical effects of 20 kHz sonication,” *Jpn. J. Appl. Phys.*, vol. 51, no. 7, p. 07GD06, 2012.

[124] L. Jiang, H. Ge, F. Liu, and D. Chen, “Investigations on dynamics of interacting cavitation bubbles in strong acoustic fields,” *Ultrason. Sonochem.*, vol. 34, pp. 90–97, 2017.

[125] N. Kerabchi, S. Merouani, and O. Hamdaoui, “Depth effect on the inertial collapse of cavitation bubble under ultrasound: Special emphasis on the role of the wave attenuation,” *Ultrason. Sonochem.*, vol. 48, pp. 136–150, 2018.

[126] T. Ding, Y. Xie, Z. Shen, X. Cheng, and Z. Wang, “Ultrasonic cleaning optimization research for ultrasmooth optical substrate with artificial micron/submicron silica spheres,” *Opt. Eng.*, vol. 53, no. 12, p. 122514, 2014.

[127] I. Tzanakis, G. S. Lebon, D. G. Eskin, and K. A. Pericleous, “Characterizing the cavitation development and acoustic spectrum in various liquids,” *Ultrason. Sonochem.*, vol. 34, pp. 651–662, 2017.

[128] G. B. Lebon, I. Tzanakis, K. Pericleous, and D. Eskin, “Experimental and numerical investigation of acoustic pressures in different liquids,” *Ultrason. Sonochem.*, vol. 42, pp. 411–421, 2018.

[129] V. Q. Vuong, “The influence of liquid temperature on the sonoluminescence hot spot,” *J. Acoust. Soc. Am.*, vol. 104, no. 4, p. 2073, 1998.

[130] H. G. Flynn, “Cavitation dynamics. I. A mathematical formulation,” *J. Acoust. Soc. Am.*, vol. 57, no. 6, p. 1379, 1975.

[131] I. Akhatov, N. Gumerov, C. D. Ohl, U. Parlitz, and W. Lauterborn, “The role of surface tension in stable single-bubble sonoluminescence,” *Phys. Rev. Lett.*, vol. 78, no. 2, pp. 227–230, 1997.

[132] E. Camerotto, S. Brems, M. Hauptmann, A. Pacco, H. Struyf, P. W. Mertens, and S. De Gendt, “Influence of surface tension on cavitation noise spectra and particle removal efficiency in high frequency ultrasound fields,” *J. Appl. Phys.*, vol. 112, no. 11, p. 114322, 2012.

[133] S. Popinet and S. Zaleski, “Bubble collapse near a solid boundary: A numerical study of the influence of viscosity,” *J. Fluid Mech.*, vol. 464, pp. 137–163, 2002.

[134] V. Salinas, Y. Vargas, O. Louisnard, and L. Gaete, “Influence of the liquid viscosity on the formation of bubble structures in a 20 kHz field,” *Ultrason. Sonochem.*, vol. 22, pp. 227–234, 2015.

[135] T.-G. Kim, K. L. Wostyn, P. Mertens, A. A. Busnaina, and J.-G. Park, “Quantitative measurement of pattern collapse and particle removal force,” *ECS Trans.*, vol. 11, no. 2, pp. 123–129, 2007.

[136] O. Supponen, D. Obreschkow, M. Tinguely, P. Kobel, N. Dorsaz, and M. Farhat, “Scaling laws for jets of single cavitation bubbles,” *J. Fluid Mech.*, vol. 802, pp. 263–293, 2016.

[137] O. Supponen, D. Obreschkow, P. Kobel, M. Tinguely, N. Dorsaz, and M. Farhat, “Shock waves from nonspherical cavitation bubbles,” *Phys. Rev. Fluids*, vol. 2, no. 9, p. 093601, 2017.

[138] S. A. Beig, B. Aboulhasanzadeh, and E. Johnsen, “Temperatures produced by inertially collapsing bubbles near rigid surfaces,” *J. Fluid Mech.*, vol. 852, pp. 105–125, 2018.

[139] P. Marlin and G. L. Chahine, “Erosion and heating of polyurea under cavitating jets,” *Wear*, vol. 414-415, pp. 262–274, 2018.

[140] I. Hansson and K. A. Mørch, “The dynamics of cavity clusters in ultrasonic (vibratory) cavitation erosion,” *J. Appl. Phys.*, vol. 51, no. 9, pp. 4651–4658, 1980.

[141] D. Krefting, R. Mettin, and W. Lauterborn, “High-speed observation of acoustic cavitation erosion in multibubble systems,” *Ultrason. Sonochem.*, vol. 11, no. 3-4, pp. 119–123, 2004.

[142] M. Virot, T. Chave, S. I. Nikitenko, D. G. Shchukin, T. Zemb, and H. Mohwald, “Acoustic cavitation at the water-glass interface,” *J. Phys. Chem. C*, vol. 114, no. 30, pp. 13083–13091, 2010.

[143] W. Kim, K. Park, J. Oh, J. Choi, and H. Y. Kim, “Visualization and minimization of disruptive bubble behavior in ultrasonic field,” *Ultrasonics*, vol. 50, no. 8, pp. 798–802, 2010.

[144] D. Fernandez Rivas, J. Betjes, B. Verhaagen, W. Bouwhuis, T. C. Bor, D. Lohse, and H. J. Gardeniers, “Erosion evolution in mono-crystalline silicon surfaces caused by acoustic cavitation bubbles,” *J. Appl. Phys.*, vol. 113, no. 6, p. 064902, 2013.

[145] C.-T. Hsiao, A. Jayaprakash, A. Kapahi, J.-K. Choi, and G. L. Chahine, “Modelling of material pitting from cavitation bubble collapse,” *J. Fluid Mech.*, vol. 755, pp. 142–175, 2014.

[146] X. D. Ren, H. He, Y. Q. Tong, Y. P. Ren, S. Q. Yuan, R. Liu, C. Y. Zuo, K. Wu, S. Sui, and D. S. Wang, “Experimental investigation on dynamic characteristics and strengthening mechanism of laser-induced cavitation bubbles,” *Ultrason. Sonochem.*, vol. 32, pp. 218–223, 2016.

[147] P. Cui, A.-M. Zhang, S. Wang, and B. C. Khoo, “Ice breaking by a collapsing bubble,” *J. Fluid Mech.*, vol. 841, pp. 287–309, 2018.

[148] B. C. Goh, F. Goh, C. Lim, Z. Ismail, and M. S. Zhou, “Impact of re-gasified water on megasonic cleaning,” *Solid State Phenom.*, vol. 134, pp. 217–220, 2008.

[149] F. J. Fuchs, “Ultrasonic cleaning and washing of surfaces,” in *Power Ultrason. Appl. High-Intensity Ultrasound*, pp. 577–609, Elsevier Ltd., 2014.

[150] L. Liu, Y. Yang, P. Liu, and W. Tan, “The influence of air content in water on ultrasonic cavitation field,” *Ultrason. Sonochem.*, vol. 21, no. 2, pp. 566–571, 2014.

[151] K. L. Mittal and R. Jaiswal, *Particle Adhesion and Removal*. Hoboken, NJ, USA: John Wiley & Sons, Inc., 2015.

[152] G. Vereecke, F. Holsteyns, S. Arnauts, S. Beckx, P. Jaenen, K. Kenis, M. Lismont, M. Lux, R. Vos, J. Snow, and P. W. Mertens, “Evaluation of megasonic cleaning for sub-90nm technologies,” *Solid State Phenom.*, vol. 103-104, pp. 141–146, 2005.

[153] M. Keswani, S. Raghavan, and P. Deymier, “Electrochemical investigations of stable cavitation from bubbles generated during reduction of water,” *Ultrason. Sonochem.*, vol. 21, no. 5, pp. 1893–1899, 2014.

[154] A. A. Atchley and A. Prosperetti, “The crevice model of bubble nucleation,” *J. Acoust. Soc. Am.*, vol. 86, no. 3, pp. 1065–1084, 1989.

[155] A. Andersen and K. A. Mørch, “Cavitation nuclei in water exposed to transient pressures,” *J. Fluid Mech.*, vol. 771, pp. 424–448, 2015.

[156] D. Lohse and X. Zhang, “Pinning and gas oversaturation imply stable single surface nanobubbles,” *Phys. Rev. E*, vol. 91, no. 3, p. 031003, 2015.

[157] K. Yasui, T. Tuziuti, W. Kanematsu, and K. Kato, “Dynamic equilibrium model for a bulk nanobubble and a microbubble partly covered with hydrophobic material,” *Langmuir*, vol. 32, no. 43, pp. 11101–11110, 2016.

[158] K. A. Mϕrch, “Cavitation inception from bubble nuclei,” *Interface Focus*, vol. 5, pp. 1–13, 2015.

[159] M. Hauptmann, S. Brems, E. Camerotto, A. Zijlstra, G. Doumen, T. Bearda, P. W. Mertens, and W. Lauriks, “Influence of gasification on the performance of a 1 MHz nozzle system in megasonic cleaning,” *Microelectron. Eng.*, vol. 87, no. 5-8, pp. 1512–1515, 2010.

[160] Y. Tano, A. Iizuka, E. Shibata, and T. Nakamura, “Physical washing method for the removal of press oil using the high-speed movement of microbubbles under ultrasonic irradiation,” *Ind. Eng. Chem. Res.*, vol. 52, no. 44, pp. 15658–15663, 2013.

[161] P. R. Birkin, D. G. Offin, C. J. Vian, and T. G. Leighton, “Electrochemical ’bubble swarm’ enhancement of ultrasonic surface cleaning,” *Phys. Chem. Chem. Phys.*, vol. 17, no. 33, pp. 21709–21715, 2015.

[162] P. R. Birkin, D. G. Offin, and T. G. Leighton, “An activated fluid stream - New techniques for cold water cleaning,” *Ultrason. Sonochem.*, vol. 29, pp. 612–618, 2016.

[163] A. Iizuka, W. Iwata, E. Shibata, and T. Nakamura, “Physical washing method for press oil removal from side surfaces using microbubbles under ultrasonic irradiation,” *Ind. Eng. Chem. Res.*, vol. 55, no. 40, pp. 10782–10787, 2016.

[164] T. Tuziuti, “Influence of sonication conditions on the efficiency of ultrasonic cleaning with flowing micrometer-sized air bubbles,” *Ultrason. Sonochem.*, vol. 29, pp. 604–611, 2016.

[165] M. Hashemi Shahraki, A. Maskooki, and A. Faezian, “Hollow Fibers Filtration and Cleaning Processes Under Ultrasound and Gas Bubbling Combination,” *J. Food Process Eng.*, vol. 40, no. 1, p. e12325, 2017.

[166] J. J. Kwan, S. Graham, R. Myers, R. Carlisle, E. Stride, and C. C. Coussios, “Ultrasound-induced inertial cavitation from gas-stabilizing nanoparticles,” *Phys. Rev. E*, vol. 92, no. 2, p. 023019, 2015.

[167] A. Zijlstra, D. Fernandez Rivas, H. J. Gardeniers, M. Versluis, and D. Lohse, “Enhancing acoustic cavitation using artificial crevice bubbles,” *Ultrasonics*, vol. 56, pp. 512–523, 2015.

[168] B. Verhaagen, Y. Liu, A. G. Pérez, E. Castro-Hernandez, and D. Fernandez Rivas, “Scaled-up sonochemical microreactor with increased efficiency and reproducibility,” *ChemistrySelect*, vol. 1, no. 2, pp. 136–139, 2016.

[169] L. M. Bryson, D. Fernandez Rivas, and C. Boutsioukis, “Cleaning of used rotary nickel-titanium files in an ultrasonic bath by locally intensified acoustic cavitation,” *Int. Endod. J.*, vol. 51, no. 4, pp. 457–468, 2018.

[170] E. J. Slowinski, E. E. Gates, and C. E. Waring, “The effect of pressure on the surface tensions of liquids,” *J. Phys. Chem.*, vol. 61, no. 6, pp. 808–810, 1957.

[171] R. Massoudi and A. D. King, “Effect of pressure on the surface tension of water. Adsorption of low molecular weight gases on water at 25°C,” *J. Phys. Chem.*, vol. 78, no. 22, pp. 2262–2266, 1974.

[172] S. Jain and L. Qiao, “Molecular dynamics simulations of the surface tension of oxygen-supersaturated water,” *AIP Adv.*, vol. 7, no. 4, p. 045001, 2017.

[173] W. J. Galloway, “An experimental study of acoustically induced cavitation in liquids,” *J. Acoust. Soc. Am.*, vol. 26, no. 5, pp. 849–857, 1954.

[174] Y. Mori, K. Hijikata, and T. Nagatani, “Effect of dissolved gas on bubble nucleation,” *Int. J. Heat Mass Transf.*, vol. 19, no. 10, pp. 1153–1159, 1976.

[175] S. Jones, G. Evans, and K. Galvin, “Bubble nucleation from gas cavities - A review,” *Adv. Colloid Interface Sci.*, vol. 80, no. 1, pp. 27–50, 1999.

[176] S. Jones, G. Evans, and K. Galvin, “The cycle of bubble production from a gas cavity in a supersaturated solution,” *Adv. Colloid Interface Sci.*, vol. 80, no. 1, pp. 51–84, 1999.

[177] S. D. Lubetkin, “Why is it much easier to nucleate gas bubbles than theory predicts?,” *Langmuir*, vol. 19, no. 7, pp. 2575–2587, 2003.

[178] B. C. Knott, J. L. LaRue, A. M. Wodtke, M. F. Doherty, and B. Peters, “Communication: Bubbles, crystals, and laser-induced nucleation,” *J. Chem. Phys.*, vol. 134, no. 17, p. 171102, 2011.

[179] M. R. Ward, W. J. Jamieson, C. A. Leckey, and A. J. Alexander, “Laser-induced nucleation of carbon dioxide bubbles,” *J. Chem. Phys.*, vol. 142, no. 14, p. 144501, 2015.

[180] B. Li, Y. Gu, and M. Chen, “An experimental study on the cavitation of water with dissolved gases,” *Exp. Fluids*, vol. 58, no. 12, p. 164, 2017.

[181] L. Zhang, Y. Zhang, X. Zhang, Z. Li, G. Shen, M. Ye, C. Fan, H. Fang, and J. Hu, “Electrochemically controlled formation and growth of hydrogen nanobubbles,” *Langmuir*, vol. 22, no. 19, pp. 8109–8113, 2006.

[182] P. S. Epstein and M. S. Plesset, “On the stability of gas bubbles in liquid-gas solutions,” *J. Chem. Phys.*, vol. 18, no. 11, pp. 1505–1509, 1950.

[183] S. Ljunggren and J. C. Eriksson, “The lifetime of a colloid-sized gas bubble in water and the cause of the hydrophobic attraction,” *Colloids Surfaces A Physicochem. Eng. Asp.*, vol. 129-130, pp. 151–155, 1997.

[184] Y. Wang, M. E. Zaytsev, H. L. The, J. C. T. Eijkel, H. J. W. Zandvliet, X. Zhang, and D. Lohse, “Vapor and gas-bubble growth dynamics around laser-irradiated, water-immersed plasmonic nanoparticles,” *ACS Nano*, vol. 11, no. 2, pp. 2045–2051, 2017.

[185] M. Alheshibri, J. Qian, M. Jehannin, and V. S. J. Craig, “A history of nanobubbles,” *Langmuir*, vol. 32, no. 43, pp. 11086–11100, 2016.

[186] M. M. van Iersel, J. Cornel, N. E. Benes, and J. T. Keurentjes, “Inhibition of nonlinear acoustic cavitation dynamics in liquid CO_2,” *J. Chem. Phys.*, vol. 126, no. 6, pp. 1–8, 2007.

[187] J. Rooze, E. V. Rebrov, J. C. Schouten, and J. T. Keurentjes, “Dissolved gas and ultrasonic cavitation - A review,” *Ultrason. Sonochem.*, vol. 20, no. 1, pp. 1–11, 2013.

[188] N. S. Khabeev, "Diffusion effects in the oscillation of vapor-gas bubbles in a sound field," *Int. J. Heat Mass Transf.*, vol. 50, no. 17-18, pp. 3556–3560, 2007.

[189] Y. Hao, Y. Zhang, and A. Prosperetti, "Mechanics of gas-vapor bubbles," *Phys. Rev. Fluids*, vol. 2, no. 3, 2017.

[190] K. B. Bader and V. Bollen, "The influence of gas diffusion on bubble persistence in shock-scattering histotripsy," *J. Acoust. Soc. Am.*, vol. 143, no. 6, pp. EL481–EL486, 2018.

[191] Y. Zhang, Y. Gao, Z. Guo, and X. Du, "Effects of mass transfer on damping mechanisms of vapor bubbles oscillating in liquids," *Ultrason. Sonochem.*, vol. 40, pp. 120–127, 2018.

[192] F. Holsteyns, K. T. Lee, S. Graf, R. Palmans, G. Vereecke, and P. W. Mertens, "Megasonics: A cavitation driven process," *Solid State Phenom.*, vol. 103-104, pp. 159–162, 2005.

[193] S. Kumari, M. Keswani, S. Singh, M. Beck, E. Liebscher, L. Q. Toan, and S. Raghavan, "Effect of dissolved CO_2 in de-ionized water in reducing wafer damage during megasonic cleaning in MegPie," *ECS Trans.*, vol. 41, no. 5, pp. 93–99, 2011.

[194] M. Hauptmann, S. Brems, H. Struyf, P. Mertens, M. Heyns, S. De Gendt, and C. Glorieux, "Time-resolved monitoring of cavitation activity in megasonic cleaning systems," *Rev. Sci. Instrum.*, vol. 83, no. 3, pp. 1–11, 2012.

[195] B. K. Kang, M. S. Kim, and J. G. Park, "Effect of dissolved gases in water on acoustic cavitation and bubble growth rate in 0.83 MHz megasonic of interest to wafer cleaning," *Ultrason. Sonochem.*, vol. 21, no. 4, pp. 1496–1503, 2014.

[196] M. Hauptmann, F. Frederickx, H. Struyf, P. Mertens, M. Heyns, S. De Gendt, C. Glorieux, and S. Brems, "Enhancement of cavitation activity and particle

removal with pulsed high frequency ultrasound and supersaturation," *Ultrason. Sonochem.*, vol. 20, no. 1, pp. 69–76, 2013.

[197] S. Brems, M. Hauptmann, E. Camerotto, A. Pacco, T.-G. Kim, X. Xu, K. Wostyn, P. Mertens, and S. De Gendt, "Nanoparticle removal with megasonics: A review," *ECS J. Solid State Sci. Technol.*, vol. 3, no. 1, pp. N3010–N3015, 2013.

[198] R. Pflieger, L. Gravier, G. Guillot, M. Ashokkumar, and S. I. Nikitenko, "Inverse effects of the gas feed positioning on sonochemistry and sonoluminescence," *Ultrason. Sonochem.*, vol. 46, pp. 10–17, 2018.

[199] M. Takahashi, "Zeta potential of microbubbles in aqueous solutions: Electrical properties of the gas-water interface.," *J. Phys. Chem. B*, vol. 109, no. 46, pp. 21858–21864, 2005.

[200] S. Khuntia, S. K. Majumder, and P. Ghosh, "Microbubble-aided water and wastewater purification: A review," *Rev. Chem. Eng.*, vol. 28, no. 4-6, pp. 191–221, 2012.

[201] K. Terasaka, A. Hirabayashi, T. Nishino, S. Fujioka, and D. Kobayashi, "Development of microbubble aerator for waste water treatment using aerobic activated sludge," *Chem. Eng. Sci.*, vol. 66, no. 14, pp. 3172–3179, 2011.

[202] F. Kobayashi, H. Ikeura, S. Ohsato, T. Goto, and M. Tamaki, "Disinfection using ozone microbubbles to inactivate Fusarium oxysporum f. sp. melonis and Pectobacterium carotovorum subsp. carotovorum," *Crop Prot.*, vol. 30, no. 11, pp. 1514–1518, 2011.

[203] K. Ebina, K. Shi, M. Hirao, J. Hashimoto, Y. Kawato, S. Kaneshiro, T. Morimoto, K. Koizumi, and H. Yoshikawa, "Oxygen and air nanobubble water solution promote the growth of plants, fishes, and mice," *PLoS One*, vol. 8, no. 6, pp. 2–8, 2013.

[204] A. Endo, S. Srithongouthai, H. Nashiki, I. Teshiba, T. Iwasaki, D. Hama, and H. Tsutsumi, "DO-increasing effects of a microscopic bubble generating system in a fish farm," *Mar. Pollut. Bull.*, vol. 57, no. 1-5, pp. 78–85, 2008.

[205] J. Creech, V. Divino, W. Patterson, P. J. Zalesky, and C. E. Brennen, "Injection of highly supersaturated oxygen solutions without nucleation," *J. Biomech. Eng.*, vol. 124, no. 6, pp. 676–683, 2002.

[206] I. B. Butler, M. A. A. Schoonen, and D. T. Rickard, "Removal of dissolved oxygen from water: A comparison of four common techniques," *Talanta*, vol. 41, no. 2, pp. 211–215, 1994.

[207] H. Tsuge, *Micro- and Nanobubbles: Fundamentals and Applications*. CRC Press, 2014.

[208] S. Goldman, "A new class of biophysical models for predicting the probability of decompression sickness in scuba diving," *J. Appl. Physiol.*, vol. 103, no. 2, pp. 484–493, 2007.

[209] G. R. Bouck, "Etiology of gas bubble disease," *T. Am. Fish. Soc.*, vol. 109, no. 6, pp. 7043–707, 1980.

[210] A. Kabalnov, D. Klein, T. Pelura, E. Schutt, and J. Weers, "Dissolution of multicomponent microbubbles in the bloodstream: 1. Theory," *Ultrasound Med. Biol.*, vol. 24, no. 5, pp. 739–749, 1998.

[211] S. Shim, J. Wan, S. Hilgenfeldt, P. D. Panchal, and H. A. Stone, "Dissolution without disappearing: Multicomponent gas exchange for CO_2 bubbles in a microfluidic channel.," *Lab Chip*, vol. 14, no. 14, pp. 2428–2436, 2014.

[212] O. R. Enríquez, C. Hummelink, G. W. Bruggert, D. Lohse, A. Prosperetti, D. van der Meer, and C. Sun, "Growing bubbles in a slightly supersaturated liquid solution," *Rev. Sci. Instrum.*, vol. 84, no. 6, 2013.

[213] O. R. Enríquez, C. Sun, D. Lohse, A. Prosperetti, and D. van der Meer, "The quasi-static growth of CO_2 bubbles," *J. Fluid Mech.*, vol. 741, p. R1, 2014.

[214] J. Holocher, F. Peeters, W. Aeschbach-Hertig, W. Kinzelbach, and R. Kipfer, "Kinetic model of gas bubble dissolution in groundwater and its implications for the dissolved gas composition," *Environ. Sci. Technol.*, vol. 37, no. 7, pp. 1337–1343, 2003.

[215] J. J. Kwan and M. A. Borden, "Microbubble dissolution in a multigas environment," *Langmuir*, vol. 26, no. 9, pp. 6542–6548, 2010.

[216] S. V. Dalvi and J. R. Joshi, "Modeling of microbubble dissolution in aqueous medium," *J. Colloid Interface Sci.*, vol. 437, pp. 259–269, 2015.

[217] P. Peñas-López, M. A. Parrales, and J. Rodríguez-Rodríguez, "Dissolution of a CO_2 spherical cap bubble adhered to a flat surface in air-saturated water," *J. Fluid Mech.*, vol. 775, pp. 53–76, 2015.

[218] K. Yasui, T. Tuziuti, and W. Kanematsu, "Extreme conditions in a dissolving air nanobubble," *Phys. Rev. E*, vol. 94, no. 1, p. 013106, 2016.

[219] S. Uesawa, A. Kaneko, Y. Nomura, and Y. Abe, "Study on bubble breakup in a Venturi tube," *Multiph. Sci. Technol.*, vol. 24, no. 3, pp. 257–277, 2012.

[220] N. Otsu, "A threshold selection method from gray-level histograms," *IEEE Trans. Syst., Man, Cybern.*, vol. SMC-9, no. 1, pp. 62–66, 1979.

[221] P. B. Duncan and D. Needham, "Test of the Epstein-Plesset model for gas microparticle dissolution in aqueous media: Effect of surface tension and gas undersaturation in solution," *Langmuir*, vol. 20, no. 7, pp. 2567–2578, 2004.

[222] E. Wilhelm, R. Battino, and R. J. Wilcock, "Low-pressure solubility of gases in liquid water," *Chem. Rev.*, vol. 77, pp. 219–262, 1977.

[223] R. Sander, "Compilation of Henry's law constants (version 4.0) for water as solvent," *Atmos. Chem. Phys.*, vol. 15, no. 8, pp. 4399–4981, 2015.

[224] O. R. Enríquez, *Growing bubbles and freezing drops: Depletion effects and tip singularities*. PhD thesis, University of Twente, 2015.

[225] R. J. Wilcock and R. Battino, "Solubility of oxygen-nitrogen mixture in water," *Nature*, vol. 252, pp. 614–615, 1974.

[226] N. Bignell, "Precise density measurements of aqueous solutions of mixed nonpolar gases," *J. Phys. Chem.*, vol. 91, no. 6, pp. 1687–1690, 1987.

[227] M. Dular, O. C. Delgosha, and M. Petkovšek, "Observations of cavitation erosion pit formation," *Ultrason. Sonochem.*, vol. 20, no. 4, pp. 1113–1120, 2013.

[228] V. Filipe, A. Hawe, and W. Jiskoot, "Critical evaluation of nanoparticle tracking analysis (NTA) by nanosight for the measurement of nanoparticles and protein aggregates," *Pharm. Res.*, vol. 27, no. 5, pp. 796–810, 2010.

[229] R. Oguri and K. Ando, "Cavitation bubble nucleation induced by shock-bubble interaction in a gelatin gel," *Phys. Fluids*, vol. 30, no. 5, pp. 1–6, 2018.

[230] A. A. Atchley, "The crevice model of bubble nucleation," *J. Acoust. Soc. Am.*, vol. 86, no. 3, p. 1065, 1989.

[231] J. N. Israelachvili, *Intermolecular and Surface Forces*. Academic Press, 2011.

[232] I. Tudela, V. Sáez, M. D. Esclapez, M. I. Díez-García, P. Bonete, and J. González-García, "Simulation of the spatial distribution of the acoustic pressure in sonochemical reactors with numerical methods: A review," *Ultrason. Sonochem.*, vol. 21, no. 3, pp. 909–919, 2014.

[233] K. Yasui, "Unsolved Problems in Acoustic Cavitation," in *Handb. Ultrason. Sonochemistry* (M. Ashokkumar, ed.), pp. 259–292, Singapore: Springer, Singapore, 2016.

[234] M. Ashokkumar, M. Hodnett, B. Zeqiri, F. Grieser, and G. J. Price, "Acoustic emission spectra from 515 kHz cavitation in aqueous solutions containing surface-active solutes," *J. Am. Chem. Soc.*, vol. 129, no. 8, pp. 2250–2258, 2007.

[235] S. H. Yoo, B. Y. Liu, J. Sun, N. Narayanswami, and G. P. Thomes, "Particle removal efficiency evaluation at 40 nm using haze particle standard," *Solid State Phenom.*, vol. 76, pp. 259–262, 2001.

[236] K. Xu, R. Vos, G. Vereecke, M. Lux, W. Fyen, F. Holsteyns, K. Kenis, P. W. Mertens, M. M. Heyns, and C. Vinckier, "Relation between particle density and haze on a wafer: A new approach to measuring nano-sized particles," *Solid State Phenom.*, vol. 92, pp. 161–164, 2003.

[237] "National Institutes of Health, ImageJ." http://imagej.nih.gov/ij/, 2015.

[238] B. Pugin, "Qualitative characterization of ultrasound reactors for heterogeneous sonochemistry," *Ultrasonics*, vol. 25, no. 1, pp. 49–55, 1987.

[239] M. Chivate and A. Pandit, "Quantification of cavitation intensity in fluid bulk," *Ultrason. Sonochem.*, vol. 2, no. 1, pp. S19–S25, 1995.

[240] V. Sáez, A. Frías-Ferrer, J. Iniesta, J. González-García, A. Aldaz, and E. Riera, "Chacterization of a 20 kHz sonoreactor. Part I: Analysis of mechanical effects by classical and numerical methods," *Ultrason. Sonochem.*, vol. 12, pp. 59–65, 2005.

[241] M. Campbell, J. A. Cosgrove, C. A. Created, S. Jack, and D. Rockliff, "Review of LDA and PIV applied to the measurement of sound and acoustic streaming," *Opt. Laser Technol.*, vol. 32, no. 7-8, pp. 629–639, 2000.

[242] R. B. H. Slama, B. Gilles, M. B. Chiekh, and J. C. Béra, "PIV for the characterization of focused field induced acoustic streaming: Seeding particle choice evaluation," *Ultrasonics*, vol. 76, pp. 217–226, 2017.

[243] R. Mettin, S. Luther, C.-D. Ohl, and W. Lauterborn, “Acoustic cavitation structures and simulations by a particle model,” *Ultrason. Sonochem.*, vol. 6, no. 1-2, pp. 25–29, 1999.

[244] S. Hatanaka, K. Yasui, T. Tuziuti, T. Kozuka, and H. Mitome, “Quenching mechanism of multibubble sonoluminescence at excessive sound pressure,” *Jpn. J. Appl. Phys.*, vol. 40, no. Part 1, No. 5B, pp. 3856–3860, 2001.

[245] C. Wu, N. Nakagawa, and Y. Sekiguchi, “Observation of multibubble phenomena in an ultrasonic reactor,” *Exp. Therm. Fluid Sci.*, vol. 31, no. 8, pp. 1083–1089, 2007.

[246] A. Eller, “Force on a Bubble in a Standing Acoustic Wave,” *J. Acoust. Soc. Am.*, vol. 43, no. 1, pp. 170–171, 1968.

[247] O. Louisnard, “A simple model of ultrasound propagation in a cavitating liquid. Part II: Primary Bjerknes force and bubble structures,” *Ultrason. Sonochem.*, vol. 19, no. 1, pp. 66–76, 2012.

[248] P. R. Birkin, D. G. Offin, and T. G. Leighton, “An activated fluid stream - New techniques for cold water cleaning,” *Ultrason. Sonochem.*, vol. 29, pp. 612–618, 2016.

[249] M. Minnaert, “XVI. On musical air-bubbles and the sounds of running water,” *Philos. Mag.*, vol. 16, no. 104, pp. 235–248, 1933.

[250] H. Monnier, A. M. Wilhelm, and H. Delmas, “Influence of ultrasound on mixing on the molecular scale for water and viscous liquids,” *Ultrason. Sonochem.*, vol. 6, no. 1, pp. 67–74, 1999.

[251] J. P. Rothstein, “Slip on superhydrophobic surfaces,” *Annu. Rev. Fluid Mech.*, vol. 42, no. 1, pp. 89–109, 2010.

[252] M. Strasberg, "The pulsation frequency of nonspherical gas bubbles in liquids," *J. Acoust. Soc. Am.*, vol. 25, no. 3, pp. 536–537, 1953.

[253] T.-H. Kim and H.-Y. Kim, "Disruptive bubble behaviour leading to microstructure damage in an ultrasonic field," *J. Fluid Mech.*, vol. 750, no. 2014, pp. 355–371, 2014.

[254] E. M. B. Payne, S. J. Illesinghe, A. Ooi, and R. Manasseh, "Symmetric mode resonance of bubbles attached to a rigid boundary," *J. Acoust. Soc. Am.*, vol. 118, no. 5, pp. 2841–2849, 2005.

[255] F. Hamaguchi and K. Ando, "Linear oscillation of gas bubbles in a viscoelastic material under ultrasound irradiation," *Phys. Fluids*, vol. 27, no. 11, p. 113103, 2015.

[256] C. Koch, "Sound field measurement in a double layer cavitation cluster by rugged miniature needle hydrophones," *Ultrason. Sonochem.*, vol. 29, pp. 439–446, 2016.

[257] P. A. QUINTO-SU and C.-D. OHL, "Interaction between two laser-induced cavitation bubbles in a quasi-two-dimensional geometry," *J. Fluid Mech.*, vol. 633, p. 425, aug 2009.

[258] F. Yuan, G. Sankin, and P. Zhong, "Dynamics of tandem bubble interaction in a microfluidic channel," *J. Acoust. Soc. Am.*, vol. 130, no. 5, pp. 3339–3346, 2011.

[259] Y. Tomita and K. Sato, "Pulsed jets driven by two interacting cavitation bubbles produced at different times," *J. Fluid Mech.*, vol. 819, pp. 465–493, 2017.

[260] S. R. Gonzalez-Avila, X. Huang, P. A. Quinto-Su, T. Wu, and C.-D. Ohl, "Motion of micrometer sized spherical particles exposed to a transient radial flow: Attraction, repulsion, and rotation," *Phys. Rev. Lett.*, vol. 107, no. 7, p. 074503, 2011.

[261] S. Poulain, G. Guenoun, S. Gart, W. Crowe, and S. Jung, "Particle motion induced by bubble cavitation," *Phys. Rev. Lett.*, vol. 114, no. 21, p. 214501, 2015.

[262] S. Wu, Z. Zuo, H. A. Stone, and S. Liu, “Motion of a free-settling spherical particle driven by a laser-induced bubble,” *Phys. Rev. Lett.*, vol. 119, no. 8, p. 084501, 2017.

[263] J. Lee, S. E. Kentish, and M. Ashokkumar, “The effect of surface-active solutes on bubble coalescence in the presence of ultrasound,” *J. Phys. Chem. B*, vol. 109, no. 11, pp. 5095–5099, 2005.

[264] Tandiono, S. W. Ohl, D. S. W. Ow, E. Klaseboer, V. V. Wong, A. Camattari, and C. D. Ohl, “Creation of cavitation activity in a microfluidic device through acoustically driven capillary waves,” *Lab Chip*, vol. 10, no. 14, pp. 1848–1855, 2010.

[265] C. U. Chan and C. D. Ohl, “Total-internal-reflection-fluorescence microscopy for the study of nanobubble dynamics,” *Phys. Rev. Lett.*, vol. 109, no. 17, p. 174501, 2012.

[266] E. Betzig, E. Betzig, G. H. Patterson, G. H. Patterson, R. Sougrat, R. Sougrat, O. W. Lindwasser, S. Olenych, S. Olenych, J. S. Bonifacino, J. S. Bonifacino, M. W. Davidson, M. W. Davidson, J. Lippincott-Schwartz, H. F. Hess, and H. F. Hess, “Imaging intracellular fluorescent proteins at nanometer resolution,” *Science (80-.).*, vol. 313, no. 5793, pp. 1642–1645, 2006.

[267] H. T. Beier and B. L. Ibey, “Experimental comparison of the high-speed imaging performance of an EM-CCD and sCMOS camera in a dynamic live-cell imaging test case,” *PLoS One*, vol. 9, no. 1, 2014.

[268] S. Khodaparast, M. K. Kim, J. E. Silpe, and H. A. Stone, “Bubble-driven detachment of Bacteria from confined microgeometries,” *Environ. Sci. Technol.*, vol. 51, no. 3, pp. 1340–1347, 2017.

[269] A. Tamayol and M. Bahrami, “Laminar flow in microchannels with noncircular cross section,” *J. Fluids Eng.*, vol. 132, no. 11, p. 111201, 2010.

[270] M. L. Zoeteweij, J. C. J. van der Donck, and R. Versluis, “Particle removal in linear shear flow: Model prediction and experimental validation,” *J. Adhes. Sci. Technol.*, vol. 23, no. 6, pp. 899–911, 2009.

[271] Z. Xu, H. Chen, X. Yan, M. Qian, and Q. Cheng, “Quantitative calibration of sound pressure in ultrasonic standing waves using the Schlieren method,” *Opt. Express*, vol. 25, no. 17, p. 20401, 2017.

[272] T. Colonius, R. Hagmeijer, K. Ando, and C. E. Brennen, “Statistical equilibrium of bubble oscillations in dilute bubbly flows,” *Phys. Fluids*, vol. 20, no. 4, p. 040902, 2008.

[273] K. Ando, T. Colonius, and C. E. Brennen, “Numerical simulation of shock propagation in a polydisperse bubbly liquid,” *Int. J. Multiph. Flow*, vol. 37, no. 6, pp. 596–608, 2011.

[274] J. R. T. Seddon, D. Lohse, W. A. Ducker, and V. S. J. Craig, “A deliberation on nanobubbles at surfaces and in bulk,” *ChemPhysChem*, vol. 13, no. 8, pp. 2179–2187, 2012.

[275] L. Bocquet and E. Charlaix, “Nanofluidics, from bulk to interfaces.,” *Chem. Soc. Rev.*, vol. 39, no. 3, pp. 1073–1095, 2010.

[276] A. E. Kuchma, G. Y. Gor, and F. M. Kuni, “Stages of steady diffusion growth of a gas bubble in strongly supersaturated gas-liquid solution,” *Colloid J.*, vol. 71, no. 4, pp. 520–528, 2009.

List of publication

(1) Articles on periodicals (related to this thesis)

1. T. Yamashita and K. Ando, “Aeration of water with oxygen microbubbles and its purging effect,” *Journal of Fluid Mechanics*, vol. 825, pp. 16–28, 2017.

2. T. Yamashita, and K. Ando, “Low-intensity ultrasound-induced cavitation and streaming in oxygen-supersaturated water: Role of cavitation bubbles as physical cleaning agents,” *Ultrasonics Sonochemistry*, 2019 (In Press).

(2) Other articles

1. T. Yamashita and K. Ando, “Laser-induced nucleation of gas bubbles in oxygen-supersaturated water,” in Proc. of *The Ninth JSME-KSME Thermal and Fluids Engineering Conference (TFEC9)*, TFEC9-1568, Okinawa, Japan, 2017.

2. R. Yamauchi, T. Yamashita and Keita Ando, “Gas-supersaturated water aided ultrasonic cleaning at different driving frequencies: Role of cavitation bubbles in particle removal,” in Proc. of *The Ninth JSME-KSME Thermal and Fluids Engineering Conference (TFEC9)*, TFEC9-1142, Okinawa, Japan, 2017.

3. T. Yamashita, R. Yamauchi and K. Ando, “Progress in ultrasonic cleaning research,” *Japanese Journal of Multiphase Flow*, vol. 32, no. 2, pp. 210–217, 2018.

4. Y. Kurashina, T. Yamashita, S. Kurabayashi, K. Takemura and K. Ando, “Growth control of leaf lettuce with exposure to underwater ultrasound and dissolved oxygen supersaturation,” *Ultrasonics Sonochemistry*, vol. 51, pp. 292–297, 2019.